Development of a large-sized high-pressure xenon gas time projection chamber for neutrinoless double beta decay search

Department of Physics, Graduate School of Science, Kyoto University
Kazuhiro Nakamura

April 22, 2022

Abstract

Exsistence of neutrinos was confirmed more than 60 years ago, and it constitutes the Standard Model as elementary particles. Since it rarely reacts with other particles, there still remains unknown basic properties. Whether the neutrino is a Majorana particle or not is one of the very important themes in modern physics. Revealing the Majorana nature of the neutrino would significantly advance our understanding of the universe and elementary particles.

Almost the only feasible method to test the Majorana nature of the neutrino is to observe the neutrinoless double beta ($0\nu\beta\beta$) decay. Since this phenomenon would not occur if the neutrino is not a Majorana particle, the discovery of this phenomenon would confirm that neutrino has a Majorana nature.

The $0\nu\beta\beta$ decay would be very rare even if it occurs. To search for the $0\nu\beta\beta$ decay, realization of a large detector that contains ton-scale decay nuclei with ultra-low background contamination is necessary.

We propose a $0\nu\beta\beta$ decay search experiment AXEL. The AXEL detector is a high-pressure xenon gas time projection chamber. By filling an enriched ^{136}Xe gas, a double beta nucleus, a $0\nu\beta\beta$ search can be performed. The ionization electrons generated by the $0\nu\beta\beta$ decay are detected by a uniquely developed scheme, ELCC. ELCC can achieve high energy resolution and reconstruct trajectories, thereby realize ultra-low background contamination.

The main object of this thesis is to establish the technology of ELCC that has both scalability and reliability to evaluate the performance near the decay energy called Q-value.

We have resolved discharge problems found in previous studies and upgraded the 180L prototype detector with larger channels and drift length. A dedicated digitizer and a data-taking system have been developed to operate and read out the signal of SiPM photosensors for ELCC. As a result, we succeeded in the stable operation of the 180L detector and demonstrated the detector performance. We obtained a $0.89 \pm 0.03\%$ energy resolution in full width at half maximum at 1.8MeV, which corresponds to $0.77 \pm 0.03\%$ at the $0\nu\beta\beta$ Q-value. We established the ELCC technology and analog and digital signal processing necessary for a larger detector, with which the world's most sensitive $0\nu\beta\beta$ search can be conducted.

Ackknowledgement

博士論文を英語で書いている以上、謝辞も英語で記すべきかもしれません。しかし、お世話になった皆様への感謝の気持ちをちゃんとお伝えするために、ここはあえて日本語で記させていただこうと思います。

まず初めに、指導教員としてご指導いただいた市川温子教授に感謝申し上げます。市川さんの研究への熱意はとにかく強烈で、その熱意についてゆくことは大変なことも多々ありました。しかし、必死にもがく中で大きく成長することができたように思います。市川さんの研究に対する妥協を許さない姿勢、考え抜く態度は、研究者のあるべき姿として強い印象を受けました[1]。また、博士論文の執筆では、たいへんお世話になりました。博士論文は至らない点だらけで情けない限りですが、最後まで見捨てずにコメントをくださったことに感謝申し上げます。ありがとうございました。

次に、中家剛教授に感謝申し上げます。中家さんが自由かつ快適な研究環境を提供してくださったおかげで、非常に充実した大学院生活を送ることができました。また、中家さんには博士論文の執筆において、たいへんお世話になりました。中家さんの手厚いサポートのおかげで、なんとか最後まで博士論文を書き切ることができました。ありがとうございました。

先輩としてお世話になった、中村輝石さん、小原脩平さん、潘晟さん、田中駿祐さんに感謝申し上げます。輝石さんと潘さんには、高エネルギー実験のことは右も左もわからずに入学した M1 のころから、たいへんお世話になりました。田中さんからはエレキ開発を引き継ぎましたが、あの膨大なシステムをひとりで開発されたことにはただただ圧倒されるばかりでした。小原さんからは仕事の進め方について、たいへん多くのことを学ばせていただきました。また、3.3.2 節で述べた ELCC チェックシステムのための回路部品を購入してくださりありがとうございました。もしあのとき小原さんが回路部品を買ってくれていなければ、博士論文の提出が半年は遅れていたと思います。ほんとうにありがとうございました。

同期として 6 年間、一緒に研究をしてくれた吉田将くんに感謝申し上げます。吉田くんのような優秀な同期と仕事ができたことは本当に幸せなことだったと思います。また、市川さんの指示はイマイチなにを言っているのかよくわからないことが多かったのですが、吉田くんが的確な翻訳をしてくれたおかげで、何を言いたいのかがわかった、ということが多々ありました。ありがとうございました。

後輩として研究を支えてくれた、菅島文悟くんと樫野幸将くんに感謝申し上げます。菅島くんも樫野くんも、入ったばかりのころは訳もわからず DAQ の再起動をくり返えさせられたり、ステンレスの板のつけはずしを延々と繰り返させられたりしてウンザリすることも多かったかと思いますが、文句も言わずに付き合ってくれたことにはほんとうに助けられまし

[1] と、同時に、私は研究者には向いていないのかもしれないと思ったことも事実です。私は研究者ではなくディレッタントなのではないかという思いは、大学院生活の中で、始終私の中につきまといました。

た。また、こんなことをこれ以上先の後輩にはさせないという思いは、研究を進める原動力にもなったように思います。ありがとうございました。

最後に、私の研究を支えてくださった、両家族、そして妻の未生に感謝申し上げます。研究ではつらいこともたくさんありましたが、家族と妻の支えがあったからこそ、なんとか乗り越えることができました。ありがとうございました。

Contents

Chapter 1

Introduction

1.1 Neutrino

Neutrino is a lepton with no electric charge and interacts only via the weak interaction. It has been more than 60 years today since the confirmation of its existence by F. Reines and C. L. Cowan [1], but the neutrino is still an enigma. The Standard Model assumes that neutrinos have zero mass, but the 1998 observation of atmospheric neutrinos [2] revealed that neutrinos also have a very small amount of mass. Neutrino oscillation experiments have shown that neutrinos have mass, but the absolute value of neutrino mass is not yet known. There have been three main ways of measuring neutrino mass. The first is a direct measurement of the electron neutrino mass. The KATRIN experiment reported an upper limit for the electron-neutrino mass of $m_\nu < 9.8\,\mathrm{eV/c^2}$ at 90% C.L. [3]. Second, from cosmological observations, the Planck collaboration reported an upper limit for the sum of the neutrino mass of $\sum m_\nu < 0.12\,\mathrm{eV}$ at 95% C.L. [4]. The third is the search for double beta decay without neutrinos, which is introduced in Section 1.2. KamLAND-Zen experiment reported an upper limit for the neutrino effective mass of $\langle m_{\beta\beta} \rangle < (36 - 156)\,\mathrm{meV}$ at the 90% C.L. [5].

The difference between neutrinos and antineutrinos is possible to be the difference of a chirality. Then, neutrinos are Majorana particles. One of the most important themes in neutrino is whether the neutrino is a Majorana particle or not. If the neutrino is a Majorana particle, they provide important support for the seesaw mechanism [6], which naturally explains the anomalous lightness of the neutrino relative to other elementary particles, and for the leptogenesis model [7], which naturally explains the matter-dominated universe. Almost the only way to verify this is to observe neutrinoless double-beta decay.

1.2 Neutrinoless double beta decay

Beta decay is a phenomena in which a neutron decays in a nucleus by a weak interaction:

$$n \to p + e^- + \bar{\nu}_e. \tag{1.1}$$

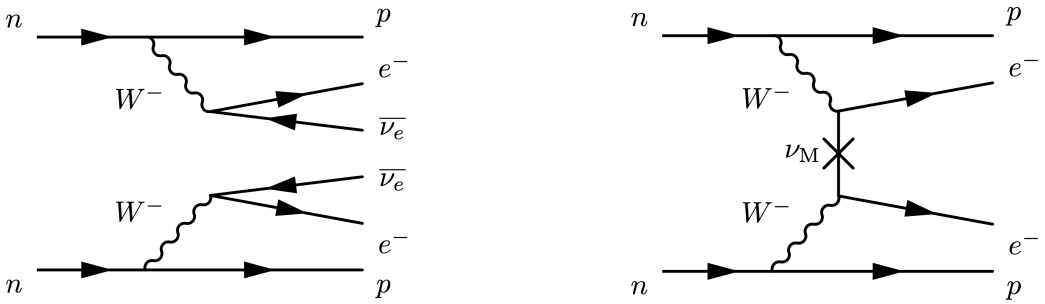

(a) $2\nu\beta\beta$ decay (b) $0\nu\beta\beta$ decay

Figure 1.1: Feynman diagrams of double beta-decays. In $0\nu\beta\beta$ decay, neutorinos are virtually annihilated in the nucleus, and only two electrons are emitted.

When a beta decay occurs, the nucleus changes its atomic number by plus one. For some nuclei, the transition to the neighboring nucleus is energetically forbidden, but that of two neighboring nucleus is energetically allowed. In such cases, a phenomenon called double beta-decay ($2\nu\beta\beta$ decay) occurs, in which two beta-decays happen simultaneously (Fig. 1.1a). The reaction of $2\nu\beta\beta$ decay is represented as

$$(A, Z) \rightarrow (A, Z+2) + 2e^- + 2\bar{\nu}_e, \tag{1.2}$$

where Z is atomic number and A is mass number.

Although the lifetime of $2\nu\beta\beta$ decay is very long ($10^{18} \sim 10^{21}$ years), it has been observed in several nuclei. For example, ^{44}Ca, ^{76}Ge, ^{82}Se, ^{130}Te, ^{136}Xe, ^{150}Nd are typical nucleus of double beta decay [8]. If the neutrino is a Majorana particle, there is a possibility of double beta decay without neutrinos ($0\nu\beta\beta$ decay) due to virtual annihilation of a neutrino and an antineutrino in the nucleus (Fig. 1.1b) Hence the observation of $0\nu\beta\beta$ decay is critically important to know whether the neutrino is a Majorana particle or not.

The lifetime,$(T^{0\nu}_{1/2})^{-1}$, is given as

$$(T^{0\nu}_{1/2})^{-1} = G^{0\nu}|M^{0\nu}|^2\langle m_{\beta\beta}\rangle^2, \tag{1.3}$$

where $G^{0\nu}$ is the phase-space factor, and $M^{0\nu}$ is the nuclear matrix element (NME). The effective neutrino mass is expressed as

$$\langle m_{\beta\beta}\rangle = \left|\sum_{i=1}^{3} U_{ei}^2 m_i\right|, \tag{1.4}$$

where U_{ei} are the first-row elements of the neutrino mixing matrix and m_i are neutrino masses.

The $2\nu\beta\beta$ decay and $0\nu\beta\beta$ decay have different spectra of two-electrons energy sum as shown in Fig. 1.2. The $2\nu\beta\beta$ decay has a contunuas spectrum. On the other hand, the $0\nu\beta\beta$

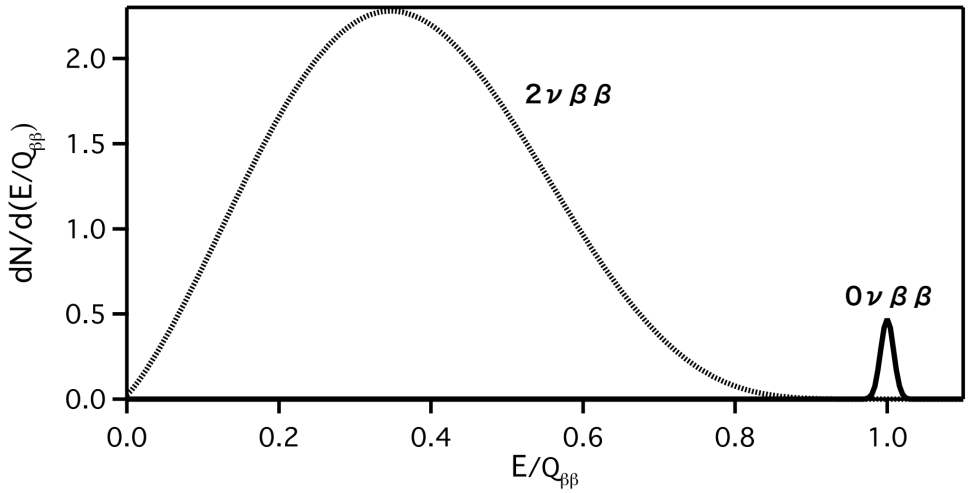

Figure 1.2: Spectrum of the sum of the energies of two beta rays from double-beta decays [10]. In $2\nu\beta\beta$ decay, since the energy is given to electrons and neutrinos, the energy spectrum is continuous. On the other hand, in the $0\nu\beta\beta$ decay, since the decay energy is given only for electrons, the energy spectrum has a sharp peak at Q-value. In this figure, the $0\nu\beta\beta$ spectrum is convoluted with finite energy resolution.

decay makes a peak at the decay Q-value since the total decay energy is all given to the two electrons. The $0\nu\beta\beta$ decay search is conducted by searching for this peak.

Allowed parameter space determined by neutrino oscillation experiments is shown in Fig. 1.3 as the green line and the red line [9]. The vertical axis is an effective mass of the neutrino, and the horizontal axis is the lightest neutrino mass. When neutrino masses are in the inverted order ($m_3 < m_1 < m_2$), the allowed region is shown as the green line. On the other hand, when neutrino masses are in the normal order ($m_1 < m_2 < m_3$), the allowed region is shown as the red line. It is not yet known which mass ordering the neutrinos are in.

Currently, KamLAND-Zen experiment gives the most strightest limit: $\langle m_{\beta\beta}\rangle < (36 - 156)\,\mathrm{meV}$ at the 90% C.L. [5]. Many experiments are aiming to reach $\langle m_{\beta\beta}\rangle = 20\,\mathrm{meV}$, which is the lower limit of the inverted order region. The expected event rate for $\langle m_{\beta\beta}\rangle = 20\,\mathrm{meV}$ is only a few events per year even if 1 ton of decay-nuclei is used. Therefore, a detector using ton-scale decay nuclei is required. Also, very low background contamination is required. Not only environmental radiation but also the $2\nu\beta\beta$ decay can be the background. Therefore, high energy resolution is important to distinguish the $0\nu\beta\beta$ and the $2\nu\beta\beta$ decay signals.

1.3 Examples of On-going Experiments

The most sensitive $0\nu\beta\beta$ decay searches have been performed with ^{136}Xe and ^{76}Ge. There are a few reasons: their natural abundance is relatively high (7.8% in xenon and 8.9% in germanium), and they can be enriched by centrifugation, and they can be used as a detector

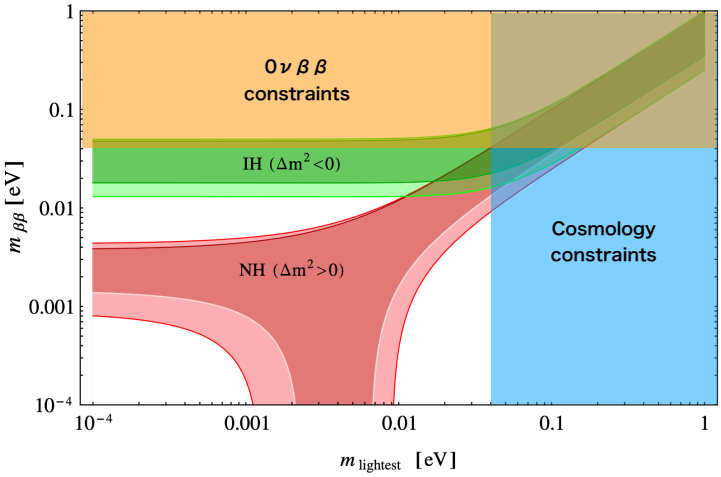

Figure 1.3: Allowed parameter region related to $0\nu\beta\beta$ decay. The vertical axis is the neutrino effective mass, and the horizontal axis is the lightes neutrino mass. The green line indicates inverted hierarchy and the red line indicates normal hierarchy. Constraints by $0\nu\beta\beta$ decay search experiments and cosmological observations are also drawn. [11]

component, i.e., scintillator or diode. In the following, representative experiments using ^{136}Xe and ^{76}Ge are introduced. In addition to the experiments introduced here, numerous other experiments are currently underway.

1.3.1 KamLAND-Zen Experiment

KamLAND-Zen is an experiment using ^{136}Xe as the double beta decay nuclei. The ^{136}Xe atoms are dissolved in a liquid scintillator, and the energy is measured by detecting scintillation light. By using 745 kg of enriched xenon, they recorded $T_{1/2} > 2.3 \times 10^{26}$ year, which corresponds $\langle m_{\beta\beta} \rangle < (36 - 156)$ meV [5]. Extremely low background has been achieved in the KamLAND-Zen experiment. However, the energy resolution is not so high, i.e., 10 % (FWHM) at Q-value. Their energy resolution is limited by the amount of the scintillation photons. Therefore, in addition to radioisotopes, contamination of the $2\nu\beta\beta$ decay is also an issue as a background source.

1.3.2 GERDA Experiment

The GERDA experiment uses ^{76}Ge as the double beta decaying nucleus. They use germanium semiconductors made with enriched ^{76}Ge as the detector and the decay nuclei. The characteristic feature of the germanium detector is the ultra-high energy resolution. They achieved 0.15 % (FWHM) at Q-value. By using about 35 kg of enriched germanium, they recorded $T_{1/2} > 1.8 \times 10^{26}$ year, which corresponds $\langle m_{\beta\beta} \rangle < (79 - 180)$ meV [12]. The subject of the germanium detectors is to fabricate large crystals.

1.4 Experiments based on Xenon Gas TPC

Here we present experiments using a high-pressure xenon gas time projection chamber (TPC) as a next-generation $0\nu\beta\beta$ decay search. A TPC uses an electric field to drift ionization electrons produced by radiation to the detection surface and reconstructs the radiation track based on the hit pattern and time. The energy deposit of the radiation can be determined from the number of detected electrons. Each of the experiments described below uses a unique method to detect ionization electrons. As described in Section 2.1, since fluctuation of ionization electrons is small in xenon, high energy resolution can be achieved in principle.

1.4.1 NEXT Experiment

The schematic view is shown in Fig. 1.4. The detector is filled with up to 15 bar of enriched ^{136}Xe gas. When xenon gas is ionized by beta rays, ionization electrons drift to the right side in Fig. 1.4 by the electric field. When the ionization electrons reach the electroluminescence (EL) region made with a two-conductor meshes, they are converted to multiple photons by the EL process described in Section 2.1. The energy is reconstructed by detecting them with the photo multiplier tubes (PMTs) shown in Fig. 1.4 left. Silicon photomultipliers (SiPMs) are placed in a two-dimensional configuration beside the EL region, and the event trajectory and position are reconstructed from the EL photon patterns observed by the SiPMs and the timing of the scintillation light when the event occurs.

They reported $0.91 \pm 0.07\%$ (FWHM) as the energy resolution with gamma rays of 2615 keV of ^{208}Tl [13], which corresponds 0.93% at Q-value when extraporated by $\sqrt{E}$. They also studied background identification using the difference of the event topology. They use a convolutional neural network for the background identification [14]. Because of these features, the NEXT experiment is expected to be the next generation experiment for the $0\nu\beta\beta$ search. A few flaws exist in this configuration. Since PMTs are far from the EL region, attenuation of light intensity and dependence of acceptances on the location of the event might limit the energy resolution. Since the EL electric field is formed by two meshes, mechanical supports could create insensitive area for the large detector.

1.4.2 PandaX-III Experiment

The PandaX-III experiment uses Micromegas for readout of ionization electrons. A quenching gas TMA (trimethylamine) is mixed with 1% in xenon gas to suppress diffusion during drift. The PandaX-III detector can reconstruct event topology with high resolution, but the energy resolution is not so high, about 3% (FWHM) at the Q-value, due to the use of avalanche amplification in the Micromegas. Also, since the scintillation light is suppressed by the TMA, it is impossible to reconstruct the absolute position in the drift direction of the event.

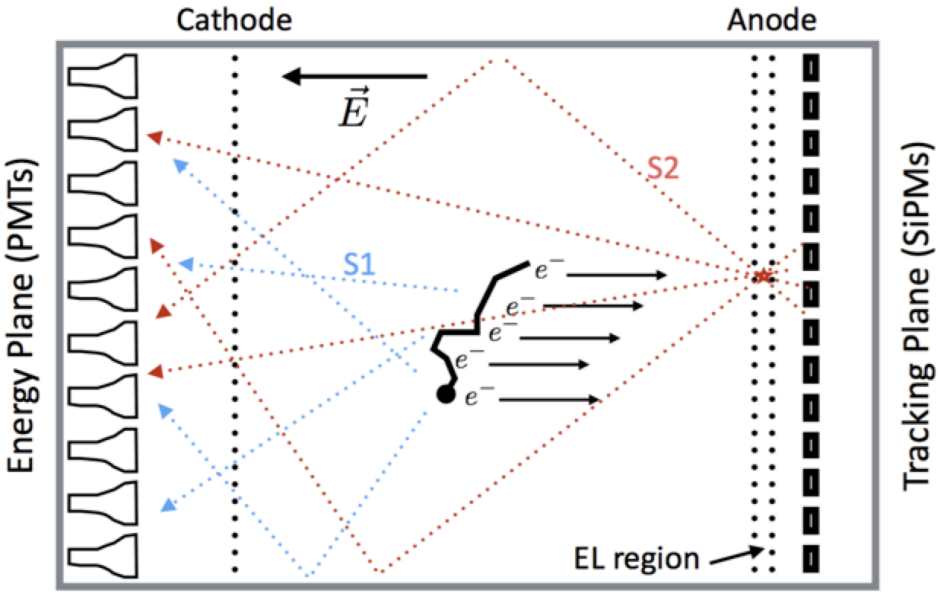

Figure 1.4: Schematic view of the NEXT detector. Enriched ^{136}Xe gas is filled in the pressure vessel. Scintillation photons (S1) are detected by PMTs. Ionization electrons are drifted to the EL region. In the EL region, ionization electrons generate photons (S2) with a strong electric field, which are detected by PMTs and tracking plane SiPMs. The energy is reconstructed by S2 detected by PMTs, and the event topology is reconstructed by the hit pattern in the tracking plane. [15]

1.4.3 AXEL Experiment

We proposed the AXEL project. In the AXEL detector, cellular readout structure, ELCC, is used to detect ionization electrons. The ELCC also utilizes the EL process. Since energy is also measured within the ELCC, it does not have a position dependence when properly designed. With a modular structure, it can be scaled up while keeping high energy resolution. We aim to achieve a high energy resolution, 0.5% FWHM at Q-value (2.5 MeV). Our target sensitivity is to reach $\langle m_{\beta\beta} \rangle = 20\,\mathrm{meV}$, which is the lower limit of the inverted mass order, by using a detector with 1 ton of enriched ^{136}Xe. To achieve this goal, it is necessary to establish technologies with scalability. We have constructed a 180L detector for this purpose. There observed some issues in the previous study, called phase 1. We updated the 180L detector to phase 2, and conducted the performance evaluation using 1.8 MeV gamma-ray of ^{88}Y.

1.5 Outline of This Thesis

The goal of this thesis is to establish the technologies of large TPC based on ELCC with which a high sensitive $0\nu\beta\beta$ search can be pursued. In Chapter 2, an overview of the AXEL experiment is described. From Chapter 3 to Chapter 5, compornents of the 180L detector in phase 2 is described. In Chapter 3, the upgrade of the ELCC is described. Front-end-electronics is described in Chapter 4, and the data acquisition system is described in Chapter 5. The calibration of MPPC is described in Chapter 6. In order to evaluate the detector performance, we conducted a measurement using 1.8 MeV gamma rays from a ^{88}Y source. The measurement condition is described in Chapter 7. The analysis and the result are described in Chapter 8. The result is discussed in Chapter 9. Finally, this thesis is summarized in Chapter 10.

Chapter 2

AXEL Experiment

2.1 Overview of the AXEL Experiment

AXEL (A Xenon ElectroLuminescence) is a project to search for neutrinoless double-beta decay using enriched ^{136}Xe gas as a decaying nucleus. Our target sensitivity is $\langle m_{\beta\beta} \rangle = 20\,\mathrm{meV}$. In order to achieve this target sensitivity with a few years of observation, at least one ton of decay nuclei is required. The background rate is required to be less than 1 events/year. We have been developing a high-pressure xenon gas Time Projection Chamber (TPC) which satisfies these requirements. A TPC is a gas detector in which electrons ionized by a charged particle are drifted to a detection plane by an electric field. Energy can be reconstructed from the number of detected electrons. Three-dimensional trajectories can be reconstructed by the position and the timing of the detected electrons.

A schematic view of the AXEL detector is shown in Fig. 2.1. An enriched ^{136}Xe gas is contained in a cylindrical vessel. The ^{136}Xe is a double-beta decay nucleus. Ring electrodes are stacked in the vessel to form an electric field. When a double-beta decay occurs in its fiducial volume, two beta-ray tracks deposit their energies by exciting and ionizing xenon gas atoms. Excited atoms produce scintillation by de-excitation, which is detected by photomultiplier tubes (PMT). Ionized electrons are drifted by the electric field to the detection plane placed on the opposite side of the PMTs. The detection plane is called an electroluminescence light collection cell (ELCC). A higher electric field is applied in the ELCC, so ionization electrons are collected into the cell and generate photons by the electroluminescence process as shown in Fig. 2.1 right. The photons are detected by silicon photomultipliers (SiPM) in the cell. The energy of beta rays is reconstructed from the number of photons detected and track patterns from the position and timing of the photons.

The intrinsic energy resolution is given by the statistical fluctuation of the number of ionizations and expressed as follows [16],

$$\frac{\Delta E\ (\mathrm{FWHM})}{E} = 2.355 \frac{\sqrt{FE/W_\mathrm{i}}}{E/W_\mathrm{i}}, \tag{2.1}$$

where E is the deposit energy in the midium gas, F is a Fano factor, and W_i is average energy loss per ionization. In general, the Fano factor is less than 1, and it means that the

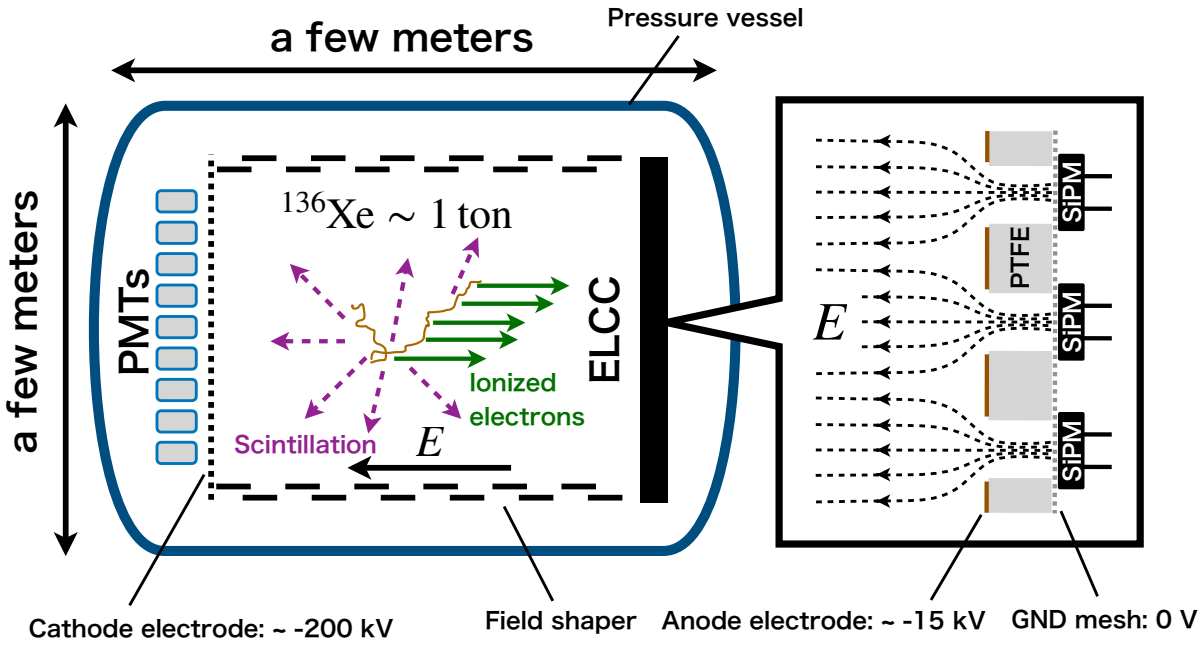

Figure 2.1: Schematic view of the AXEL detector. Enriched ^{136}Xe gas is filled in the pressure vessel. Scintillation photons (purple arrows) are detected by PMTs. Ionization electrons are drifted to the detection plane (ELCC). In the ELCC, ionization electrons are further accelerated by a strong electric field and generate photons, which are detected by SiPMs. From the hit pattern and the number of observed photons, event topology and energy are reconstructed.

ionization process is not entirely random. In the case of the xenon gas, $W_{\rm i}$ is 22.1 eV, and F is 0.13 [16], which is relatively small compared to other noble gas atoms. Then, the intrinsic energy resolution is 0.25% (FWHM) at 2.5 MeV, the Q-value of the $0\nu\beta\beta$ decay. We aim at the energy resolution of 0.5%. To achieve this, suppressing other effects less than 0.43% is required.

The electroluminescence (EL) process is described as follows [16],

$$\begin{aligned} e + A &\rightarrow e + A^* \\ A^* + 2A &\rightarrow A_2^* + A \\ A_2^* &\rightarrow 2A + h\nu, \end{aligned} \tag{2.2}$$

where e is an electron, A is an atom, $h\nu$ is a photon produced by the EL process. The excited state of A is expressed with an asterisk. The wavelength of the xenon EL light is $150 \sim 180$ nm [16]. Light of this wavelength is called vacuum ultraviolet (VUV) since it attenuates rapidly in the atmosphere. The number of photons emitted by the EL process (EL yield) is given by an empirical formula [17]

$$Y_{\rm EL}/p = 140\, E/p - 116, \tag{2.3}$$

where $Y_{\rm EL}$ is the photon yield during 1 cm electron drift, p is a gas pressure in bar, and E/p is a reduced electric field in units of kV/cm/bar. Since the EL process produces photons only from initial electrons, the fluctuation of the photon generation is small compared to the avalanche amplification, and hence a good energy measurement is expected. Also, the ELCC has a rigid structure, which is advantageous to make a large detector.

The candidate of the main background for $0\nu\beta\beta$ decay search by using ^{136}Xe is 2,447 keV gamma-ray from ^{214}Bi contained in the pressure vessel. The energy difference from the Q-value is only 11 keV, which corresponds to 0.45% of the energy of the Q-value. This means that backgrounds remain even if the target energy resolution, 0.5% (FWHM) at Q-value, is achieved. By a simulation study, the background rate in the region of interest (ROI) is estimated at about 100 events/year for a 1-ton detector. Our strategy to remove this background is to use the event topology. Since the $0\nu\beta\beta$ decay has two electron tracks, it has two endpoints. On the other hand, the absorption event of gamma-ray makes a single electron track, which has only one endpoint. At around the endpoint, an electron loses more energy, and many atoms are ionized. So the endpoint has a blob pattern. By distinguishing events with this feature, background events can be reduced. Deep learning is a good solution to distinguish $0\nu\beta\beta$ events from background events. A simulation study has shown that background events can be reduced by less than 1/100, i.e., less than 1 events/year. We estimate that we can reach $T_{1/2} > 10^{27}$ years with 6 years of observation with a 1-ton detector that achieves an energy resolution of 0.5%. This corresponds to $\langle m_{\beta\beta}\rangle < (19.77-53.56)$ meV, which reaches the lower limit of the inverted hierarchy region.

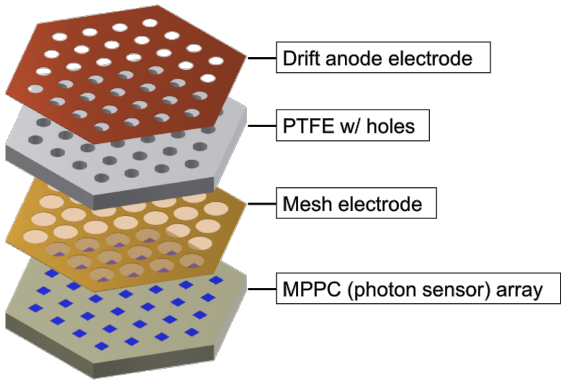

Figure 2.2: The structure of the ELCC. ELCC cell is configurated with a hexagonal layout so that the distance from the neighboring cell is equal. PTFE is used to increase the EL yield by reflecting EL photons in the cell.

2.2 Optimization of the ELCC design

We optimized the design of the ELCC by a simulation [18]. The important point of the design is as follows.

- The correction efficiency of electrons is sufficiently higher than 99.5%.
- The position dependence of the EL gain is sufficiently small.

On the simulation, EL electric field is fixed at 3 kV/cm/bar, and the depth of the cell hole is fixed at 5 mm. Sufficient EL gain can be obtained without an excessively high voltage under this condition. A hexagonal layout is adapted on the ELCC cell as shown in Fig. 2.2 so that the distance from the neighboring cell is equal. The cell pitch and the aperture ratio of the cell are optimized.

As a result, 10 mm pitch and 5.5 mm holesize is adapted. A Initial position dependence of ionization electrons of EL gain is shown in Fig. 2.3. The red circle in Fig. 2.3a represents a hole of the ELCC cell. Applying this fluctuation, the energy resolution at 30 keV is 3.46% (FWHM), which is sufficiently small compared to the required value of 4.52% (FWHM) to achieve 0.5% (FWHM) at the Q-value.

2.3 Roadmap of AXEL Project

We are aiming to achieve our target sensitivity $\langle m_{\beta\beta} \rangle = 20$ meV with a ton-scale detector. Toward this goal, we had started with a small prototype detector. The roadmap of the AXEL project is shown in Fig. 2.4. The ELCC principle was demonstrated in the 10L prototype. We obtained en energy resolution of $2.54 \pm 0.20\%$ (FWHM) at 356 keV, which corresponds $0.82 \pm 0.038\%$ (FWHM) at Q-value [18]. The main purpose of the next prototype, the 180L

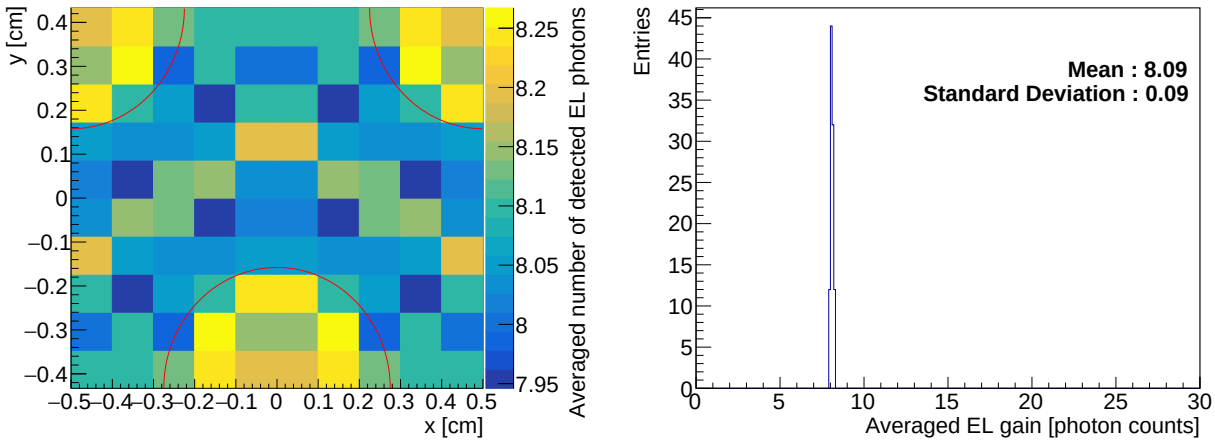

(a) (b)

Figure 2.3: (a) EL gain map for each initial electron position. The red circule represents a hole of the ELCC cell. (b) Distribution of EL gain. [18]

detector, is to establish technology to scale up the detector and demonstrate the energy resolution around the $0\nu\beta\beta$ Q-value. Studying track pattern recognition is another purpose of the 180L detector. Details and the current status of the 180L detector are described in section 2.4. With the 1,000L detector, we aim to conduct a $0\nu\beta\beta$ search. Currently, we are selecting detector components for the 1,000L detector to achieve a low RI level.

2.4 180L Detector

The 180L detector can have ELCC of up to 1,500 channels and the drift length of up to 50 cm. In order to realize such a large ELCC plane, the ELCC is modularized with 56

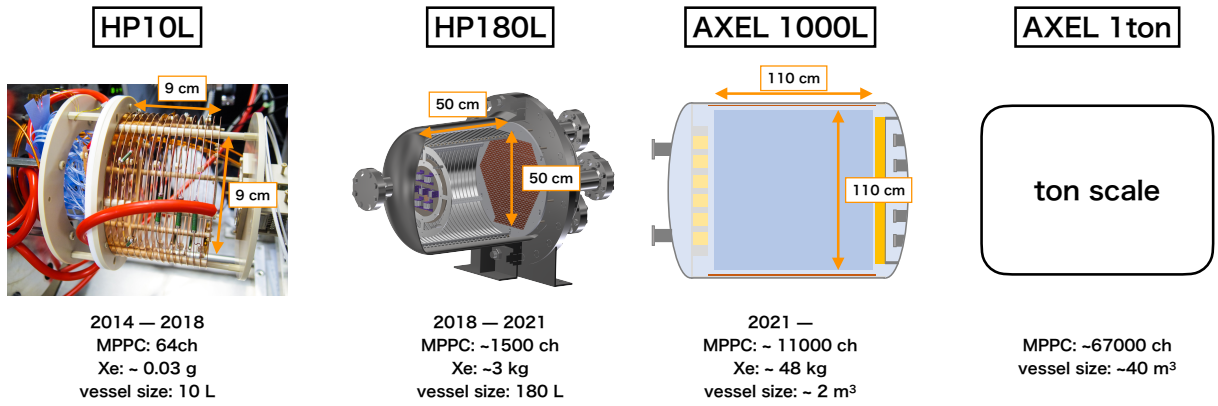

Figure 2.4: Roadmap of the AXEL porject.

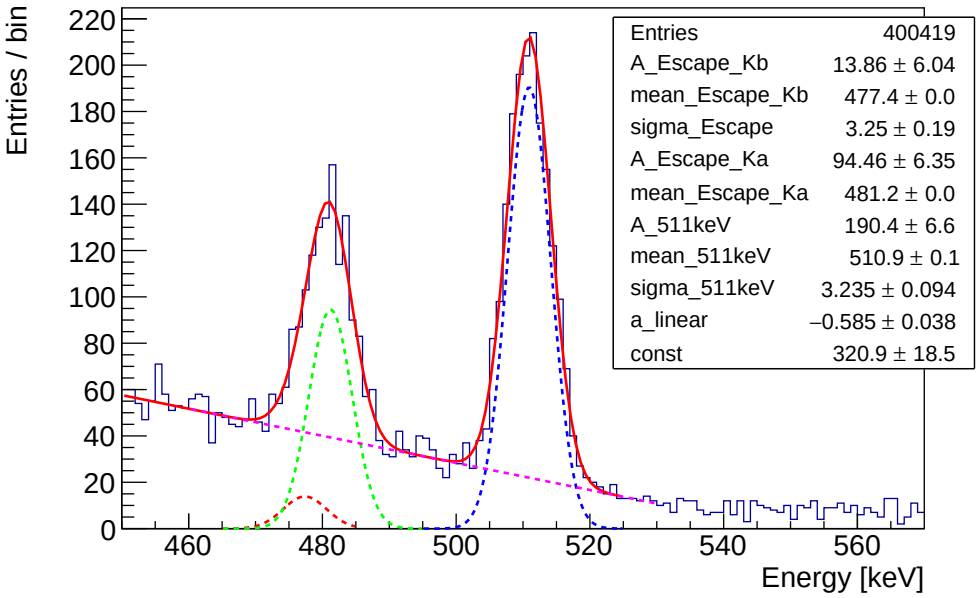

Figure 2.5: Energy spectram obtained in phase 1 of the 180L size prototype. A ^{22}Na soource was used. The blue dashed line is the full peak of the 511 keV and the green dashed line is the escape peak of the K_α (481.2 keV) and the red dashed line is the escape peak of the K_β (477.4 keV). [18]

channels, which is called an ELCC module.

We started performance evaluation with three ELCC units (168 channels) as a phase 1. In the phase 1, we conducted a measurement with a 511 keV gamma-ray's from a ^{22}Na source, and obtained $1.73 \pm 0.07\%$ (FWHM) energy resolution at 511 keV, which corresponds to $0.79 \pm 0.03\%$ (FWHM) at the Q-value (Fig. 2.5). In phase 1, we could not conduct measurement more than 4 bar xenon because of a discharge in the ELCC. In order to conduct a measurement with the target gas pressure (8 bar), solving discharge in ELCC is the most important subject of phase 2.

In this thesis, we updated the design and installed twelve ELCC modules (672 channels) as a phase 2. In phase 2, we conducted the performance evaluation with 1.8 MeV gamma-ray from a ^{88}Y source. Components of the 180L detector are briefly described in the following. Further details are described in [18] and the details of the ELCC design and production in Chapter 3.

2.4.1 Detector Size

The vessel of the 180L detector is shown in Fig. 2.6. It is made of stainless steel. The diamiter is 55 cm, and the length is 83 cm. ELCCs are placed at the flange side, and the PMTs are at the backside in the vessel.

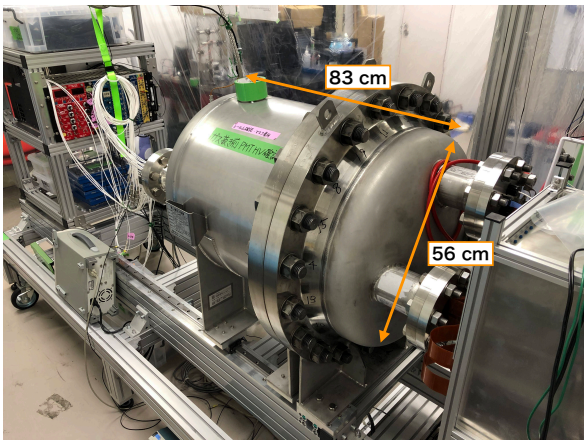

(a)

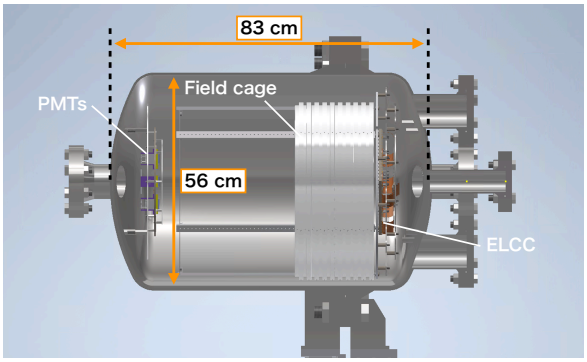

(b)

Figure 2.6: Detector view and crossectional view of the 180L detector.

2.4.2 Field Cage

A field cage is shown in Fig. 2.7. The field cage is made of aluminum. The diamiter is 50 cm, and the drift length is 18 cm. In the field cage, double strip electrode structure is adapted.

2.4.3 PMT

Figure 2.8 shows the installed PMTs. Seven PMTs are installed. We use R8520-406 manufactured by HAMAMATSU PHOTONICS K.K.. It has a sensitivity to VUV light and hence to scintillation light of the xenon gas ($\sim$ 179 nm). It can be used in high pressure xenon gas.

2.4.4 High Voltage

The high voltages for the anode electrode and the cathode electrode are supplied by HFR-10-20N and HFR-10-30N by Matsusada Precision Inc., respectively. The voltage supply for each stage of the field cage is provided by dividing the high voltage to the cathode by a resistor. Power supplys are connected from outside the chamber via a feed-through.

2.4.5 Gas System

A shcematic view of the gas system is shown in Fig. 2.9. The gas was purified during the measurement through the green line. A molecular sieve filter and a getter is used for the purification. The molecular sieve removes H_2O, O_2, CO, CO_2, H_2, NMHC from xenon gas. We used 250C-V04-I-FP manufactured by ARM Purification as the molecular sieve. In order to remove N_2, getter is used. We used a getter purifier for xenon gas manufactured by Nippon API Co., Ltd. The gas purity is monitored by a dew-point meter. We used PURA manufactured by Michell Instruments Ltd. as the dew-point meter.

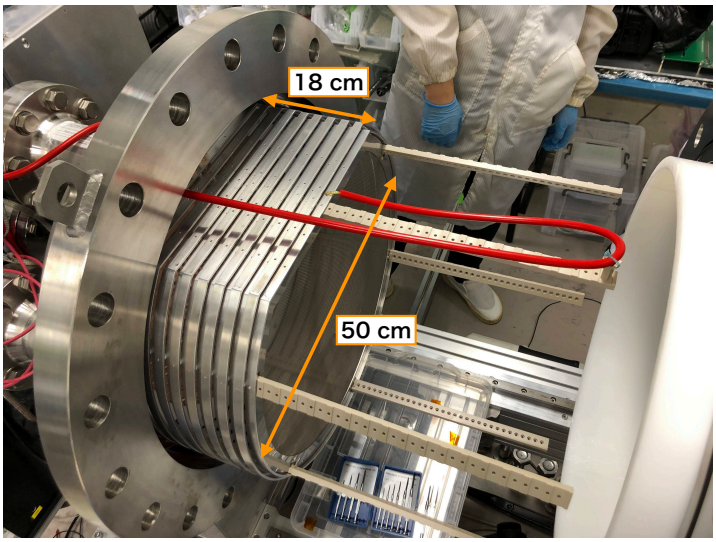

Figure 2.7: Installed field cage.

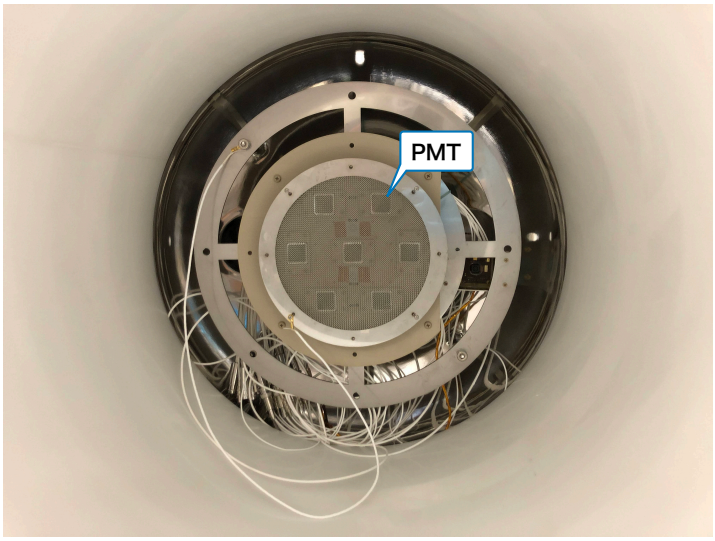

Figure 2.8: Installed PMTs.

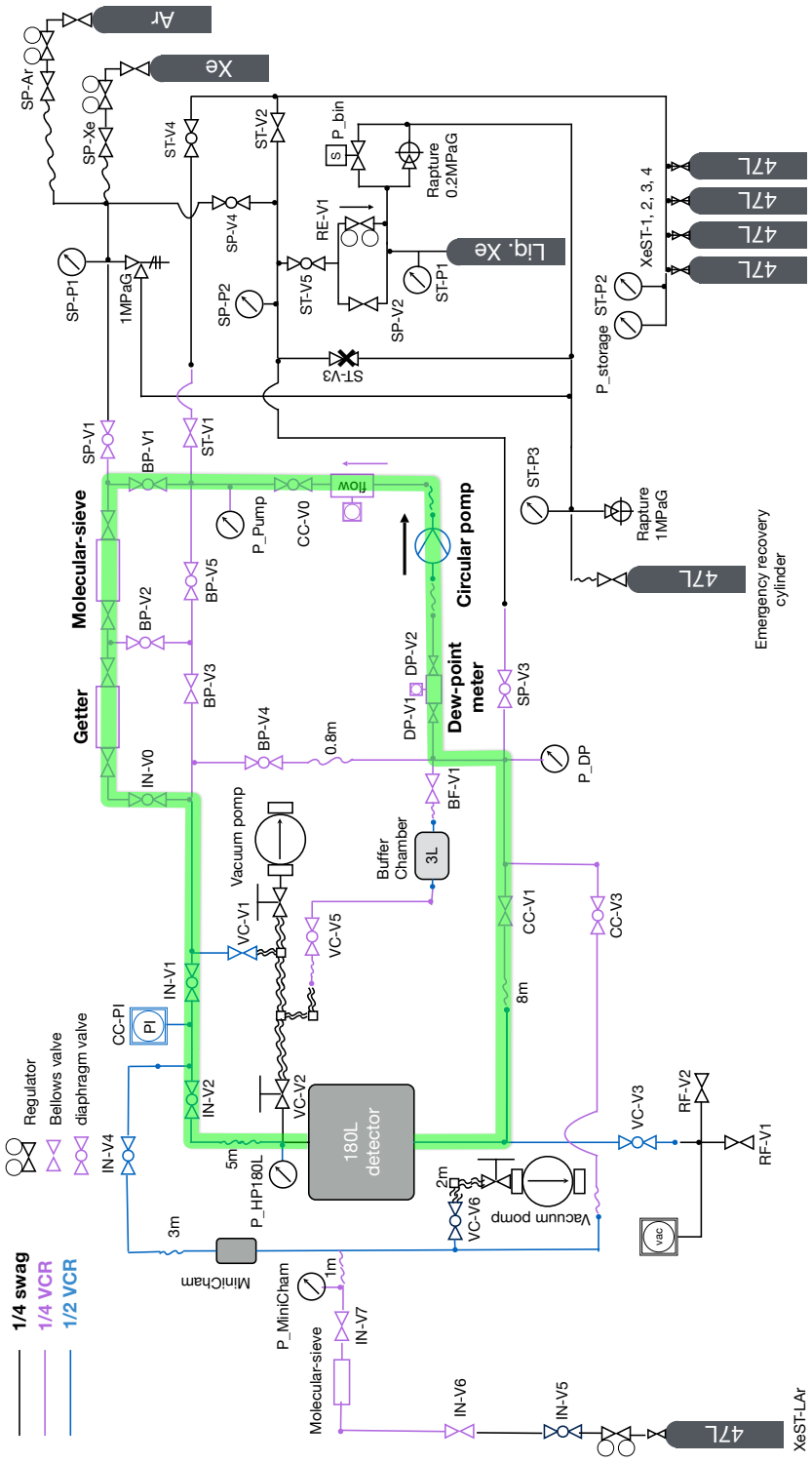

Figure 2.9: Shematic view of the gas system. The gas was purified through the green line during the measurement. A molecular sieve filter and a getter is used for the purification.

Chapter 3

Establishment of ELCC Technology

The most challenging part of the ELCC realization is to apply the required high voltage. The target reduced electric field is 3 kV/cm/bar, which corresponds to 12 kV at 8 bar. In this chapter, issues identified in phase 1 of the 180L detector and the measures taken for phase 2 are described.

3.1 Overview of the ELCC for the 180L Detector

Fig. 3.1a shows the top view of the ELCC plane in phase 2. The copper plate in front is the anode electrode for forming the EL electric field. The ELCC plane consists of 3 modules in phase 1 and 12 modules in phase 2. One module consists of 56 cells (Fig. 3.1b). As the SiPMs, we use a Multi-Pixel Photon Counters (MPPC) manufactured by HAMAMATSU PHOTONICS K.K.. MPPCs of an ELCC module are connected to a read out digitizer, AxFEB, outside the chamber via a flexible-print-circuit (FPC) cable.

3.2 Issues Identified in Phase 1

In phase 1, it was not possible to apply sufficient voltage under high xenon gas pressure. Following issues were identified in phase 1.

- Discharges through the screw holes to fix ELCC modules to the frame (Fig. 3.2)
- Discharges induced by a filament of the ground mesh having contaminated into a cell (Fig. 3.3)
- It is difficult to pin down the position of discharges that have not left black traces.

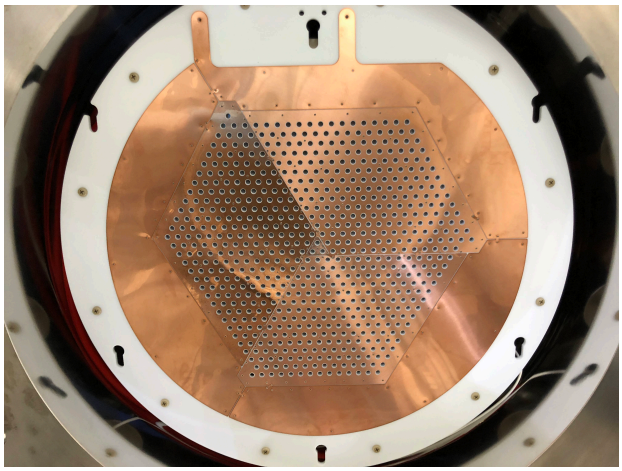

(a)

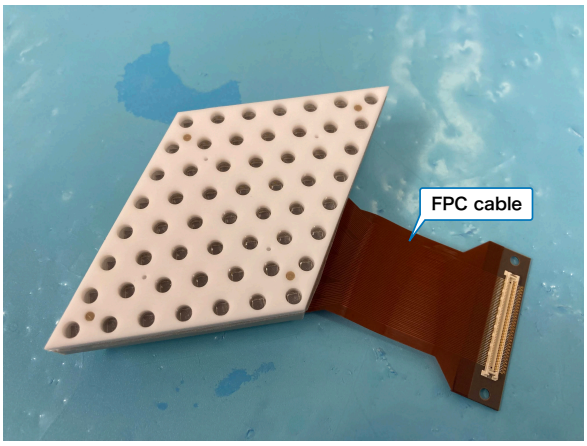

(b)

Figure 3.1: (a) Top view of the ELCC in phase 2. The copper plate in front is the anode electrode for forming the EL electric field. The ELCC in phase 2 consists of 672 channels of MPPC and it consists of 12 units of ELCC module. (b) Single ELCC module. The ELCC module consists of 56 cells. A MPPC is attached to each cell. Their signals are readout via a FPC cable.

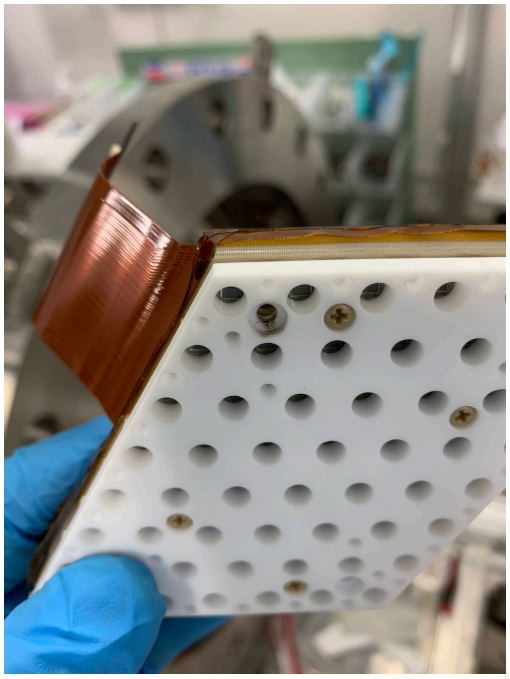

Figure 3.2: The ELCC module that had been discharged. Black traces of discharge is seen at the screw hole for fixing the ELCC module to the frame.

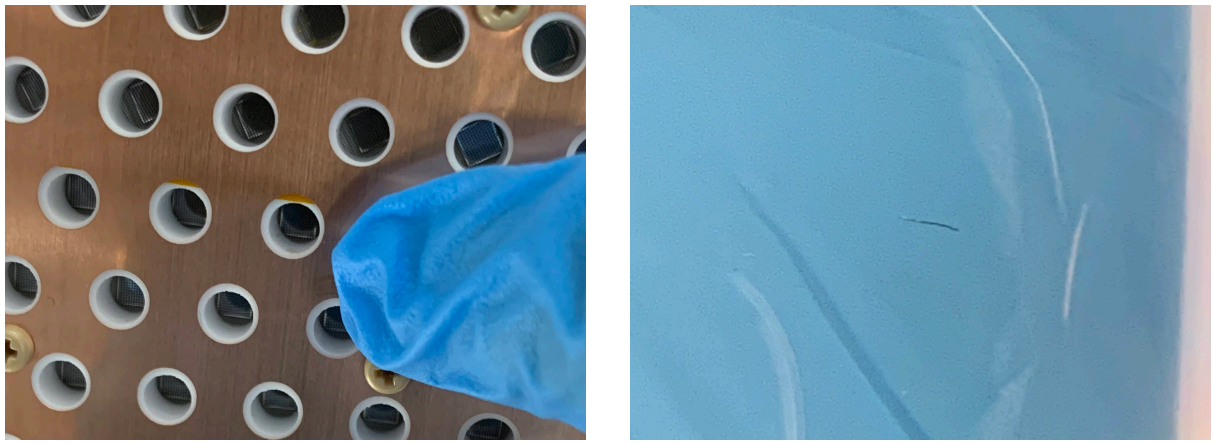

(a) (b)

Figure 3.3: (a) Filament of the ground mesh having contaminated into the cell. (b) Extracted filament of the ground mesh.

3.3 Design and Production of ELCC for Phase 2

3.3.1 Countermeasures for Electrical Discharge

Identification of Discharge Points

In order to identify discharge points, we installed a USB camera inside the detector and built a system to record the moment of discharge. A USB camera module ELP-USB13MAF-V75-J manufactured by Ailipu Technology Co., Ltd. is used. In order to suppress outgassing, the USB camera was potted in a case with epoxy resin for vacuum application as shown in Fig. 3.4a. The case is made of stainless steel, not aluminum, to supress outgassing. The USB cable is replaced with a vacuum-compatible polyimide insulated cable. The camera was installed on the PMT mount as shown in Fig. 3.4b. Camera images are recorded only at the moment of discharge by a motion detection, application "motion"[19].

Figure 3.5a shows a discharge recorded by this system. From the obtained discharge records, it was revealed that discharge positions were concentrated at module boundaries. Especially discharges particularly happened at the periphery of the modules, which is indicated by the blue region in Fig. 3.5b. The reason is understood that there is no GND electrode on the back of the periphery as shown in Fig. 3.5c. This caused the electric field to be concentrated.

Structure Ingenuity of ELCC

When a conductor and two insulators with different dielectric constants intersect at a single point, that point is called a triple junction. In general, electric field lines concentrate, and secondary electrons can be emitted from the conductor surface there. Therefore, triple junctions are weak to electrical discharge, especially when the electric field direction is parallel

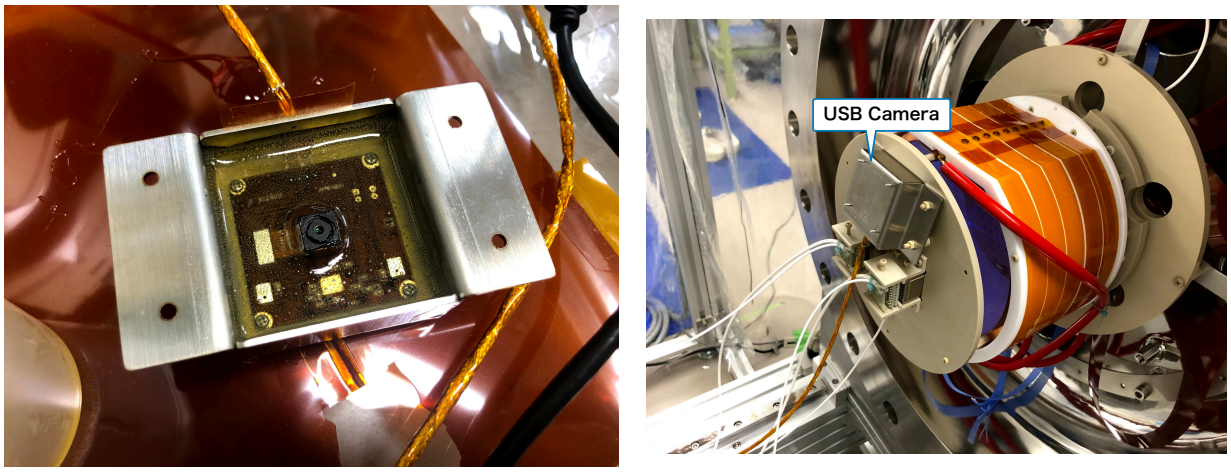

(a) (b)

Figure 3.4: (a) USB camera potted with epoxy resin in a stainless steel case. (b) USB camera installed on the top of the cathode plate.

to the insulator surface. In ELCC, the copper electrode, PTFE plate, and xenon gas make triple junctions. The screw holes fixing an ELCC module shown in Fig. 3.6 are found to be weak to discharge. In the new design, modules are fixed by plugs in stead of screws as shown in Fig. 3.7a so that penetrating hole is not necessary. One of the four electrode plugs is used to give the ground potential to the mesh as shown in Fig. 3.7b.

To avoid the concentration of electrical flux lines at the periphery of the ELCC module, a ground electrode was added at the back of the periphery, as shown in Fig. 3.8. In addition, in order to prevent discharge at module boundaries, the ELCC structure was changed. Now, the 5 mm PTFE-plate making cells are divided into two 2.5 mm-thick plates. The anode electrode and the top half of the PTFE plate are separated from the module. They cover multiple modules. Their shape and position are arranged so that their boundaries are displaced from those of ELCC modules, as shown in Fig. 3.9. Since there still remains overlaps of the module boundary and the cover boundary (shown as blue circles in Fig. 3.9), a 125 μm polyimide sheet is inserted between the modules and the cover to prevent discharge at these points. Three polyimide sheets shown as brown polygons in Fig. 3.9 are arranged to cover the blue circles. The withstand voltage of 125 μm thick polyimide is about 50 kV, which is sufficiently large compared to the maximum voltage of 12 kV between an anode and the mesh.

In summary, the cross sectional view of the new ELCC is shown in Fig. 3.10.

Countermeasures against Mesh Fraying

In order to prevent the mesh from fraying, this time, the mesh is sandwiched between two perfluoroalkoxy alkanes (PFA) films and welded together. The mesh is made of stainless steel wires with a diameter of 0.03 mm and its aperture ratio is 77.8%. It is cut to the A5 size. The thickness of the PFA film is 100 μm. The PFA film is cut to have holes at the cell position and the connection point to the ground. The mesh and the PFA films are attached as shown

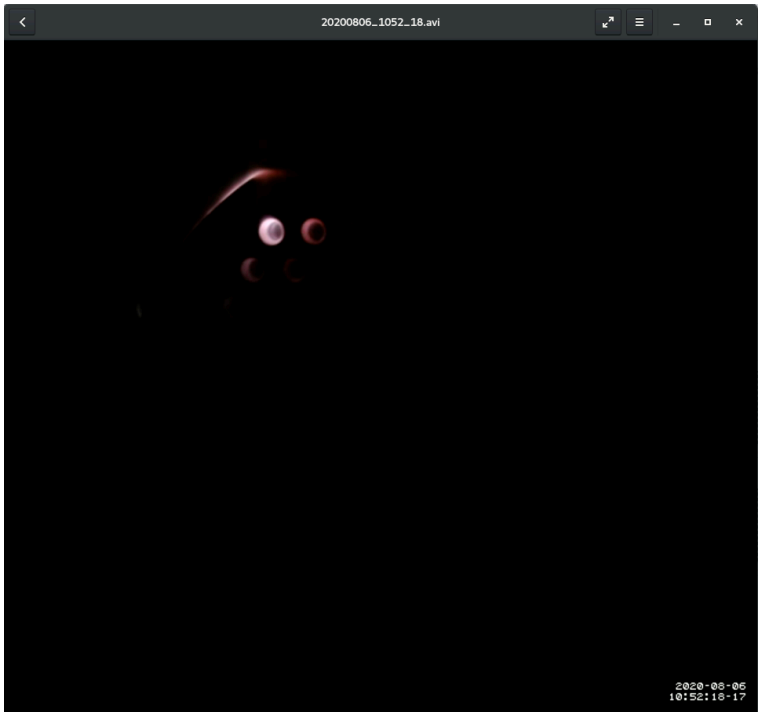

(a)

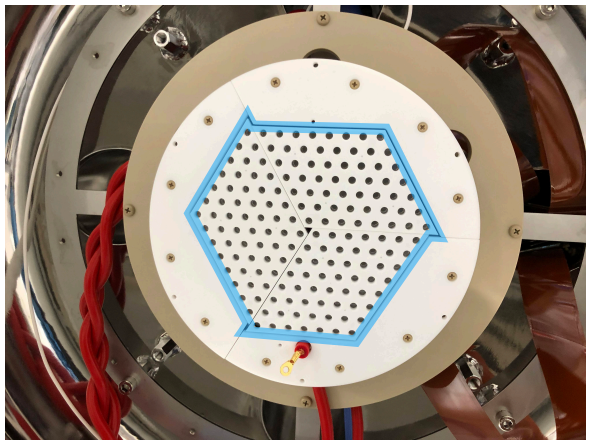

(b)

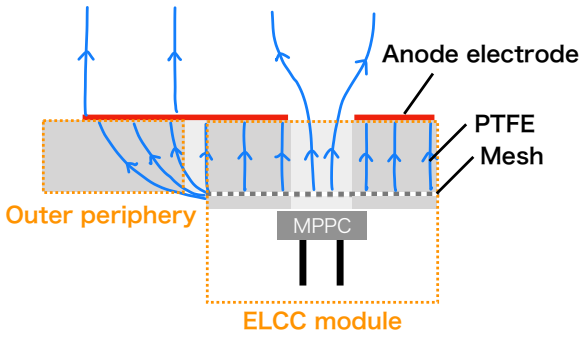

(c)

Figure 3.5: (a) Example image of a discharge recorded by the camera system. (b) The discharge points were particularly concentrated at the region indicated by the blue line. (c) Cross sectional view of the ELCC plane. There was no GND electrode on the back of the periphery of the module, which caused the electric field to be concentrated.

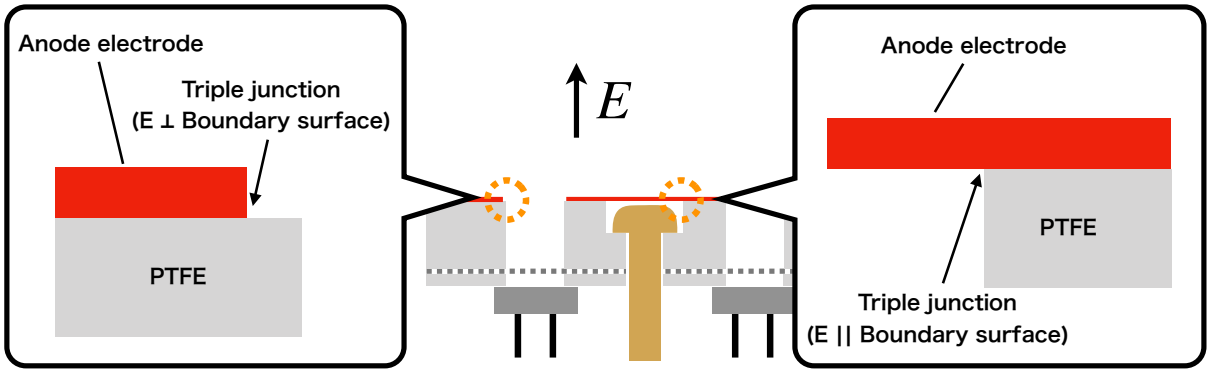

Figure 3.6: Since the interface between xenon gas and PTFE is parallel to the electric field, screw holes fixing the ELCC module are less susceptible to the canceling effect of the electric field by charge-up than cell sections. Therefore, discharge is more likely to occur in screw holes than in cell sections.

in Fig. 3.11, then laser-welded at the areas shown in Fig. 3.12a and cut with a Thomson mold to improve cutting accuracy and productivity. The mesh direction is arranged to limit the areas where fraying could start to the area indicated by the blue circles in the figure, rejecting a possibility of fraying happens along lines. Fig. 3.12b shows the welded mesh after the cutting.

3.3.2 Other improvements

ELCC Quality Control System

An ELCC quality control system was developed in order to verify the assembled ELCC modules. An ELCC module is set in a light-shielded plastic box as shown in Fig. 3.13b. AxFEB is used for the signal readout electronics. Each channel is connected via a jumper pin, so that if one MPPC fails and bias voltage can not be applied, that channel can be identified by disconnecting at the jumper pin.

Countermeasures aginst Contact Failure of the FPC Connector

Signals of the ELCC module are connected to AxFEB via FPC cable. A connector by HIROSE ELECTRIC CO., LTD. is used for the FPC cable connector. FX11LA-116P-SV is used on the ELCC module side and Fx11LA-116S-SV on the AxFEB side. In phase 1, failures of the connector contact occurred frequently. The reason is understood to be due to warped connectors or connectors not aligned in parallel. Therefore, we took measures using PEEK spacers and covers as shown in Fig. 3.14. The spacers keep connectors in parallel. Its thickness is 1.9 mm, which is decided by measuring the gap between the connectors. The purpose of the cover is to avoid the warping of the connecter. In order to hold sufficient

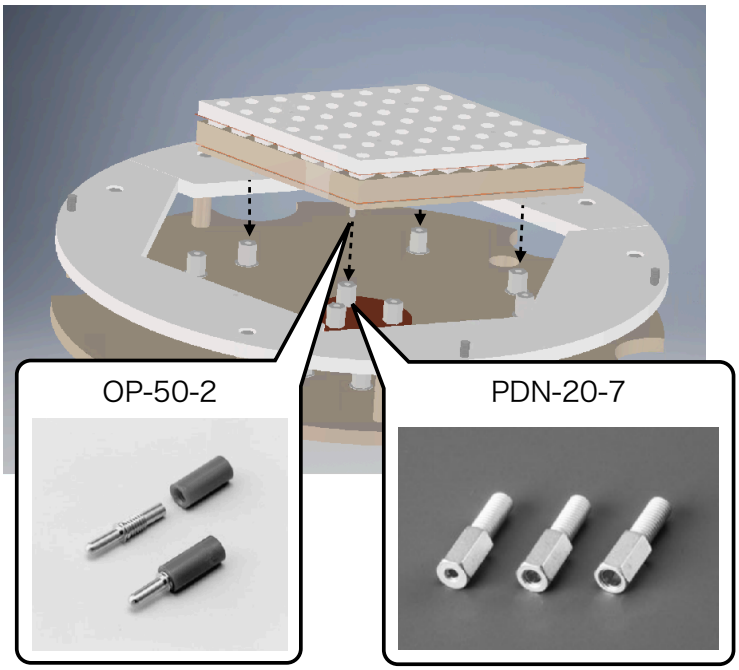

(a)

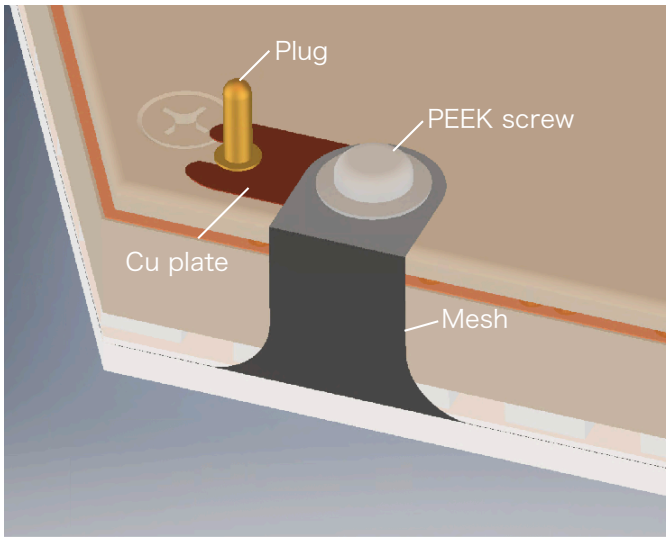

(b)

Figure 3.7: (a) ELCC is fixed by plugs. (b) Behind view of the ELCC. One of the four electrode plugs is used to give the ground potential to the mesh.

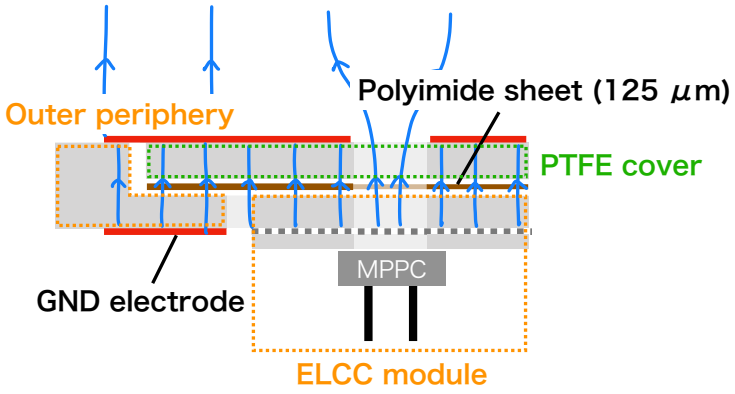

Figure 3.8: A ground electrode is added at the back of the periphery in order to prevent the concentration of electrical flux lines in the periphery of the ELCC module. In addition, a covered structure is adapted in order to prevent discharge at the module boundary.

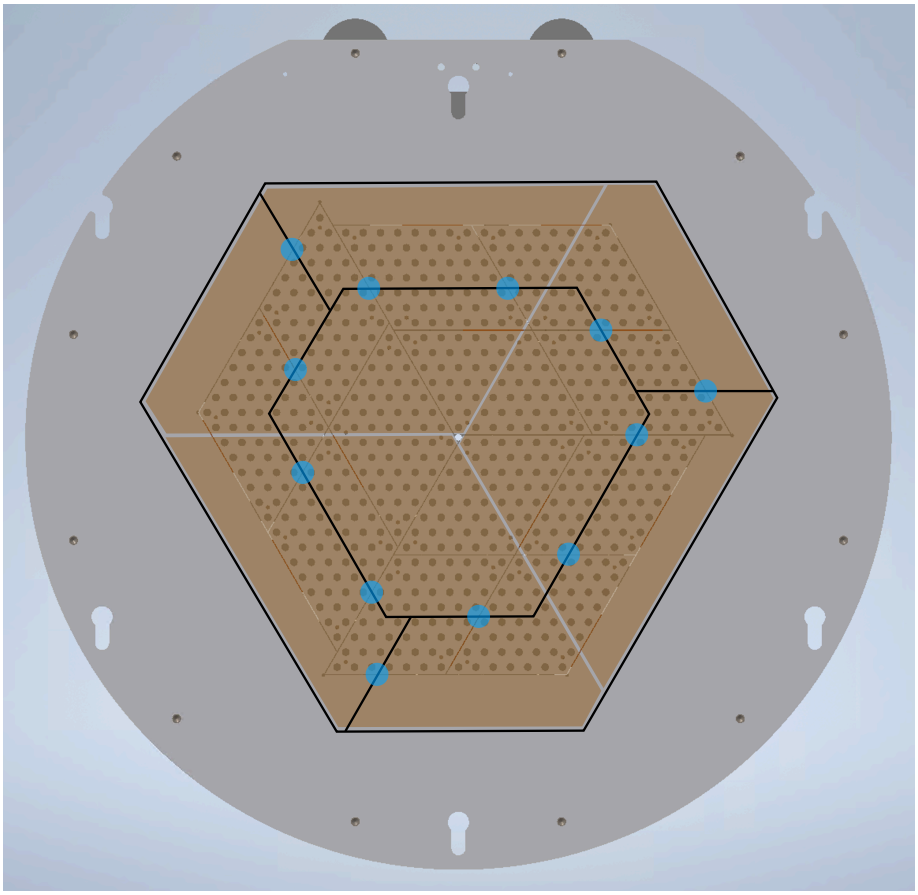

Figure 3.9: Black line indicates the boundary of the cover. It is displaced from the boundary of ELCC modules. Blue circles indicate the intersection of the module boundary and the cover boundary. Broun polygons are polyimide sheets placed so that the intersections are covered.

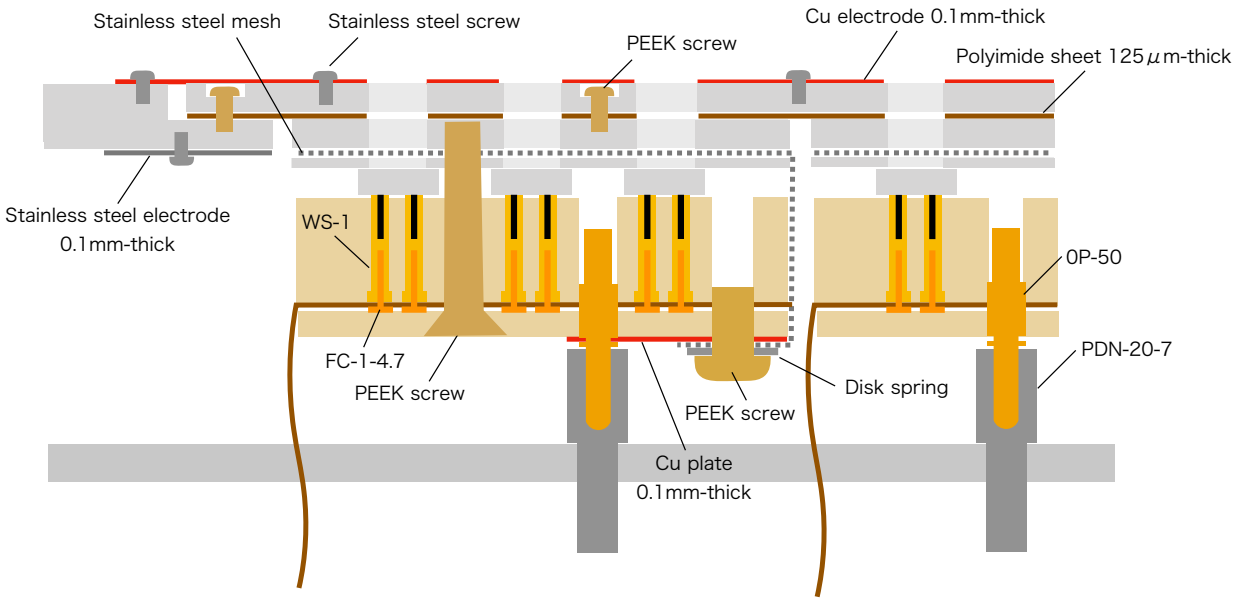

Figure 3.10: Cross sectional view of the ELCC.

strength, 3 mm-thick is adapted for the cover. Also, the other purpose of the spacer is to fix the FPC cable temporarily, as shown in Fig. 3.15.

Countermeasures against Disconnection of the FPC cable

In phase 1, the FPC was often broken at the area shown as the orange rectangle in Fig. 3.16a. The connector FPC is reinforced with a 0.5 mm-thick polyimide plate at the connector. The coverlay of the FPC ends before the plate. When the connector part is bent, as shown in Fig. 3.16b, the coverlay bites into and cuts the copper wire. Therefore, we changed the design of the connecter part (Fig. 3.17). By making 5 mm overlapping area for the polyimide plate and the coverlay, the disconnection due to the connector bending is prevented.

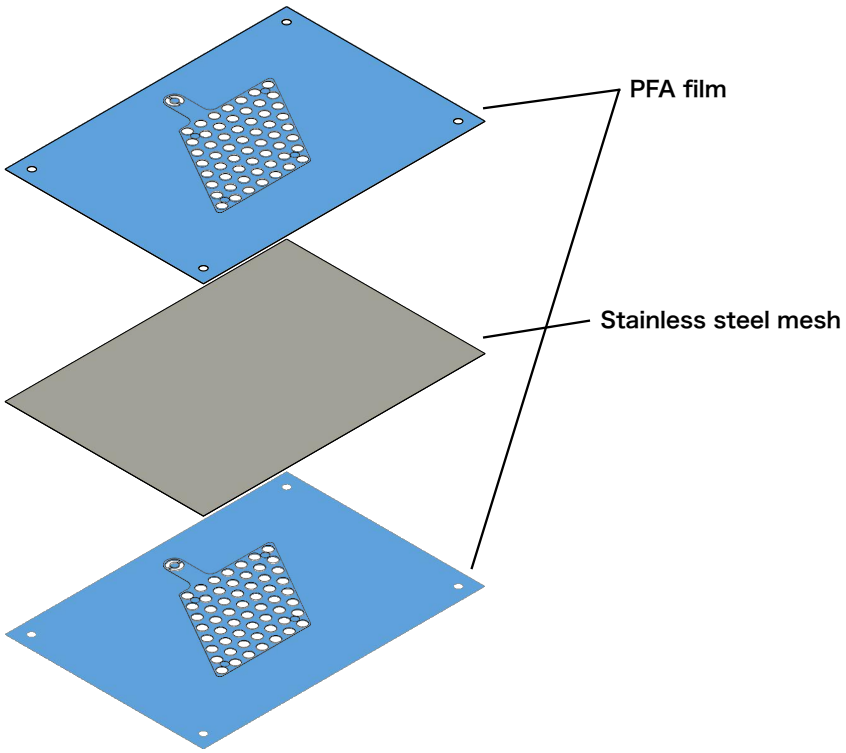

Figure 3.11: A mesh sheet is sandwiched between PFA films and laser-welded.

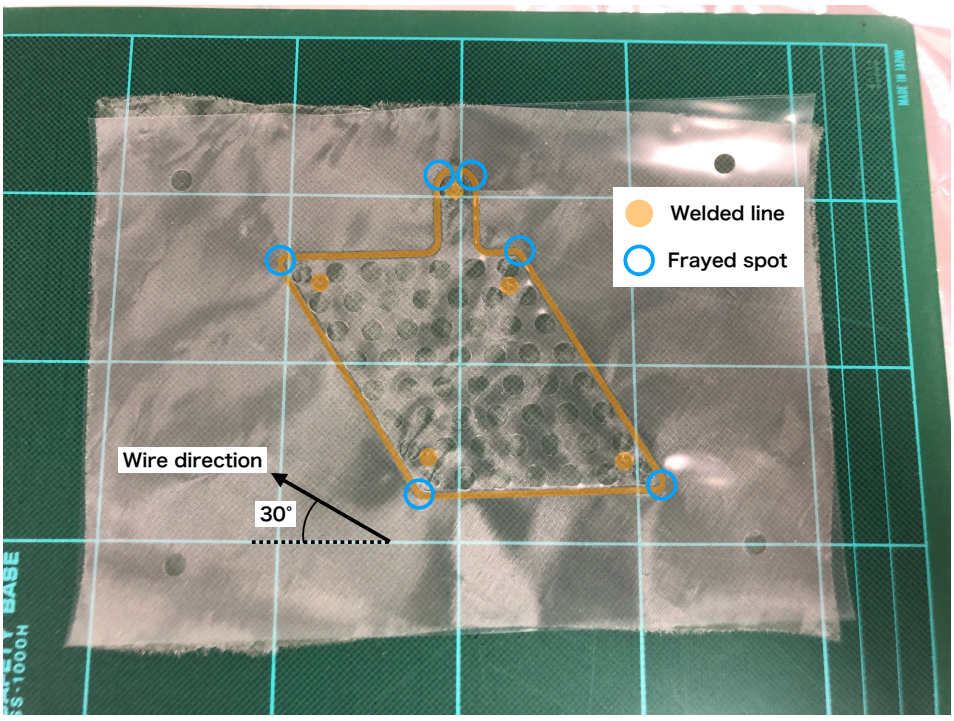

(a)

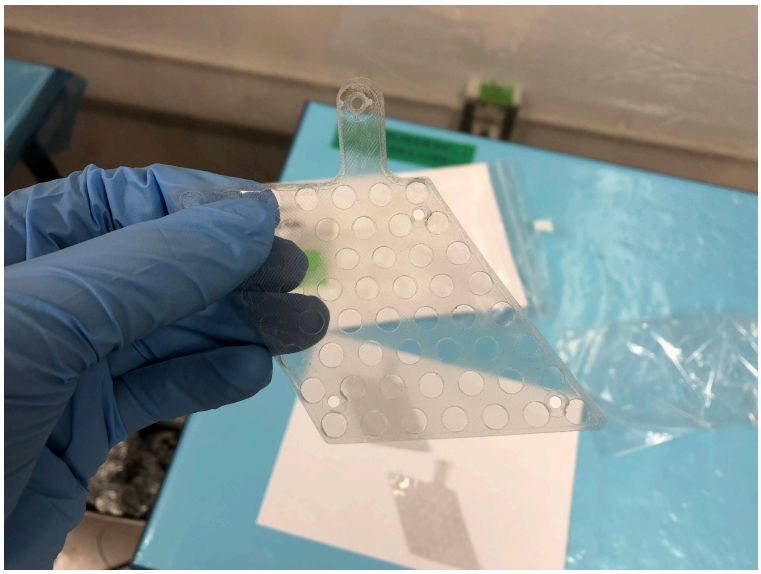

(b)

Figure 3.12: (a) Mesh and PFA sheets. They are welded along the line indicated by the orange line. The areas where fraying could start is limited to the blue circle points. (b) Cut welded mesh. Welded mesh is cut with a Thomson mold to improve cutting accuracy and productivity.

(a) (b)

Figure 3.13: (a) ELCC quality control system. An assembled ELCC can be checked quickly by the system. (b) ELCC set in the black box.

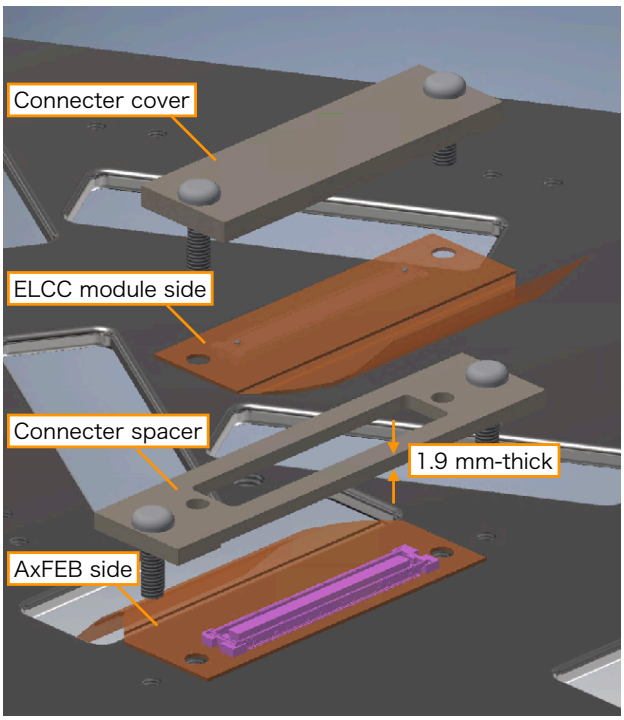

Figure 3.14: FPC cable connection. In order to ensure the connection, a spacer and a cover support the connection.

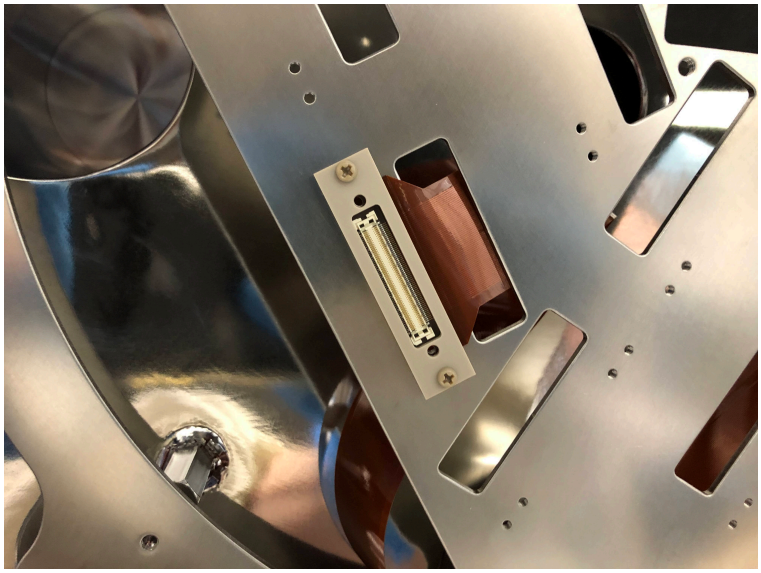

Figure 3.15: Connecter spacer fixes the FPC cable temporarily.

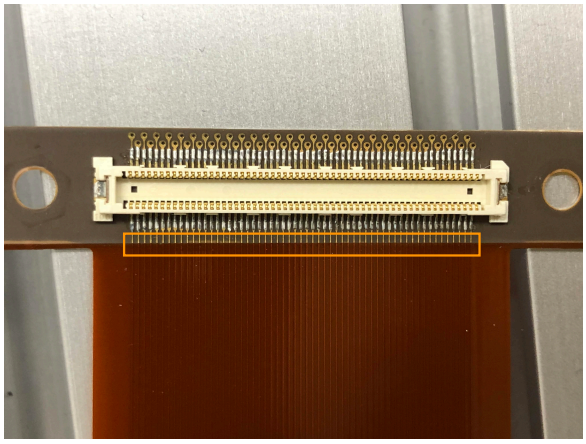

(a)

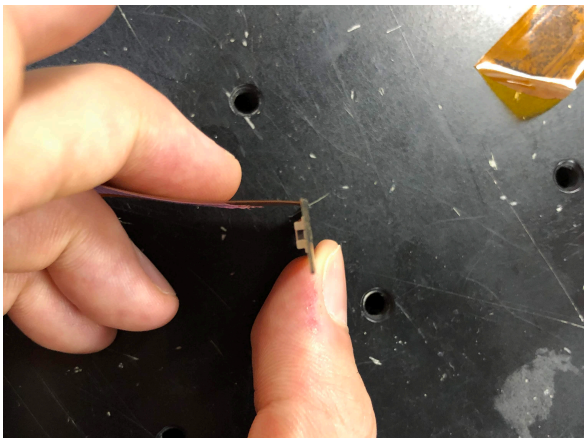

(b)

Figure 3.16: Old design of the connecter part of the FPC. Disconnection occured at the orange are in (a). When the connecter part is bent as shown in (b), the cupper foil is cutted by the coverlay and disconnected.

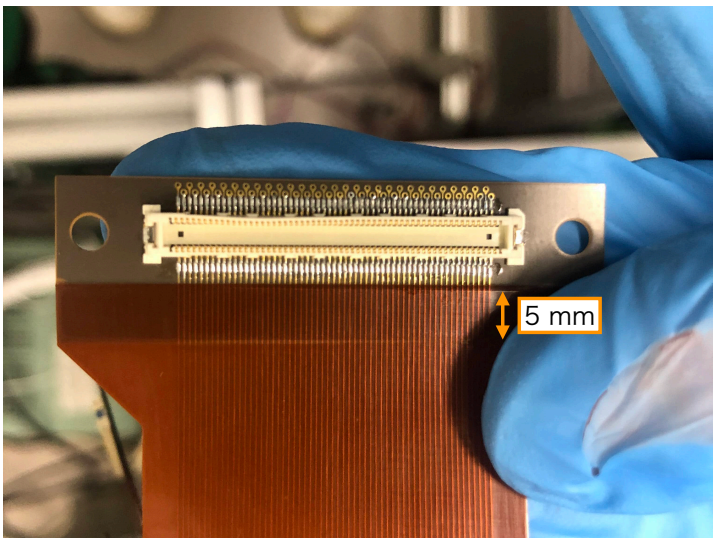

Figure 3.17: New design of the FPC connecter part. In order to avoid the disconnection, the base plate and the coverlay have a 5 mm overlap.

Chapter 4

AxFEB: Front-End-Electronics

4.1 Requirement

AxFEB is a front-end-electronics to read out the signal of MPPCs of ELCC. Since the power supply line of MPPC is the signal output line, power supply to MPPCs is required. And waveform acquisition is also required to reconstruct the event topology. As mentioned in Chap. 2, the fundamental resolution of the AXEL detector is 0.25% FWHM at Q-value. To achieve the target energy resolution of 0.5% FWHM at Q-value, the effect of other factors on the resolution has to be less than 0.43% FWHM. The following factors are considered the main causes of poor resolution.

(1) Fluctuations in the amplification process, such as EL amplification and amplification at MPPC.

(2) Fluctuations in signal magnitude derived from variations of pressure, impurity concentration, etc.

(3) Errors and nonlinearities in sampling and digitally converting MPPC signals.

(4) Noise in circuits.

In order to suppress the effect of (1), the most important point is to obtain uniform gain by tunning the amplification factor of individual MPPCs. To do this, the dark current of each MPPC is used to obtain the 1p.e. gain, and the bias voltage has to be tuned in tens of mV level according to the amplification factor. (1) To measure the EL gain difference between cells and (2) to measure the time variation with sufficient accuracy, xenon characteristic X-ray (about 30 keV) is used. In order to measure with sufficient accuracy from 30 keV to the Q-value of 2.5MeV, a wide dynamic range is required.

Considering that a typical drift velocity is about 0.1 cm/μs and the drift length of 180L prototype is up to 50 cm, a record length is required to be 500 μs.[1] A sampling speed is

[1]Since the maximum drift length was 60 cm when AxFEB is designed, as the record length, 600 μs is adapted.

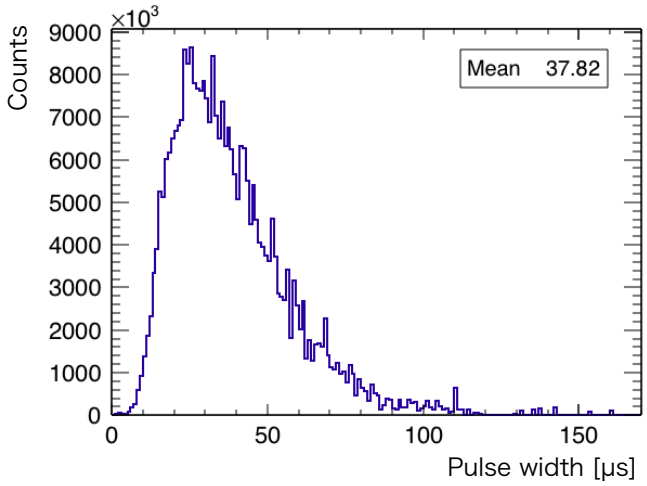

Figure 4.1: Simulation result of the duration time of the EL signal in a MPPC.

required to be at least 5 Mega Sampling/s, which is from a requirement of a nonlinearity correction of MPPC under large intensity light.

For scalability, it is useful if AxFEB can be operated by a single voltage. Also, if the AxFEB can be communicated via Ethernet, it can send data for a PC and slow control.

In order to quantitatively evaluate the dynamic range requirements, we performed simulations. EL photons observed by an MPPC are simulated by generating $0\nu\beta\beta$ decay by Geant4 and considering the drift of electrons and EL yield. Figure 4.1 shows the duration time of EL photons observed by an MPPC. The maximum duration time of the EL light is 150 μs. Fig. 4.2 shows the number of EL photons observed by an MPPC. The distribution of the number of photons is $20 - 20,000$ photons/μs. Therefore, the required dynamic range is $4 - 4,000$ photons/200 ns with 5 MS/s readout. The DC-coupling readout is necessary to read out a significant light intensity of 4000 photons/200 ns and a long waveform of 150 μs without distortion, while ensuring sufficient rate tolerance.

In summary, we developed a front end electronics with the following features.

- Bias voltage supply for MPPC's
  - Up to 65 V
  - Individual bias voltages can be adjusted with 10 mV units.
- Dead time free data acquisition
  - 5 MS/s × 56 ch
  - Amplification factor in analog part: 5 times
  - Dynamic range: $0 - 400$ mV
  - Record length: 3,072 samples (About 600 μs)

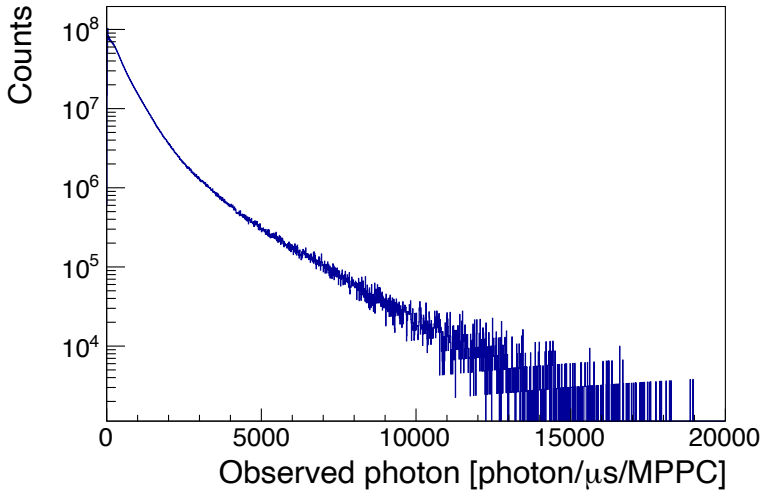

Figure 4.2: Simulation result of the number of photons observed by a MPPC.

- Acquiring dark current
  - 40 MS/s × 7 ch
    - Acquiring 7 channels at the same time
    - Acquiring channels can be changed by a multiplexsa.
  - Amplification factor in analog part: 162 times
  - Dynamic range: $0 - 12$ mV
  - Record length: 8,192 samples
- Data communication and slow control via Gigabit Ethernet

4.2 Design of AxFEB

A brock diagram of AxFEB is shown in Fig. 4.4. AxFEB is driven with DC 5 V.

The gain of MPPC is given as,

$$g \equiv \frac{Q_{1\,\mathrm{p.e.}}}{q_{e^-}} = \frac{C(V_{\mathrm{bias}} - V_{\mathrm{break}})}{q_{e^-}} = \frac{C \cdot V_{\mathrm{over}}}{q_{e^-}}, \tag{4.1}$$

where $Q_{1\,\mathrm{p.e.}}$ is a charge of a 1 photon-equivalent (p.e.) signal, q_{e^-} is an elementary charge, C is a capacitance of a APD in the MPPC, V_{bias} is applied voltage for MPPC, and V_{break} is a voltage at which APD's start the operation of Guiger mode. The V_{over} is called overvoltage, and the gain of MPPC is proportional to it. The overvoltage is very small compared to the breakdown voltage, and breakdown voltage varies for each MPPC. In order to control gains with 1% level precision, the bias voltage has to be controlled with a precision of a few tens of mV. The precision is achieved by supplying a uniform voltage to the cathodes of

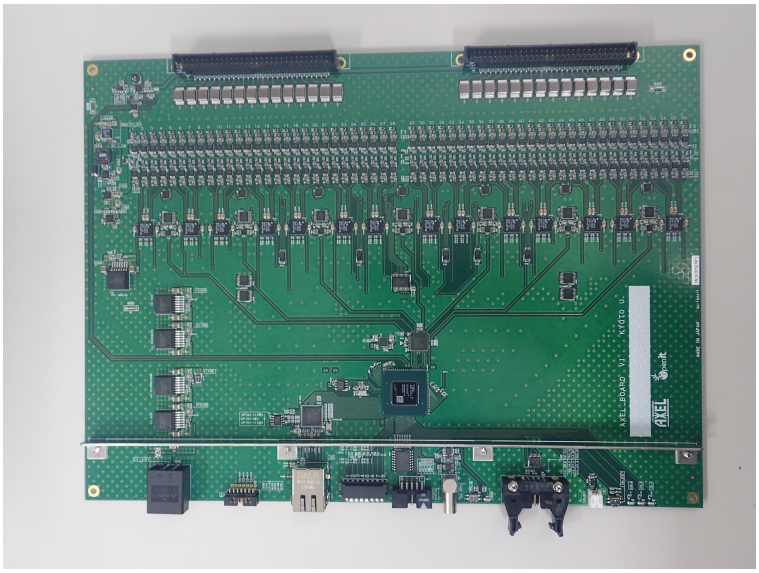

Figure 4.3: AxFEB

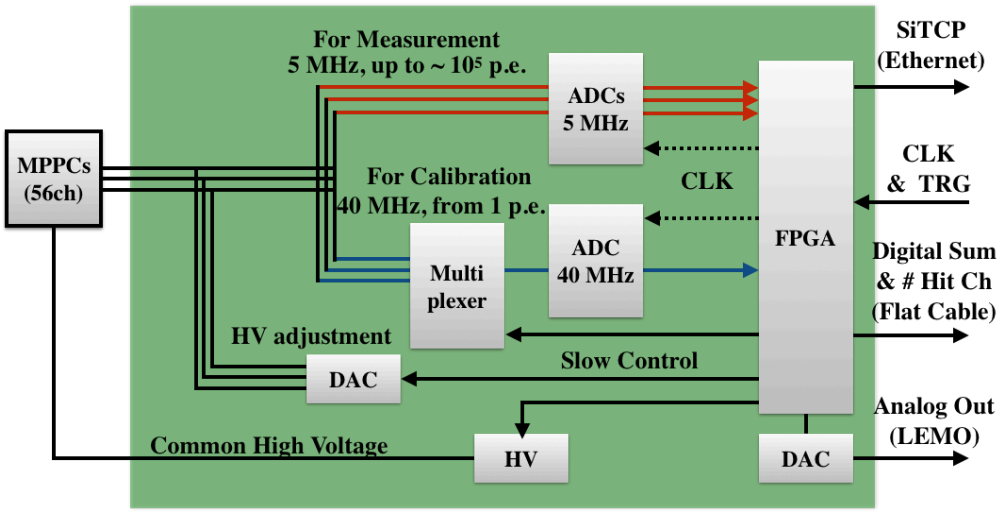

Figure 4.4: Block diagram of the AxFEB.

MPPCs with a DAC and applying an individual voltage to the anodes of MPPCs. The DAC for uniform voltage reaches up to 65 V, and the DAC for the adjustment applies in units of 10 mV. The detail of the adjustment is described in Sec. 4.2.1.

AxFEB has two types of ADC's, one for EL light waveform acquisition and the other for dark pulse waveform acquisition. The ADC for the EL light waveform acquisition is called ADCL, and the ADC for the dark pulse acquisition is called ADCH. There are 56 ADC channels for simultaneous waveform readout of all channels. On the other hand, there are 7 ADCH channels. To each of ADCL channel, 8 MPPC signals are connected via a 8:1 analog multiplexer connected and multiplexes switch reading channels.

The values of 56 channels of ADCL are summed up in each three samples, the sum value is sent to the trigger module. The trigger module further sums up the ADC values sent from all AxFEB and produces the trigger based on the value. Then the trigger signal is sent to AxFEBs and the DAQ PC. When the AxFEB receives a trigger signal from the trigger module, data is sent to the PC. Each AxFEB is assigned an IP address, allowing data communication and slow control with the PC via Ethernet. Overall control, data processing, and communication with the trigger module and the PC are handled by the FPGA on the board.

4.2.1 Analog Section

The diagram of the analog secter of AxFEB is shown in Fig. 4.5. The main task of the analog sector is:

1. Provide the bias voltage to each MPPC.
2. Amplify the MPPC signal to match the dynamic range of the ADCs
3. Shaping the waveform to match the sampling rate of the ADCs

The MPPC signal is shaped and amplified in the first-order filter (Integrating circuit) shown in Fig. 4.5c. The time constant of this filter is 17 ns and the amplification factor is five. Then, the waveform is shaped by the second-order filter (Sallenkey filter) with 400 ns time constant, and input to ADCL. The total amplification factor for ADCL is five. On the other hand, the signal input to ADCH is taken from the first filter, amplified by 16.5 by the inverting amplifier circuit shown in Fig. 4.5e, and further amplified by a factor of 2 by a differential amplifier before being input to ADCH. The total amplification factor for ADCH is 165.

A common voltage is applied to the cathode of MPPC by a BIAS DAC with a low-pass filter attached to each channel. The bias voltage for each channel is finely adjusted by ADJ DAC connected to the anode of the MPPC. In such a configuration, AC-coupling read is usually adapted to avoid the offset of the baseline. However, AC-coupling causes distortion for long pulses. AxFEB uses DC-coupling readout because it is necessary to read pulses of up to 150us duration without distortion while ensuring sufficient rate tolerance. In order to realize this feature, the virtual short-circuit connection of operational amplifiers is utilized.

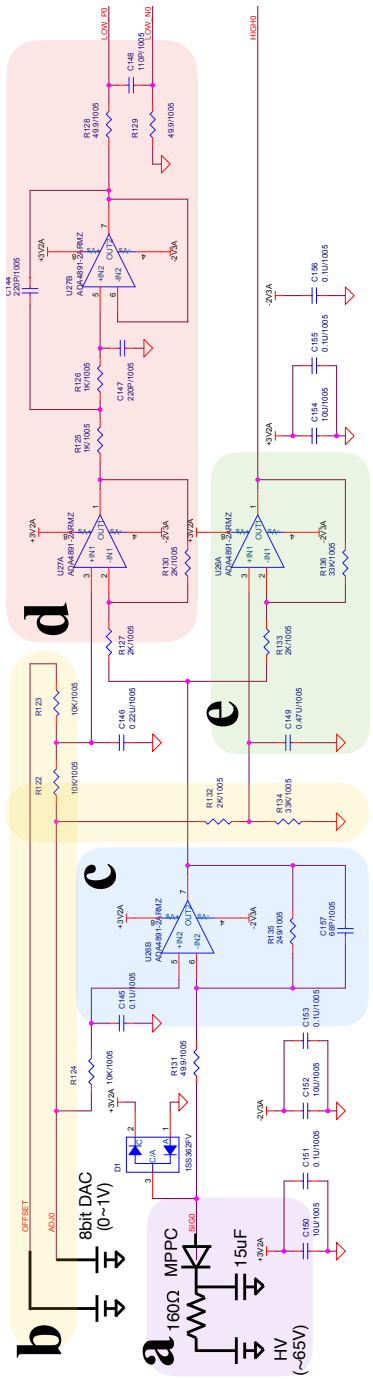

Figure 4.5: Diagram of the analog sector of AxFEB. (a) A common voltage is applied to the cathode of MPPC by a BIAS DAC. (b) The bias voltage is finely adjusted by ADJ DAC. (c) The MPPC signal is sharped and amplified in the first-order filter (Integrating circuit). The time constant of this filter is 17 ns and the amplification factor is five. (d) The waveform is shaped by the second-order filter (Sallenkey filter) with 400 ns time constant, and input to ADCL. (e) the signal input to ADCH is further amplified by 16.5 by the inverting amplifier circuit. The total amplification factor for ADCH is 165.

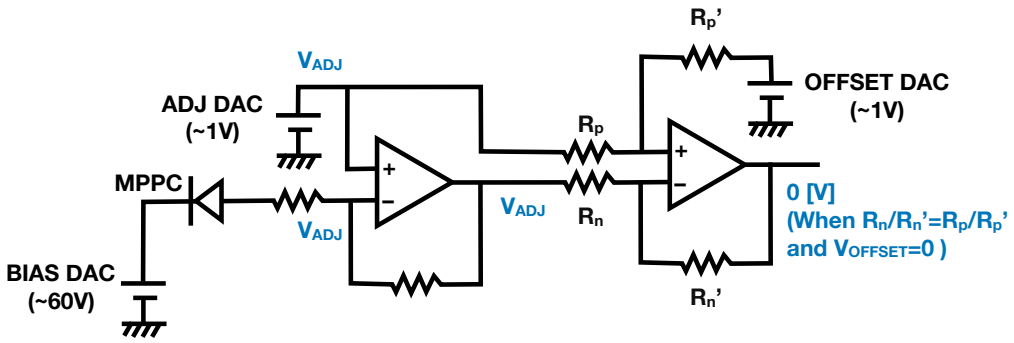

Figure 4.6: Mechanism of the bias voltage adjustment. In order to realize gain adjustment with DC coupling readout, the virtual short of the operational amplifier is applied.

The part where the bias voltage is finely adjusted is shown in Fig. 4.5b. Also, the mechanism of the adjustment is shown in Fig. 4.6. When V_{ADJ} is output from the ADJ DAC, V_{ADJ} is virtually applied to the anode of the MPPC by the virtual short of the first operational amplifier. At the same time, V_{ADJ} is applied via resister, R_{p}, to the op-amplifires that follows the first op-amplifire. Since the output of the first op-amp has an offset of V_{ADJ}, the offset is canceled by the second stage op-amp when the relationship $R_{\mathrm{n}}/R_{\mathrm{n}'} = R_{\mathrm{p}}/R_{\mathrm{p}'}$ is satisfied OFFSET DAC is prepared for further fine tunning.

4.2.2 Digital Section

As the ADC chip for ADCL, Analog Devices Inc. LTC2325CUKG-12 is adapted. Its dynamic range is $2\,\mathrm{V_{pp}}$ and sampling rate is $5\,\mathrm{MS/s}$. Considering the amplification factor in the analog sector, the maximum input pulse height is $400\,\mathrm{mV}$. With the normal gain of 2.6×10^6 of the ELCC MPPC, the allowable photon number is $4,000\,\mathrm{photon}/200\,\mathrm{ns}$.

The ADC chip for ADCH is Analog Devices Inc. AD9637. The dynamic range is $2\,\mathrm{V_{pp}}$, and the sampling rate is $40\,\mathrm{MS/s}$. This ADC chip has 8 ADCs, and 7 channels are used. Considering the amplification factor in the analog circuit, the maximum input pulse height is $12\,\mathrm{mV}$.

As the FPGA, Xilinx Inc., XC7A200T-1FBG484C is used. Considering that the data size of an event is about $2\,\mathrm{Mbit}$, 200T series whose memory size is $13\,\mathrm{Mbit}$ is used. The main function of FPGA is as follows,

- Slow control of DACs (BIAS DAC, ADJ DAC, OFFSET DAC).
- Distribution of clocks to the ADC chip.
- Sum up ADC values from ADCLs and send it to the trigger module
- Receives trigger or veto signals from the trigger module and sends data to the data-taking PC.
- Control of the multiplexer for ADCH

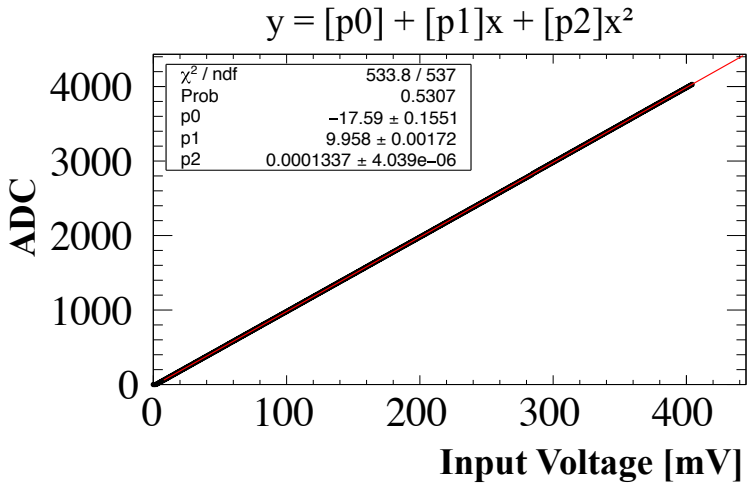

Figure 4.7: Relationship between the input voltage and the ADCL ADC value. By fitting with a quadratic function, the linearity of ADCL is evaluated.

- Store the ADC values by forming ring buffer memories.

An LVDS signal of 160 MHz is used for communication between the AxFEB and the trigger module. AxFEB communicates with the PC via gigabit Ethernet. The acquired data is transferred by TCP protocol, and UDP protocol is used for the slow control. SiTCP is used for Ethernet communication in FPGA.

4.3 Performance Evaluation

4.3.1 Performance of ADCL

The linearly of ADCL was confirmed by inputting a constant voltage to ADCL in 1 mV increments. Fig. 4.7 shows the relationship between the input voltage and the ADC value. It was fitted by a quadratic function. The quadratic component is about 10^{-5} compared to the linear component. It was confirmed that the linearity is sufficient.

4.3.2 Performance of ADCH

Fig. 4.8 shows the waveform of MPPC dark pulses taken by ADCH. It is confirmed that the pedestal and dark pulses are discriminated clearly. Also, it is confirmed that the read out channels can be changed by multiplexes.

4.3.3 Gain Adjustment

We confirmed the change of MPPC gain by changing the applied voltages for MPPC. The result is shown in Fig. 4.9. The blue circle indicates the gain, where BIAS DAC is changed

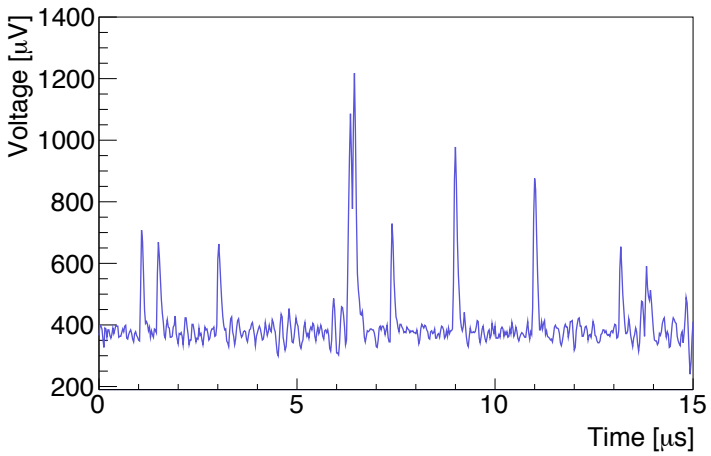

Figure 4.8: Waveform of MPPC dark pulses taken by ADCH. The pedestal and the dark pulses are well discriminated.

from 54.9 V to 55.3 V while fixing V_{ADJ} at 0 V. The red circle indicates the gain, where V_{ADJ} is changed with the fixing output of BIAS DAC at 55.3 V. It is confirmed that the gain of MPPC can be controlled by $V_{\mathrm{BIAS}} - V_{\mathrm{ADJ}}$. The gain changes about 2.5% with bias voltage change of 0.1 V. Since DAC can be changed with 0.01 V step, the gain of the MPPC can be controlled with 0.25% precision.

Fig. 4.10 shows a comparison of the gain distribution before and after the gain adjustment. It is confirmed that the gains, which are uneven when a common bias voltage is applied, are controlled to one value after fine adjustment.

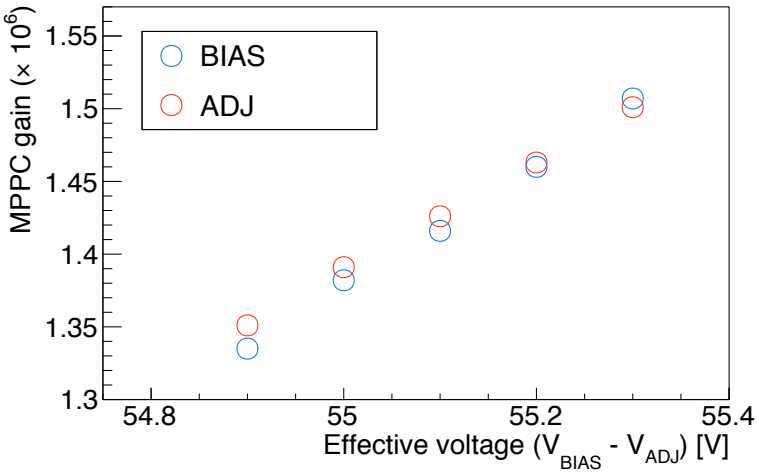

Figure 4.9: Relationship between the effective applied voltage for MPPC and the gain of MPPC. The blue circle indicates the gain, where BIAS DAC is changed from 54.9 V to 55.3 V while fixing V_{ADJ} at 0 V. The red circle indicates the gain, where V_{ADJ} is changed with the fixing output of BIAS DAC at 55.3 V. It is confirmed that the gain of MPPC can be controlled by $V_{\mathrm{BIAS}} - V_{\mathrm{ADJ}}$.

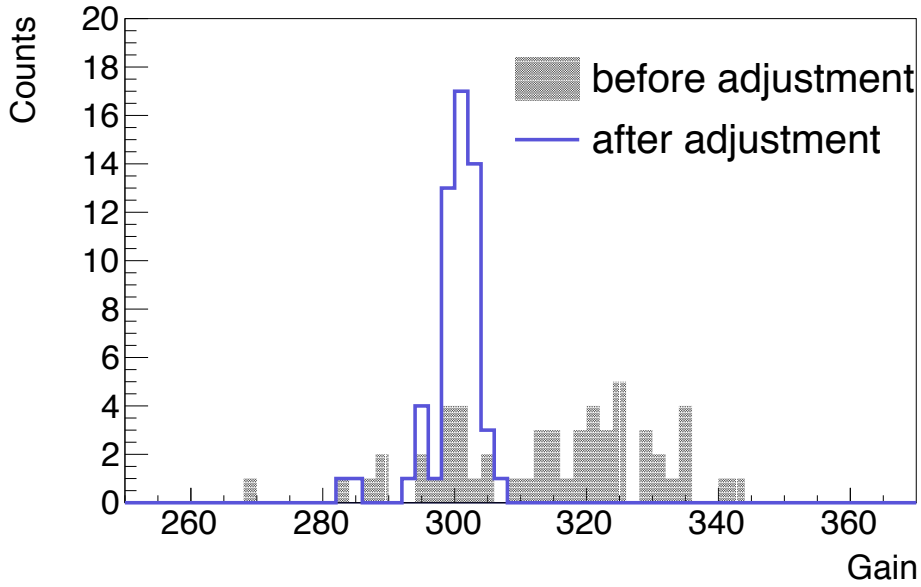

Figure 4.10: Gain distribution for 56 MPPCs. It is confirmed that the gain, which is uneven when a common bias voltage is applied, is uniform after fine adjustment.

Chapter 5

Data Acquisition System

The data acquisition system of the 180L detector handles two types of read-out modules. One is AxFEB to read out the ELCC signal, and the other is a general-purpose digitizer to read out the PMT signal. A schematic diagram of the data acquisition system is shown in Fig. 5.1.

5.1 Data Acquisition for ELCCs

Waveforms of MPPCs are taken by ADCLs of the AxFEB. As a trigger board, Hadron Universal Logic module (HUL) is used.

5.1.1 HUL

HUL is a general-purpose IO logic module. For the 180L detector data taking, HUL is used combned with an extended card, HUL Mezzanine differential signal transmitter LVDS (Mezzanine DTL). HUL supports up to 64 channels of signal input. Up to two Mezzanine DTLs can be installed in the HUL, each having 32 channels of LVDS output. HUL is equipped with Xilinx Kintex7 and we developed firmware for the 180L detector. HUL supports GbE and can send data via TCP communication and slow control via UDP communication. Communication between HUL and AxFEB is done by 160 MHz LVDS signals.

The LVDS signal sent from AxFEB to HUL is as follows.

- data: 1/2 of the sum of 3 samples of ADC values of fiducial channels, 1/2 of the sum of 3 samples of ADC values of veto channels, hit_mask (not used)
- enable_reading: 1 pulse is sent at every break in the data (96 bits) as a separator.

The LVDS signal sent from HUL to AxFEB is as follows.

- clock: 160 MHz clock signal. AxFEB is driven by this clock.
- trig: tigger signal, veto signal, etc. are sent in synchronization with the clock.

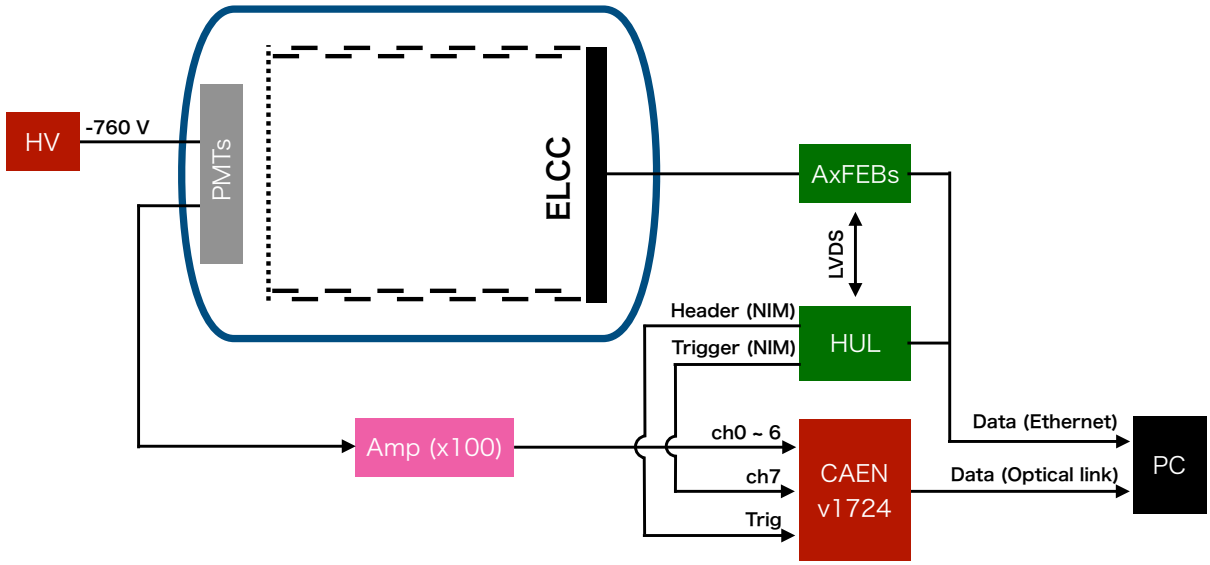

Figure 5.1: Schematic diagram of the data acquisition system of the 180L detector.

HUL further sums up the ADC values for the fiducial and veto channels received from each AxFEB. Based on the summed ADC values, HUL sends the trigger or veto signal to the AxFEB accordingly.

5.1.2 Details of the Data Acquisition

Fig. 5.2 shows the data flow of ADCL data in AxFEB.

(1) Serial data from ADCL is converted to paralel data in the Deserializer (DSR) module and it is sent to the Ring Buffer (PBF) module and the DigitalSum (DSM) module.

(2) In DSM, ADC counts of each clock are summed up for fiducial channels and veto channels. They are averaged by 3 samples and sent to HUL.

(3) The data are continuously stored in the PBF. When a trigger signal is received from HUL, the data begins to be sent to the Event Buffer starting from the specified depth prior to the trigger timing. (Four event buffers are equipped in the AxFEB. In the figure, only EBF1 and EBF2 are shown.)

(4) Send the data for the fixed length. If a veto signal is received from HUL during the process, the data are discarded.

(5) When a header signal (signal sent from HUL when veto is not issued) is received from HUL, data is sent to the TCP Sender (SND) module.

(6) Data in SND are divided into 1 Byte each and sent to PC via SiTCP.

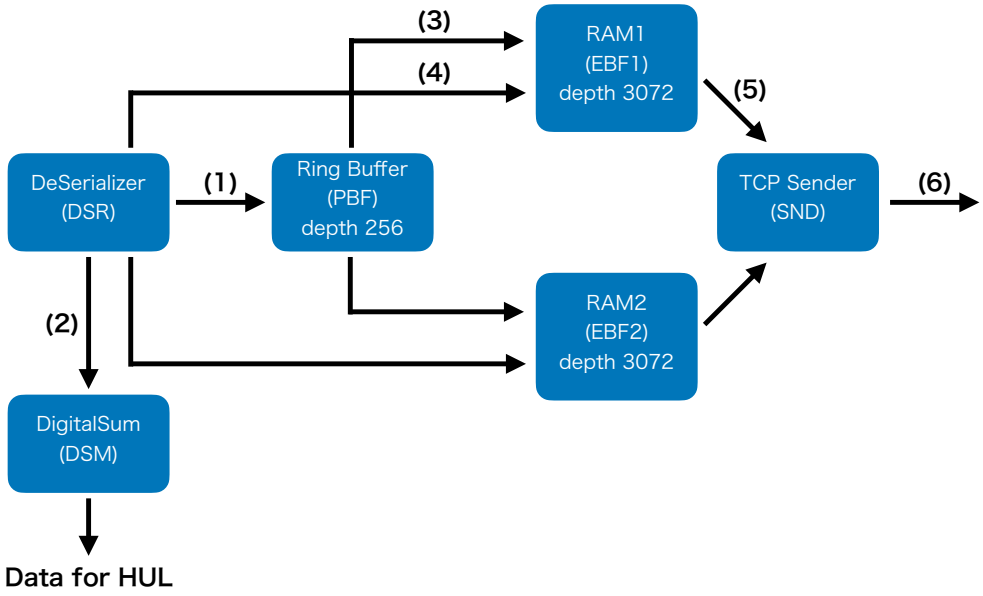

Figure 5.2: ADCL data flow in AxFEB.

The DAQ system has two levels of thresholds, one for data acquisition and one for calibration. A trigger for the data acquisition is called fid_trig, and a trigger for calibration is called whole_trig. The whole_trig is set to acquire the characteristic x-ray of xenon around 30 keV. Since low-energy events have a higher event rate than high-energy events, the whole_trig event is issued once per a certain number. Dark pulses of MPPCs are acquired periodically.

5.2 Data Acquisition for PMTs

A supply voltage of the PMT is -760 V. The PMT signals are amplified by 100 by an amplifier and readout by CAEN v1724. The header signal issued by HUL is used as the trigger for v1724. Also, the trigger signal issued by the HUL is input to ch7 of v1724. The trigger signal is synchronized with the timing of the trigger timing of the AxFEB, and by using this signal, the timing of the data acquired by AxFEB and v1724 is synchronized. Data acquired by v1724 is sent to a PC via an optical link.

5.3 Event Matching between ELCCs and PMTs Data

If an event is missed in the v1724, for example, by PC busy status, a gap is made in the event ID between the AxFEB and the v1724. To reconstruct events even in such a case, the duration time between events is calculated from each timestamp by PCs, and the events are matched when the time difference between each duration time is within 100 μs.

Chapter 6

Calibration of MPPC

6.1 One-photon Equivalent Gain

For calibration and analysis, ADC counts of AxFEBs have to be converted to the number of photons detected by the MPPC of that channel. In order to do so, it is necessary to determine that the one-photon equivalent (1 p.e.) gain of the MPPC is a unit of the ADC count. We use dark pulses of the MPPCs, whose data are periodically acquired during the data-taking by AxFEB's ADCH. Typical waveforms acquired are shown in Fig. 6.1. Dark pulses are clearly identified by the pulse heights.

We use pulse height to select a region to integrate and calculate the ADC count for a dark pulse. The pulse height threshold is set at 40 counts.

To subtract the baseline offset, the baseline is calculated by making a distribution of the ADC count and taking the peak position.

The pulse threshold is set at 40 counts, and the width of the integration is 25 clocks. The distribution of the integral value is shown in Fig. 6.2. The 1 p.e. gain is obtained as a difference of the peak positions of those with and without dark pulses. This 1 p.e. gain is converted to that in a unit of ADCL considering the ratio of the gains of the analog circuit of AxFEB and the sampling speeds between ADCH and ADCL.

The 1 p.e. gain determined for 56×12 channels are shown in Fig. 6.3. The mean of the distribution is 0.9577 in a unit of ADCL count corresponding to 2.33×10^6 multiplication factor of MPPC. The relative standard deviation of the gain distribution is 2.41%. The operating voltage was adjusted to align gains within 1%. However, optimum operation voltage is larger than the dynamic range of the gain adjustment of AxFEB for some channels.

6.2 Nonlinearity

6.2.1 Overview

MPPCs have a significant nonlinearity under high light intensity. This is because when two or more photons are incident to one pixel in a short period, the output charge from that pixel

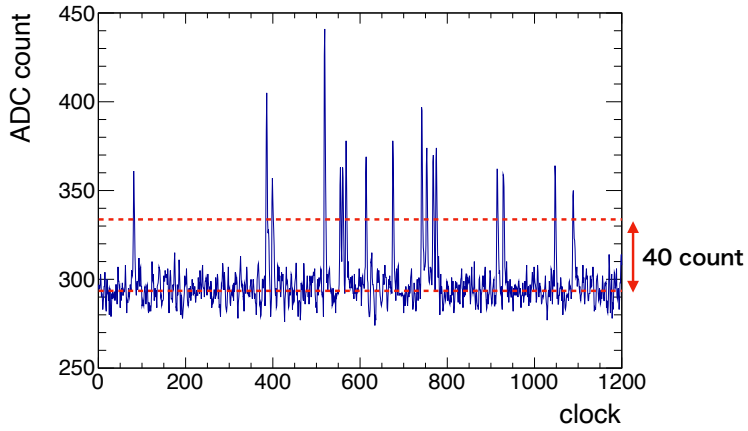

Figure 6.1: Typical waveform of MPPC dark pulses obtained by AxFEB ADCH. One clock corresponds to 25 ns.

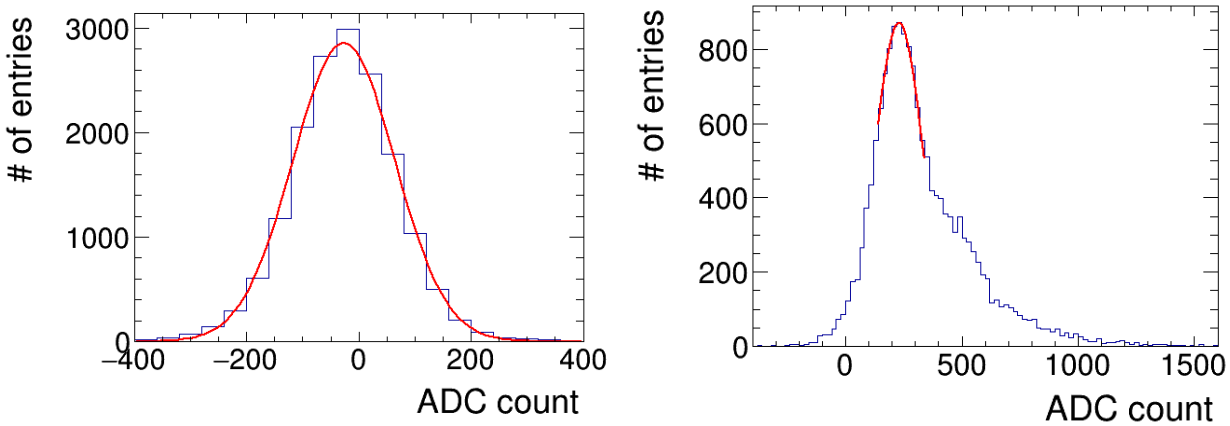

(a) Pedestal-only distribution

(b) Distribution with the dark pulses

Figure 6.2: Distribution of 25-samples integration. If the waveform does not exceed the pulse threshold, the integration value is filled into (a), otherwise the integration value is filled into (b). The 1 p.e. gain is obtained by the difference of peak positions.

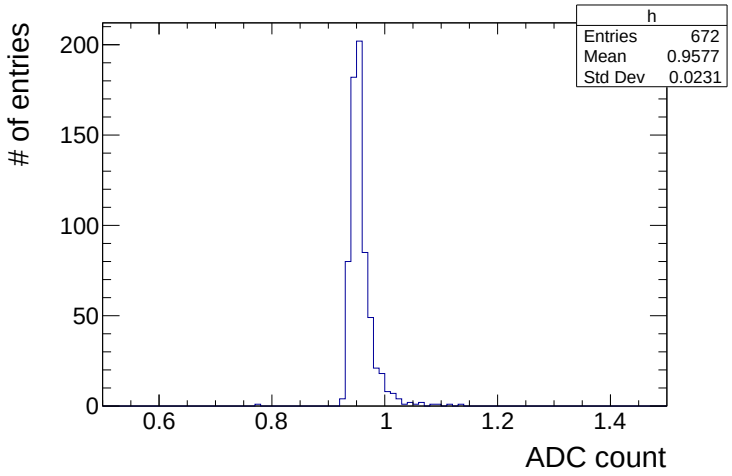

Figure 6.3: Distribution of the 1 p.e. gain in unit of ADCL. The relative standard deviation of the distribution is 2.41%. after the bias voltage were adjusted.

is limited because the voltage on that pixel is quenched. In order to achieve high energy resolution, it is required to correct this nonlinearity.

The nonlinearity can be modeled as follows[20].

$$N_{\text{obs}} = \frac{N_{\text{true}}}{1 + \tau \dfrac{N_{\text{true}}}{\Delta t \cdot N_{\text{pix}}}}, \tag{6.1}$$

where N_{pix} is the number of pixels of a MPPC, N_{true} is the number of photons incident to the MPPC in a certain time Δt, and N_{obs} is the number of photons calculated from the output of the MPPC in Δt. The Δt should be shorter than the time scale of the detector response. The nonlinearity is characterized by τ called recovery time, which is a time required for a pixel to recover from the quenched state. Typically, the range of the τ is $70-80$ ns for our MPPCs. An example of the responce of the model is shown in Fig. 6.4, where $\tau = 75$ ns, $\Delta t = 1,000$ ns, $N_{\text{pix}} = 3,600$ are assumed. The effect of the nonlinearity on energy reconstruction was evaluated by a simulation, and the result is shown in Fig. 6.5. From this, it is concluded that the recovery time has to be measured within 2 ns accuracy[1].

The recovery times of the MPPCs used in the 180L detector were determined by measuring the responses to high light intensity by a LED. In order to monitor the number of incident photons to the target MPPC, a reference MPPC with light intensity reduced by an ND filter is used. The transmittance of the ND filter is 5%. By fitting the relationship between the number of photons observed by the target MPPC, N_{obs}, and the number of photons observed

[1]In this simulation, as the cell pitch, 13 mm is assumed. Since the current cell pitch is 10 mm, the number of instantaneous photons incident on the MPPC is smaller than the simulation, and an effect of nonlinearity would be small. Therefore, 2 ns would be stricter than the actual requirement.

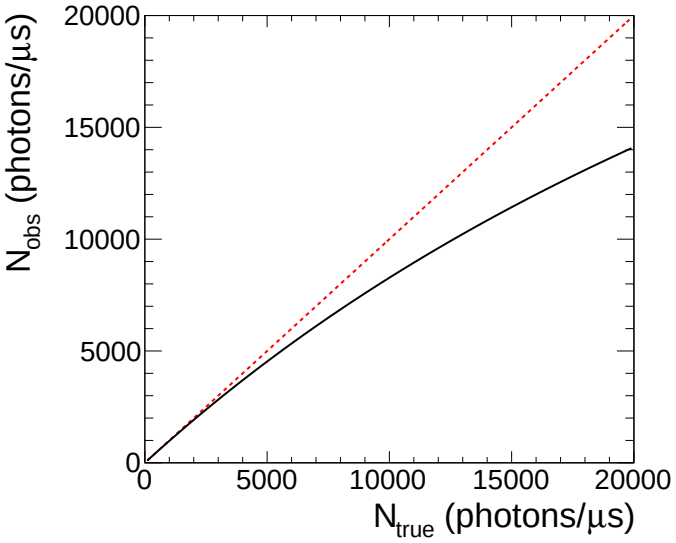

Figure 6.4: Example of the MPPC responce under high light intensity. The black line represents the MPPC responce, where $\tau = 75\,\mathrm{ns}$, $\Delta t = 1000\,\mathrm{ns}$, $N_{\mathrm{pix}} = 3600$ are assumed.

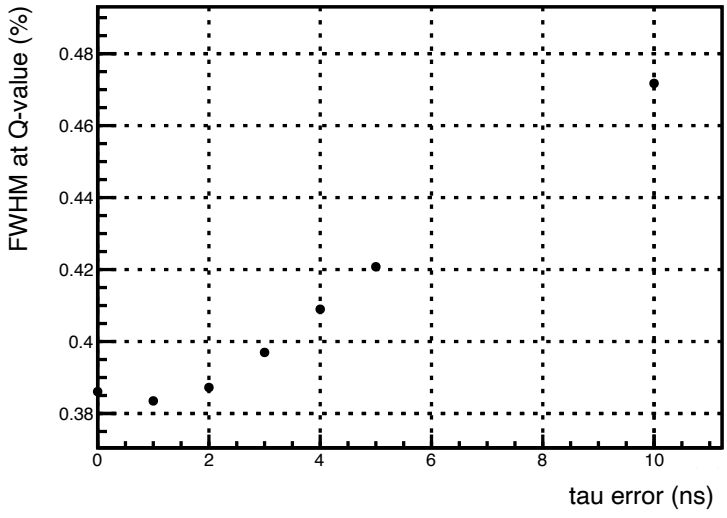

Figure 6.5: Relationship between the resovery time error and the energy resolution.

by the reference MPPC, N_{ref}, with a function of a and b,

$$N_{\mathrm{obs}} = \frac{aN_{\mathrm{ref}}}{1 + bN_{\mathrm{ref}}}, \tag{6.2}$$

the recovery time is obtained as follows,

$$\tau = \frac{b}{a-1}\Delta t \cdot N_{\mathrm{pix}}, \tag{6.3}$$

where it is assumed that the difference in the recovery time between the target MPPC and the reference MPPC is not large.

The measurement error of the recovery time mostly originates from the measurement error of the 1 p.e. gain. In order to obtain the recovery time within 2 ns accuracy, the 1 p.e. gain has to be measured within the 1% accuracy.

6.2.2 Measurement Setup

The schematic view of the calibration system for the recovery time measurement is shown in Fig. 6.6. Two LEDs are mounted on the base plate to fix the PMTs as shown in Fig 6.7. A blue light LED L-9294QBC-D (Kingbright Electronic Co, Ltd) is used. In order to operate LED's stably, a 150 Ω register is connected to each LED in series. A 0.13 mm-thick PTFE sheet is mounted in front of each LED to diffuse light.

The setup around the reference MPPC and it's position are shown in Fig. 6.8. A ND filter is installed in front of the reference MPPC.

LEDs are driven by a function generator GFG-3015 (Good Will Instrument Co., Ltd.). It has a serial interface and can be controlled by a PC[2]. GFG-3015 outputs a TTL signal in sync with the LED drive pulse. The TTL signal is converted to a NIM logic signal, and the pulse width is adjusted to 200 ns with a discriminator module. Then it is input as the external trigger signal to HUL. HUL outputs trigger signals to AxFEBs, and data are taken. The depth of the waveform is set to 256 samples, and the pretrigger width is set to 128 samples.

6.2.3 Result

In the calibration run, the rectangle pulse of 1 μs width is applied to LEDs. The pulse rate is set to 50 Hz considering the AxFEB's capacity. The pulse height is changed from 2.2 V to 5.5 V with 0.02 V step.

The output of the MPPC is obtained by integrating 20 samples around the peak after subtracting the baseline. It is then converted to the number of photons by dividing by the 1 p.e. gain of the MPPC. The 1 p.e. gain error is less than 1% and satisfies the requirement.

The obtained relationship between the number of photons detected by the target MPPC and the reference MPPC is shown in Fig 6.9a, where it is fitted by Eq. 6.2 (red line). The fit

[2]The serial interface on GFG-3015 is RS-232C; since there is no RS-232C interface on the PC, we used a conversion connector between RS-232C and USB.

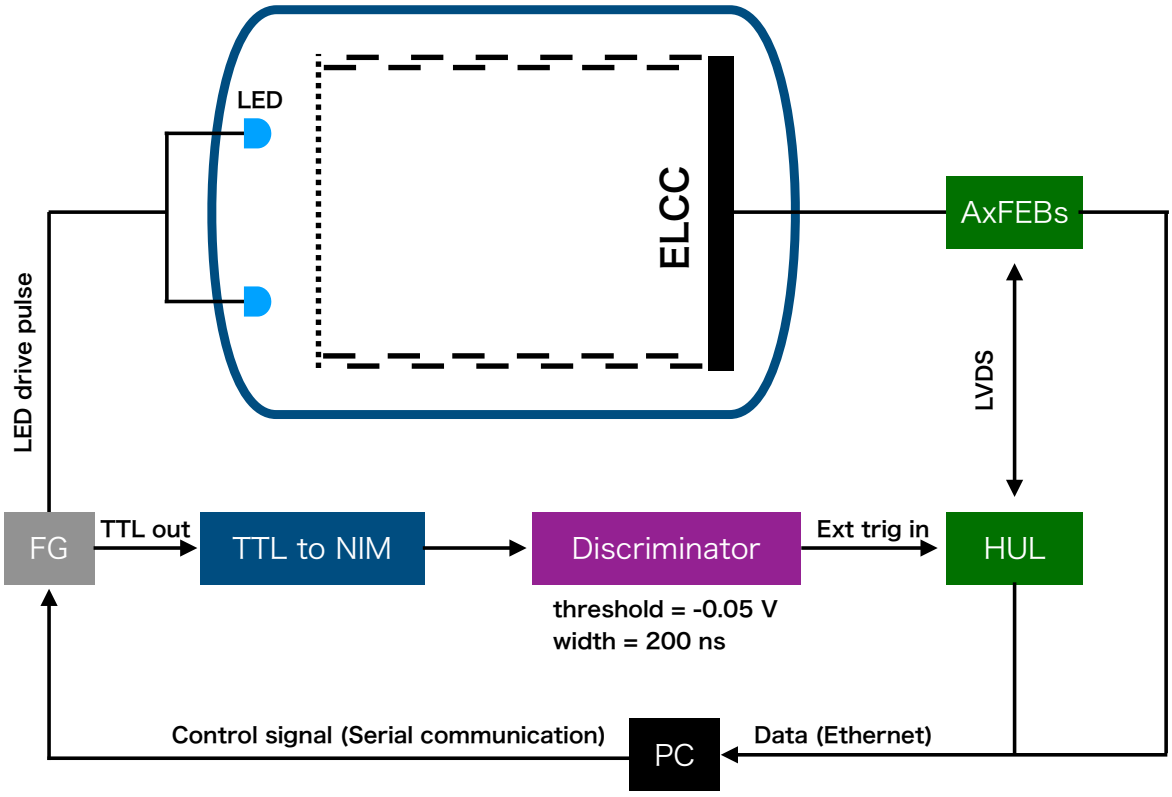

Figure 6.6: Setup of the recovery time measurement. LED installed in the chamber is driven by a function generator (FG). FG output the TTL signal in sync with the LED drive pulse. It is used as an external trigger signal for the DAQ system.

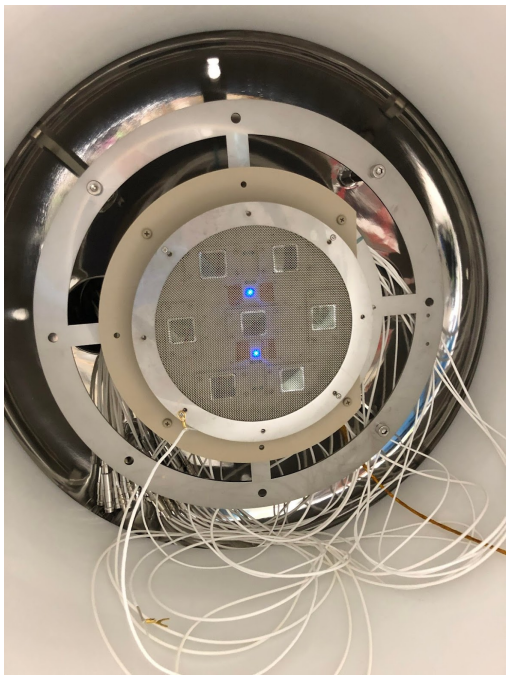

Figure 6.7: LEDs installed in the 180L detector. The LED light is diffused by 0.13 mm-thick PTFE sheets mounted in flont of the LEDs.

residual divided by the fit function is shown in Fig. 6.9b. The residual is evenly distributed around 1, which confirms that the MPPC responce is well reproduced by the fittinng function Eq. 6.2.

The recovery times for all channels are shown in Fig 6.10a, and the errors are shown in Fig. 6.10b. The error of the obtained recovery time is less than 2 ns, which confirms that the requirement for the accuracy of the recovery time is satisfied. This recovery time is used in section 8.3.2 to correct the nonlinear response of the MPPCs.

6.2.4 Effect of the GND mesh

In the recovery time measurement, LED light is irradiated through the ELCC GND mesh to the MPPCs. Because a shadow is created on MPPCs by the mesh, the effective recovery time could be changed since the adequate number of the pixel on the MPPC (N_{pix}) is decreased by the shadow. On the other hand, since the EL light produced in ELCC incidents from a random direction, the shadow might be blurred, and the effect by the mesh could be small. Measurement was conducted to evaluate the Effect of the GND mesh using an MPPC for visible light (S13360-4870). A LED was set either at 150 mm far from the MPPC or closely in front of the surface from the MPPC. The latter emulate the ELCC condition.

The result is shown in Fig. 6.11. With the mesh, the recovery time tends to be larger, about 5 ns. On the other hand, in the case of the measurement emulating EL light, obtained recovery time similar to that without the mesh. It is confirmed that the MPPC response is

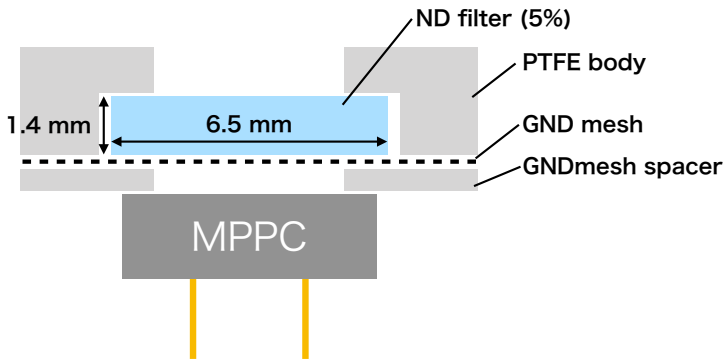

(a)

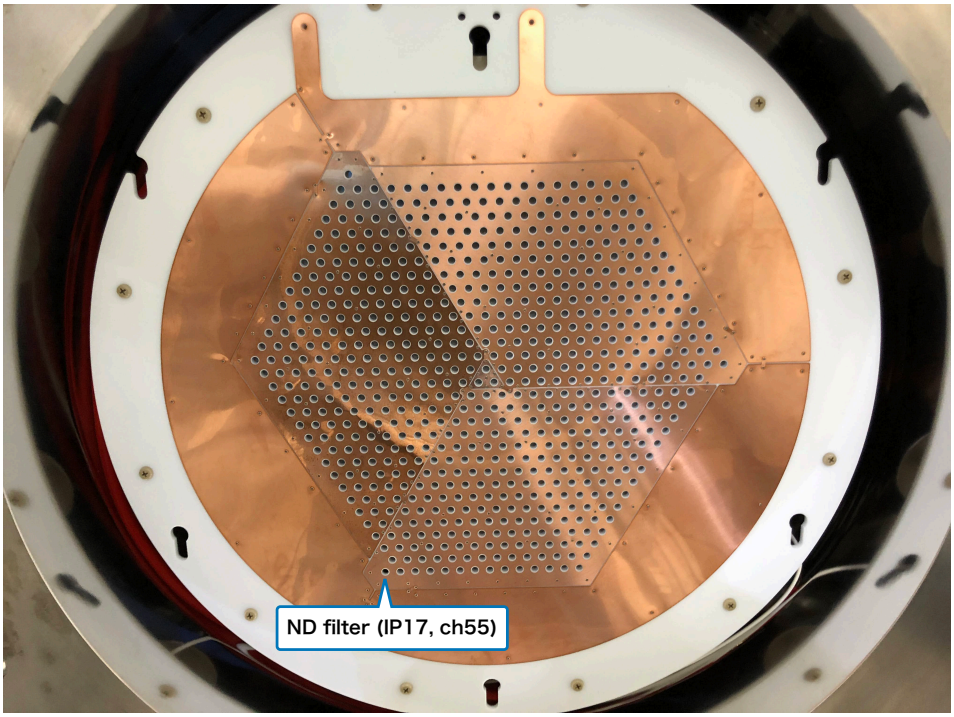

(b)

Figure 6.8: (a)A ND filter is installed in front of the reference MPPC. (b) Position of the reference MPPC (ELCC-3 and ch 55).

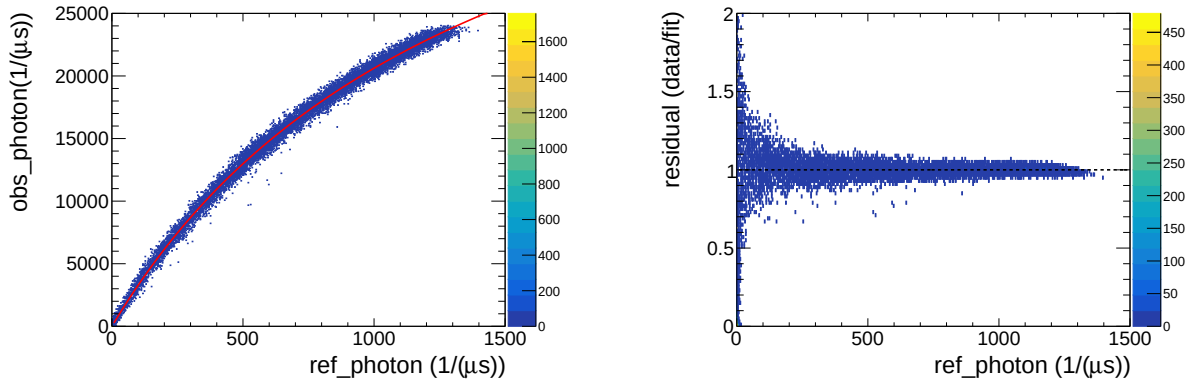

(a) (b)

Figure 6.9: Example of a MPPC output vs. reference (a) The MPPC responce is fitted by Eq. 6.2. The fit result is shown as the red line. (b) Relative fit residual.

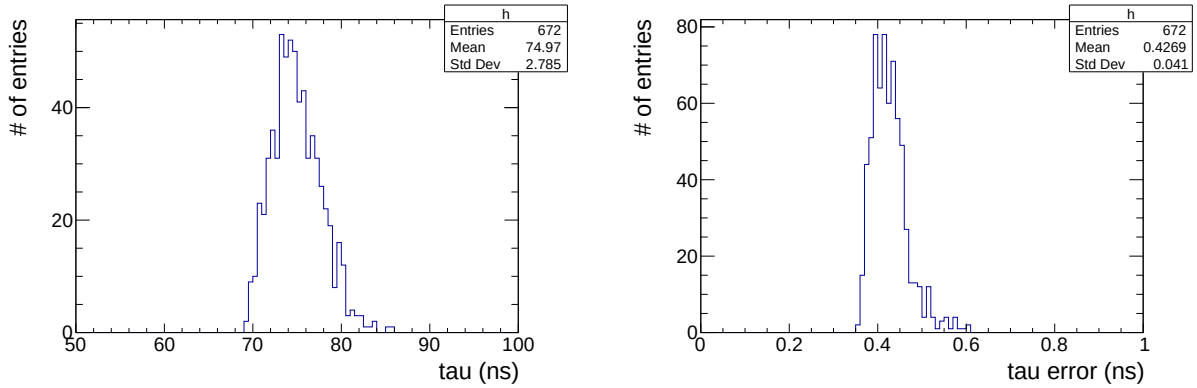

(a) (b)

Figure 6.10: Measured recovery times (a) and their errors (b) for the 672 MPPC's used for the 180L detector. The requirement for the recovery time accuracy is less than 2 ns, and is satisfied.

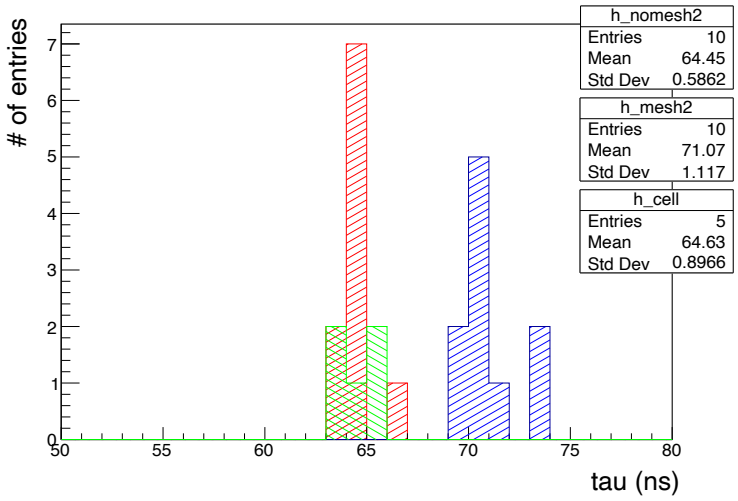

Figure 6.11: Effect of the mesh in front of MPPC. Red and blue histograms show the recovery times measured without and with the mesh, respectively. A LED was set at 150 mm far from the MPPC in these measurements. The green histogram is the result when the LED is set just in front of MPPCs to emulate the ELCC condition. Note that these measurements were done with MPPC S13360-4870, which is not the same type as those used for the 180L detector but has the same area and then a number of pixels.

affected by the mesh in terms of the recovery time. For the 180L detector, since two LED's are used, and the distance between the mesh and MPPC is increased by a 0.5 mm thick PTFE sheet (GNDmesh spacer) added in the ELCC, blurring the shadow, the effect of the mesh would be smaller than the 5 ns. This is further discussed in Section 9.2.

Chapter 7

Operation of 180L detector

7.1 Evacuation and Introduction of Xenon Gas

The chamber was evacuated for 10 days from October 12, 2021 to October 22, 2021 by a sctoll pomp and a turbo molecular pomp. The vacuum level reached 1.70×10^{-2} Pa and the leak rate was 2.33×10^{-4} Pa m^3/s. Then, xenon gas was introduced into the 180L detector up to 8 bar.

7.2 Veto Channel Configuration

In order to define the fiducial volume, veto channels are set as shown in Fig. 7.1. The MPPC on ch46 of IP21 was found to be faulty. This channel and surrounding channels are designated as veto channels. MPPCs on ch19 and ch22 of IP21 had high hit rate because of dhischarge. These channels are also designated as veto channels.

7.3 Operation of the ELCC module

We conducted a voltage application test on the ELCC and succeeded in stable operation for more than 48 hours with the target electric field of 3 kV/cm/bar applied at 7.6 bar (Fig. 7.2).

7.4 Run Summary

In the physics measurement, we were not able to apply the target electric field of 3 kV/cm/bar on the ELCC because discharge happened at above 2.5 kV/cm/bar. Therefore, the EL and drift electric fields were set to 2.25 kV/cm/bar and 75 V/cm/bar, respectively, as stable voltages that can be applied while maintaining the relationship between $E_{\mathrm{EL}} = 3$ kV/cm/bar and $E_{\mathrm{drift}} = 100$ V/cm/bar. Later the chamber was opened, and the corresponding ELCC module was investigated. It was found that the overhang of the mesh was warped up to the anode side as shown in Fig. 7.3. After eliminating the mesh overhang, a voltage application

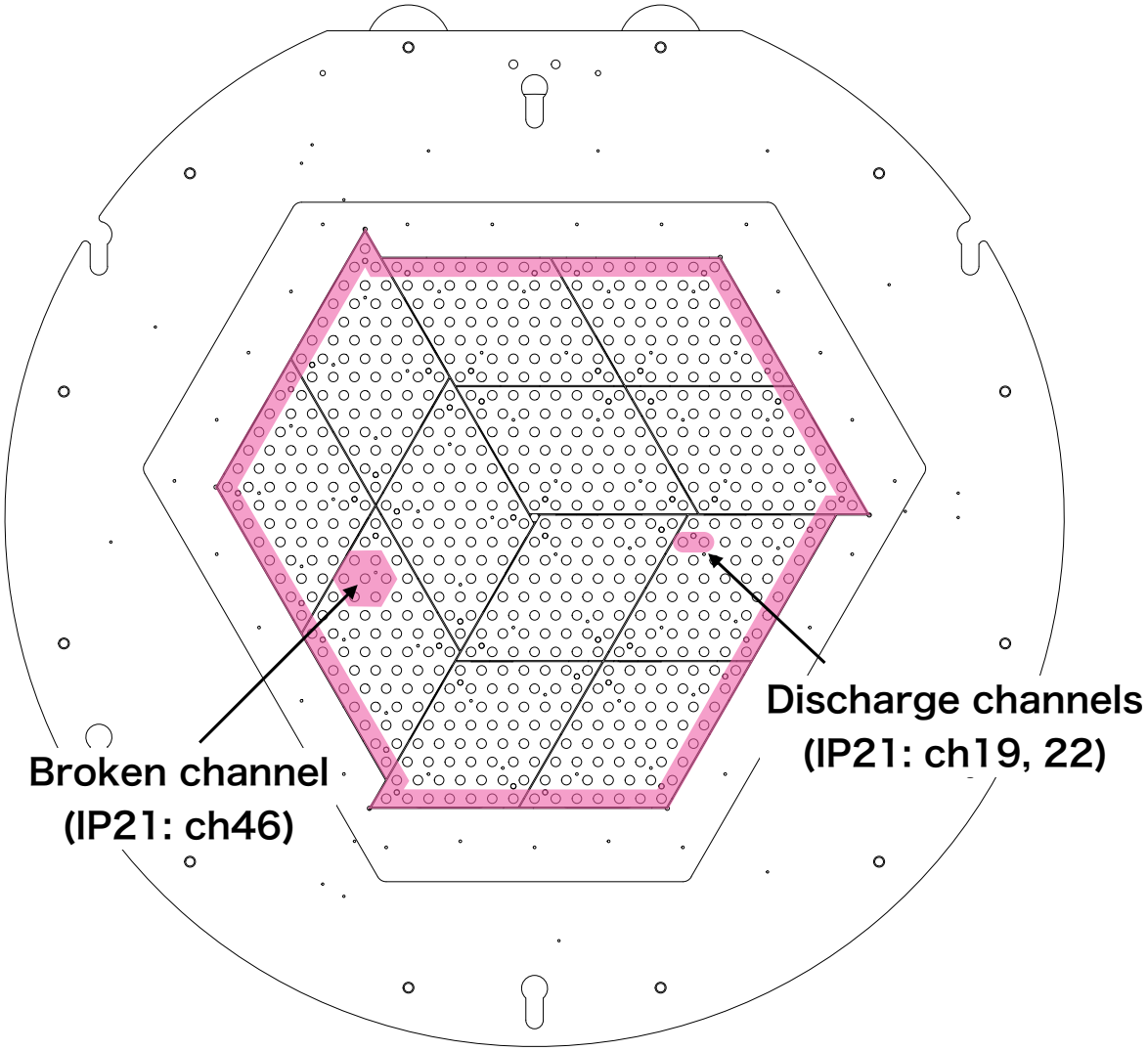

Figure 7.1: Veto channels are shown as the pink area. The MPPC on ch46 of IP21 was out of order. This channel and surrounding channels are designated as veto channels. If veto channels is included in the hit channels, the event is discarded. MPPCs on ch19 and ch22 of IP21 was high rate because of discharge. These channels are also designated as veto channels.

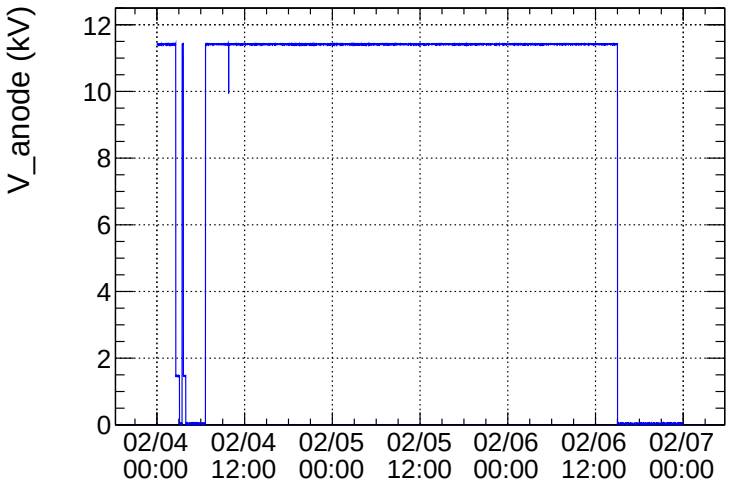

Figure 7.2: High voltage application test on the ELCC modules with 3 kV/cm/bar at 7.6 bar. A stable operation is succeeded more than 48 hours.

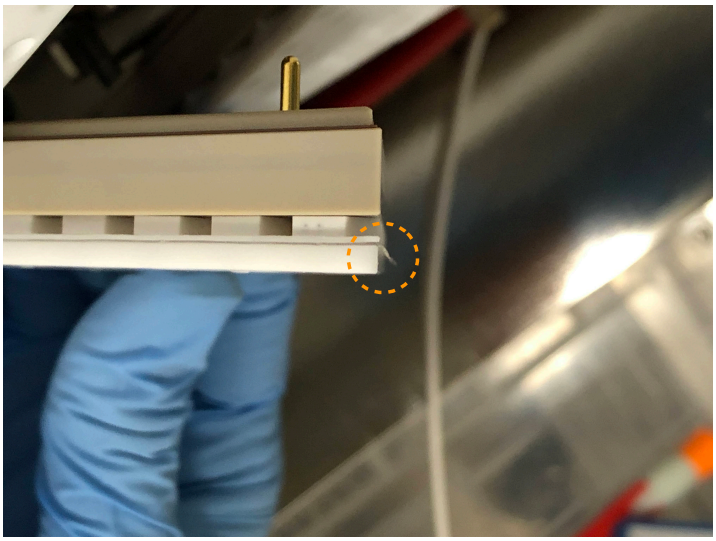

Figure 7.3: Overhang of the mesh was warped up to the anode side.

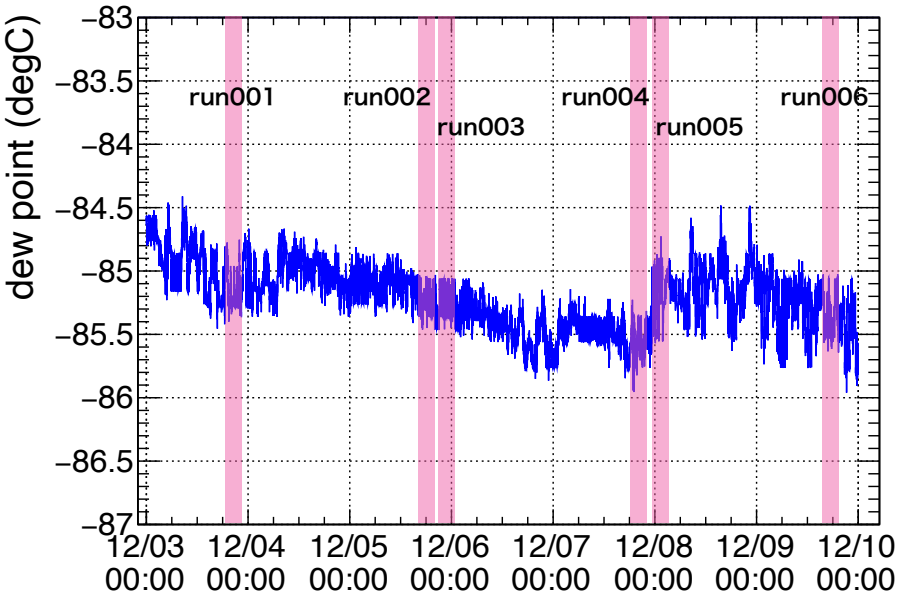

Figure 7.4: Dew point trend.

test was conducted, and as shown in Fig. 7.2, stable operation for more than 48 hours was successfully achieved.

Measurements are conducted in 6 runs, each of which has 200,000 events. The trigger thresholds were tuned as follows. The whole_trig was set so that the K_α can be taken. The fid_trig was set so that some peaks (from 800 keV to 1,800 keV) can be taken. The downsampling ratio for whole_trig was tuned so that the number of events taken by whole_trig is roughly same as that by fid_trig. The xenon gas was circulated through the molecular sieve and getter filter during the measurement to keep the purity. The gas purity was monitored by the dew point meter. The trend of the dew point during the measurement is shown in Fig. 7.4. The dew point was about -85°C, which corresponds to about 0.4 ppm.

Chapter 8

Analysis

8.1 Overview

The obtained data are analyzed to produce a energy spectrum and to reconstruct the event topology. Figure 8.1 shows an example waveforms of the K_α 30 keV event. The analysis process is as follows.

1. Hit pulse finding
2. Clustering of hits
3. Hit reconstruction
   (a) Conversion of the ADC count to the number of photons
   (b) Correction of the nonlinearity of MPPC
   (c) Correction of the EL gain of each cell
   (d) Conversion of the clock number to the absolute z-position
4. Event reconstruction
5. Correction of the time dependence
6. Correction of the z-dependence
7. Production of energy spectrum

Details of each process are described in the following sections.

The coordinate defined as Fig. 8.2 is used in this chapter. The origin is set at the center of the anode electrode.

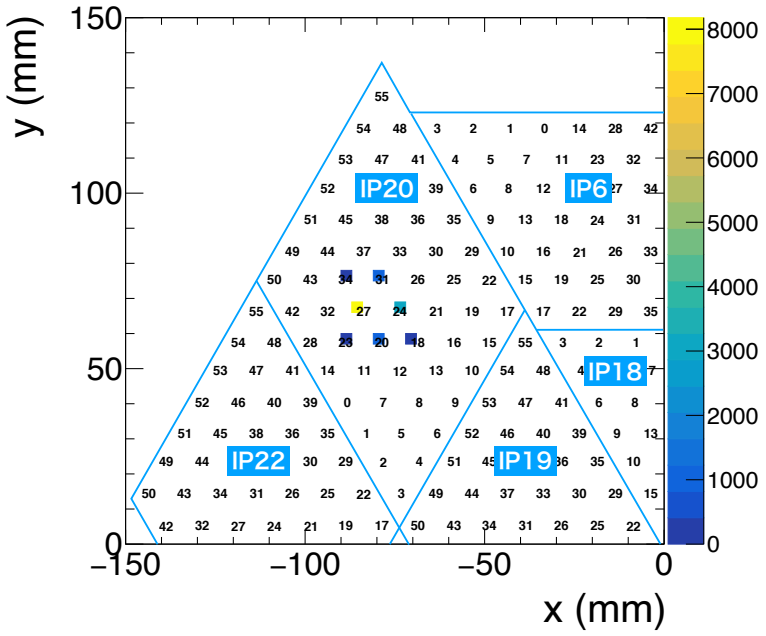

(a)

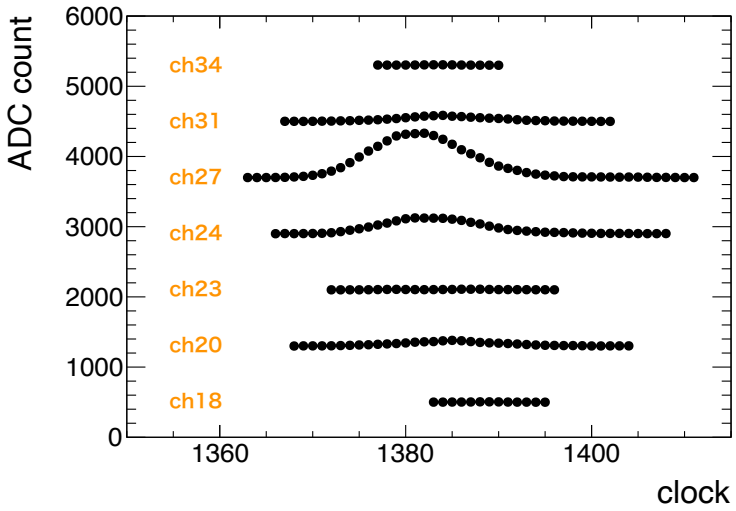

(b)

Figure 8.1: Example of the hit channels of the candidate K_α event. Hit map of the cluster is shown in (a). Numbers in the figure indicate the of channel of the AxFEB. Waveforms of the cluster are shown in (b).

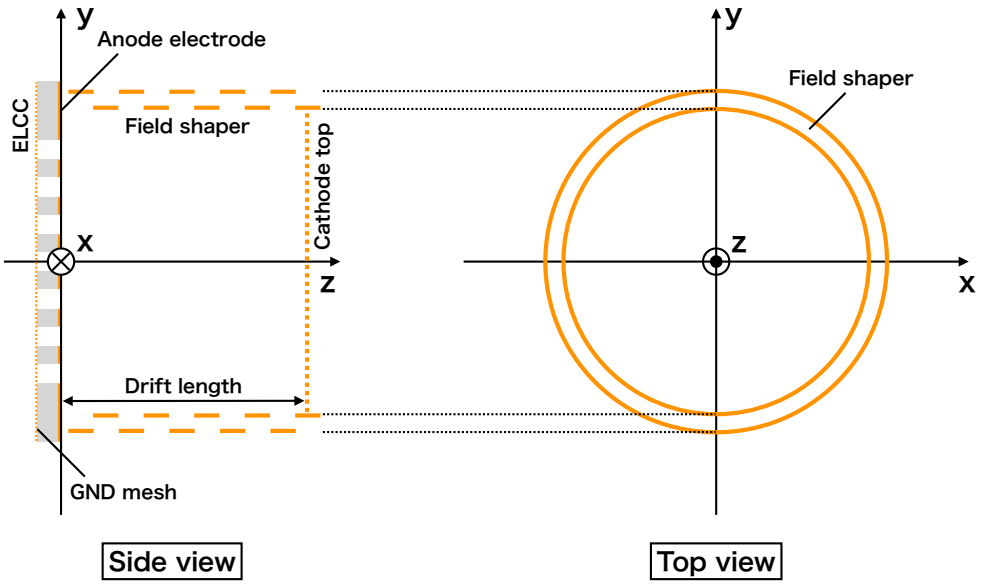

Figure 8.2: Coordinate used in the analysis.

8.2 Hit Finding

The EL light signal is acquired by the ADCL in the AxFEB. In order to search hit pulses, the baseline of the event waveform is first calculated and then hit pulses are searched as excess from the baseline.

Figure 8.3 shows the waveform averaged over many events. The fluctuation of the pedestal in the ADCL is two or three ADC counts. Dark pulses of the MPPC are smoothed by the analog circuit in the AxFEB, and the effect of the dark pulse is within this fluctuation. There are few hit pulses in 1300 – 1499 clocks. Therefore, the baseline is obtained by averaging the ADC count at 1300 – 1499 clocks, which corresponds to 200 μs – 300 μs from the trigger timing and is unlikely to have pulses. The temporary baseline is calculated by averaging the baseline region but excluding the region where the ADC count exceeds a threshold (3.5 counts) from the simple average. Then the pulses in the baseline region are scanned again, and the region containing a pulse is excluded with a margin of 10 clocks before and after the pulse. By averaging the remaining region, the final baseline is obtained.

Next, the EL signal is scanned. The pulse threshold is set to 3.5 counts, which corresponds to about 3.3 p.e., from the baseline. In this process, the start timing clock is recorded as *rise-clock* and the end timing clock as *fall-clock*. The x, y positions are reconstructed from the channel number.

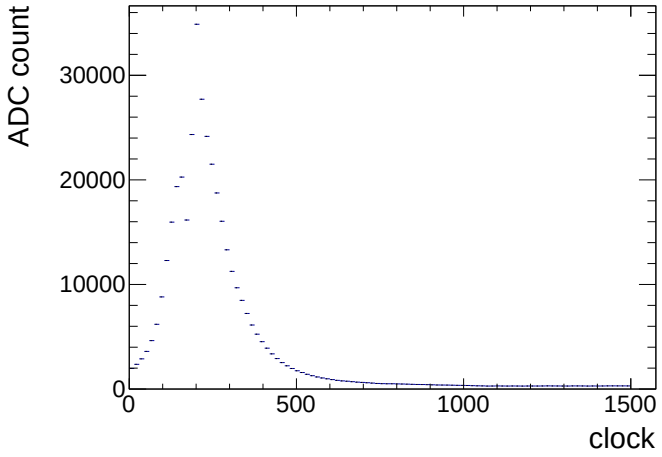

Figure 8.3: Waveform averaged over events. The region (1300 – 1499 clocks) has little pulses and is appropriate for the baseline analysis.

8.3 Hit reconstruction

8.3.1 Conversion to photon equivalence

The ADC counts are converted to the number of photons using the 1 p.e. gain obtained in Section 6.1.

8.3.2 Nonlinearity Correction

The nonlinear response of the MPPC is corrected by

$$N_{\text{true}} = \frac{N_{\text{ob}}}{1 - \dfrac{\tau}{\Delta t \cdot N_{\text{pix}}} N_{\text{obs}}}, \tag{8.1}$$

which is the inverse solution of Eq. 6.1 for N_{true}. Considering the effect of the mesh, the τ for each MPPC obtained in Chapter 6 is adapted for Eq. 8.1 after subtracting -2 ns.

8.4 Clustering of hits

If two pulses of the adjacent channels have timing overlap or the gap less than 2 clocks, the same cluster_id is given for two pulses. This process is performed for all pulses.

Each pulse is integrated with the 5 clocks margin before and after rise and *fall-clock*. When adjacent pulses in the same channel are less than 5 clocks integration is done only for one pulse to avoid double counting.

Then, the number of photons in the same cluster is summed up. The smallest *rise-clock* and the largest *fall-clock* are adapted as the *rise-clock* and *fall-clock* of the cluster. The center-of-mass position of the cluster is also calculated in this process.

8.5 EL gain Correction

The EL gain is defined as the number of photons detected by the MPPC when one ionization electron is incident on that ELCC cell. The EL gain varies channel-by-channel because of the machining accuracy even if the same voltage is applied. Since the difference of the EL gain worsen the energy resolution, it is necessary to correct the difference. In order to determine the EL gain of each channel, clusters made by the 29.7 keV K_α ray is used. More specifically, clusters satisfying following condition are used:

- No veto channel
- No overflow in ADC counts
- Fully contained ($rise\_clock > 20$ && $fall\_clock < (sample\_depth - 20)$

Example of the photon number distribution around the K_α peak for all channels is shown in Fig. 8.4a. By fitting the peak by the Gaussian function, the mean photon number ($total\_mean$) is obtained as 14,000 photons, which means EL gain is 10.4 photon/electron. Next, a same distribution is prepared for each channel. For each K_α cluster, the most bright channel is selected and the cluster photon number is filled into the distribution of the corresponding channel. For example, in Fig. 8.1, the brightest channnel is ch27 of IP20. The peak position (ch_mean) is obtained for each distribution by fitting with a Gaussian function. Figure 8.4b shows the distribution of the peak position of all channels.

A temporal correction factor of the EL gain (ch_elcor) is obtained for each channel as follows

$$ch\_elcor = \frac{total\_mean}{ch\_mean}. \tag{8.2}$$

The ch_elcor is multiplied the photon number in order to correct the EL gain. Note that the ch_elcor of the veto channels are set to 1 since the statistics is not enough and also some electrons are absorbed in the anode electrodes in the veto channel cluster. Since the cluster of K_α contains multiple channels as shown in Fig. 8.1a, the process is repeated a few times and the final correction factor is obtained. In this analysis, we iterated for six times. The result of the iteration of the EL gain correction is shown in Fig. 8.5. It is confirmed that the K_α peak becomes sharper and sharper, and the ch_mean and ch_elcor is to be equal.

8.6 The t_0 detamination and z reconstruction

The absolute z-position is given for pulses by the difference of the pulse timing and t_0, the time at which the event occurred. Since the scintillation light is emitted within a couple of

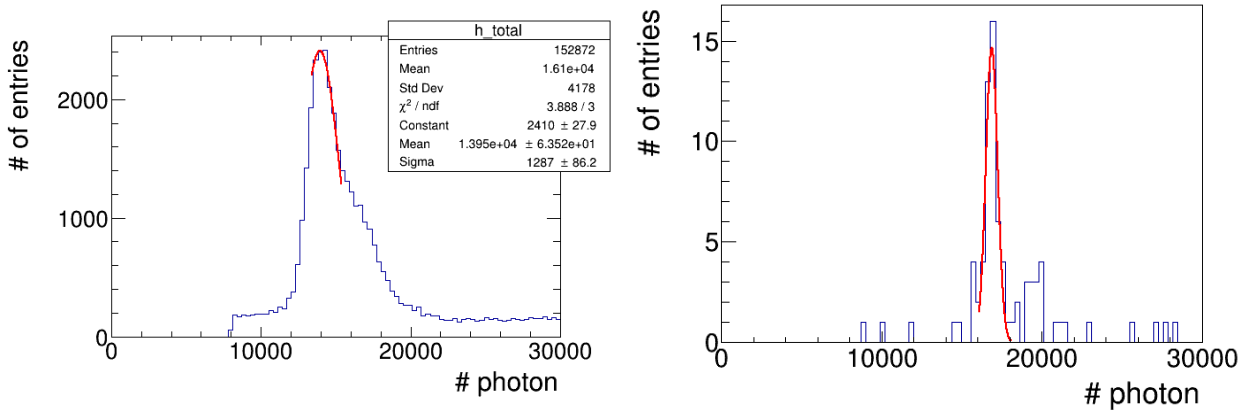

(a) (b)

Figure 8.4: (a) Distributions of the cluster photon number around the K_α peak for all channels. Since the EL gain varies channel-by-channel, peaks of K_α and K_β are not separated. The total fit mean of the K_α (*total_mean*) is obtained by fitting the peak by a Gaussian function. (b) Distributions of the cluster photon number around the K_α peak for a channel. The peak position (*ch_mean*) is obtained for each distribution by fitting with a Gaussian function.

100 ns from the time the event occurred, the scintillation light timing is used as the t_0 timing. The scintillation light is detected by the PMTs placed on the cathode side. An example of the waveform of the PMT output is shown in Fig. 8.6. In order to synchronize the event timing between AxFEB and v1724 for the PMT readout, the NIM logic signal issued by the trigger signal from HUL to acquire the data from AxFEB is input to ch7 of v1724.

The scintillation light is identified as follows. The baseline is calculated in the 0–999 clocks by averaging the waveform. The *rise-clock* and *fall-clock* and the number of the coincidence channels are recorded, where the hit threshold is 200 count from the baseline. If the gap between pulses is closer than 10 clocks, those pulses are merged into one pulse.

Since both EL signal and scintillation signal make spiky waveforms, EL signals could be misidentified as a scintillation signal if pulses are selected using only pulse height and width and the number of coincidences channels. In order to avoid this misidentification, the pulse is required to be isolated from other pulses by 100 clocks, that is 1 μs. The size of 100 clocks is decided from the drift velocity of the ionized electrons and the duration time of the EL signal. Since the drift velocity of the ionized electron is typical $\sim 1\,\mathrm{mm}/\mu\mathrm{s}$, and the depth of the cell is 5 mm, the EL signal continues for $\sim 5\,\mu$s for each electron. When EL light is generated, there should be other pulses in the vicinity of the EL light. By requiring pulses to be isolated, it is possible to avoid misidentification of this EL light as scintillation light.

Following conditions are required:

- The number of coincidence channels is more than two.
- The pulse is isolated.

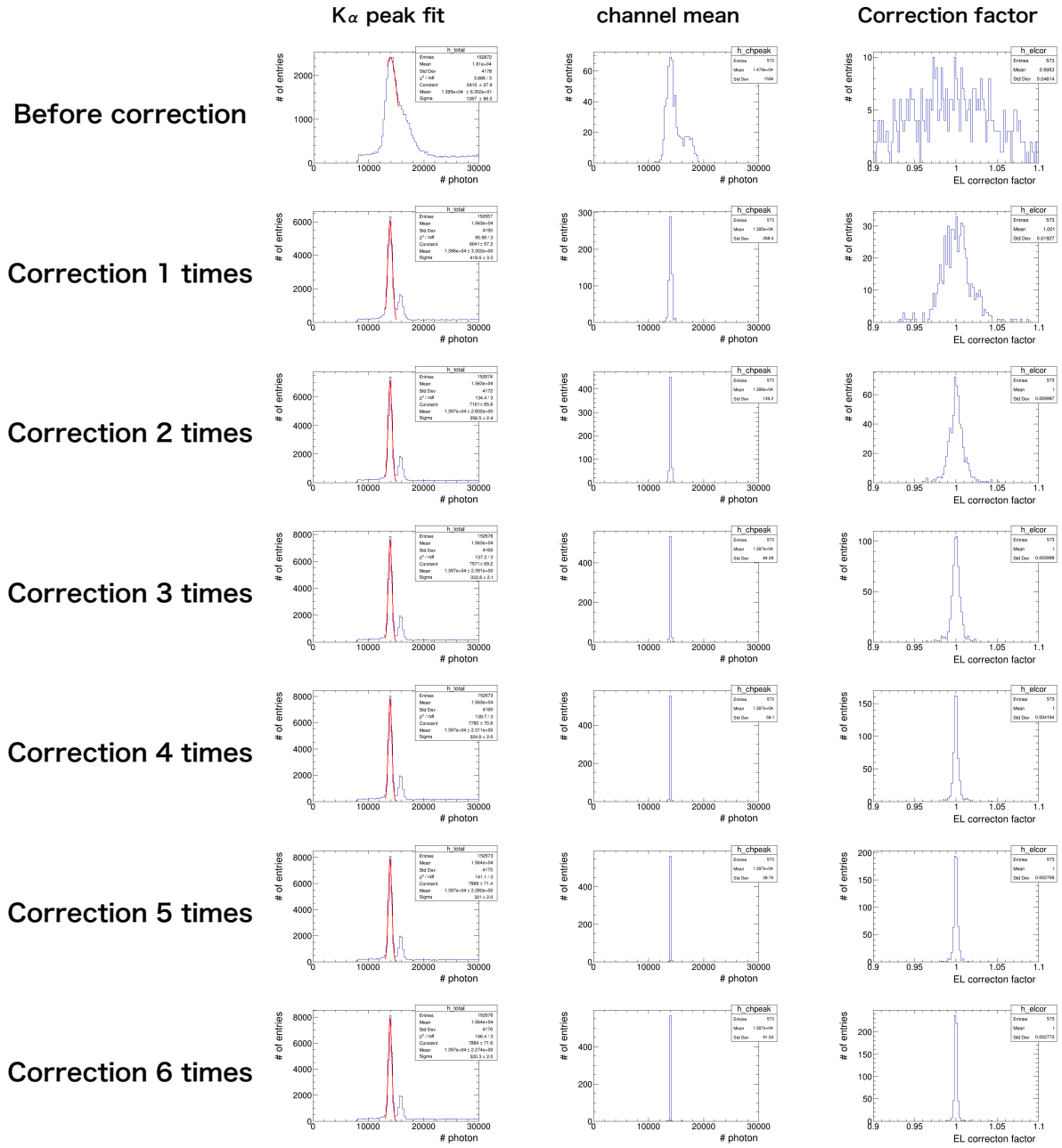

Figure 8.5: Result of the iteration of the EL gain correction. It is confirmed that the K_α peak is sharper and sharper, and the channel mean (*ch_mean*) is to be same value (about 14,000 photons), and the correction factor (*ch_elcor*) is to be 1.

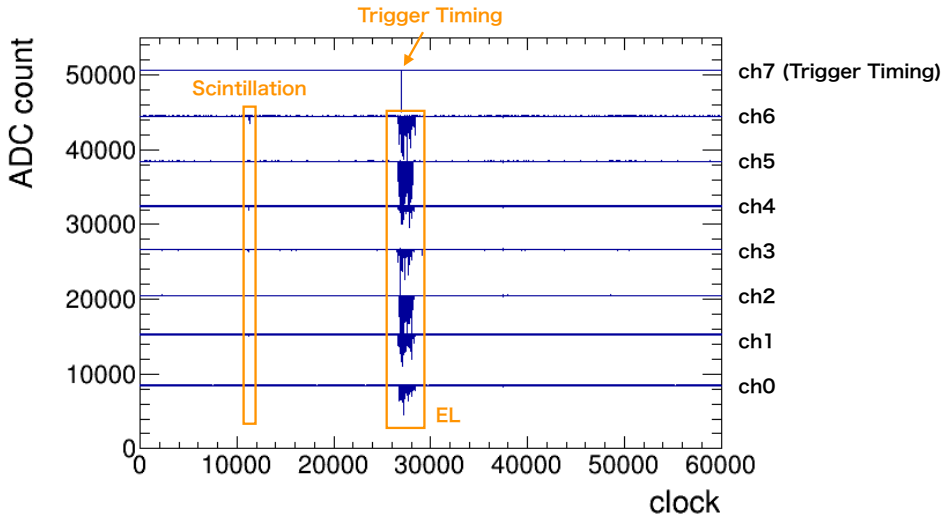

Figure 8.6: Example waveform of PMTs. One clock corresponds to 10 ns. The channel 7 records the NUM logic signal issued by the trigger to acquire the data from AxFEB.

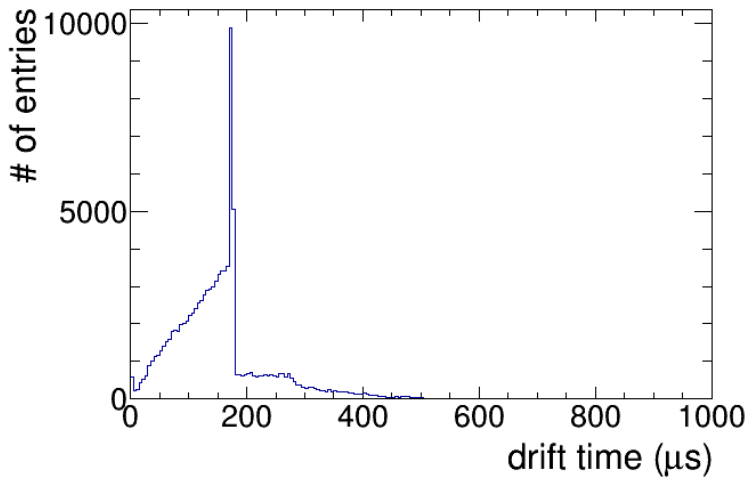

Figure 8.7: Distribution of the time difference between the scintillation timing and the EL_fall. Cathode crossing events are at 175 μs. Events after the peak are considered due to misidentification of the scintillation light.

- The $fall\_clock$ is ahead of the trigger timing.
- The pulse width ($fall\_clock - rise\_clock$) is smaller than 400 clocks (4 μs).

Among the pulses that satisfied these conditions, the closest pulse to the trigger timing is adopted as the scintillation light. To calculate the z position from the timing information, it is necessary to know the drift velocity of the ionization electron. The drift velocity can be obtained by dividing the length between the anode electrode and the cathode mesh, 180 mm, by the drift time of the event that crossed the cathode mesh.

Figure 8.7 shows the disribution of the time difference of EL_fall and Sci_rise. The peak structure at around 175 μs corresponds to the tracks that crossed the cathode. Therefore, the drift velocity is calculated to be 1.03 mm/μs. The events after the peak are considered to be misidentification of scintillation light when true scintillation is not detected.

Then, the z-position of the hit can be calculated as

$$(z\ position) = (hit\ timing - Sci\_rise) \times (drift\ velocity). \tag{8.3}$$

Comparing the numbers of events before and after the z-position reconstruction of run001, 99,024 events are reconstructed from 200,018 events (Fig. 8.8). In the lost events, no pulse is found that satisfies the scintillation requirements. Therefore, the detection efficiency of the scintillation light is 49.5% in run001.

On the other hand, for the events around 1.8 MeV (870×10^3 photons), 695 events are reconstructed from 945 events after the z-position reconstruction. The detection efficiency of the scintillation light around 1.8 MeV is 73.5%.

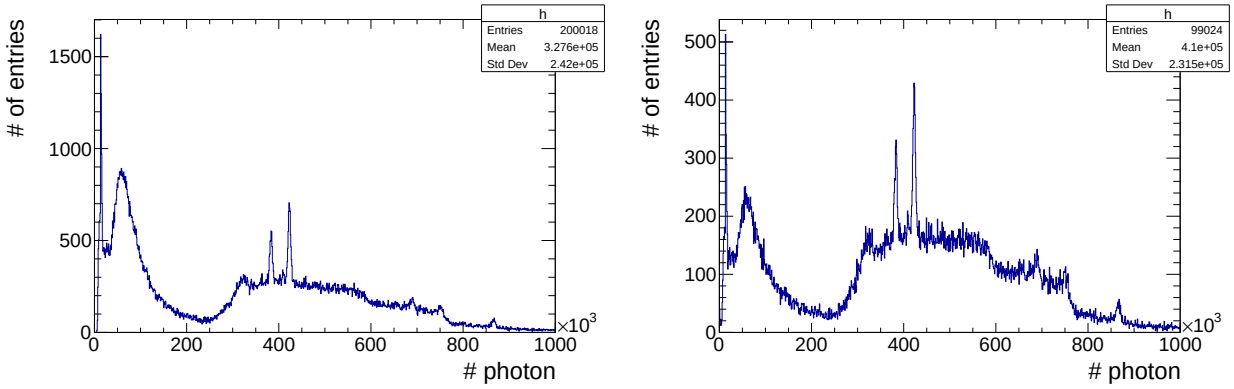

(a) Before the z-position reconstruction.

(b) After the z-position reconstruction.

Figure 8.8: Distributions of the number of photons. No cut is appried.

8.7 Time dependence Correction

The EL yield varies depending on various factors such as gas purity. In order to correct such time-dependent variation, the K_α peak is used. For every thirty minutes; the K_α peak position, is stored in the variable $Kalpha\_period$ (Fig. 8.9b) for clusters which satisfies the following conditions

- do not include veto channels.
- Waveform does not overflow.
- Waveform is fully contained in the event (rise_clock $>$ 20 && fall_clock $<$ (depth $-$ 20))
- z cut (rise_pos_z $>$ 20 && fall_pos_z $<$ (drift_length $-$ 10))

The correction factor, defined as $tcor\_factor$, is given as

$$tcor\_factor = \frac{Kalpha\_total}{Kalpha\_period}, \tag{8.4}$$

where $Kalpha\_mean$ is the K_α peak averaged over all period. The result of the time correction is shown in Fig. 8.10. The red markers represents the position of K_α peak with fit error bar.

The number of photon distribution with the K_α peak and fit after the time correction is shown in Fig. 8.11. The sigma of the peak is changed from 306.1 (Fig. 8.9a) to 290.2, it is confirmed that the energy resolution is improved.

8.8 z-dependence Correction

Ionization electrons could be absorbed by inpurity molecules in the xenon gas and the signal size could be reduced. This decrease would have z-dependence:

$$N = N_0 e^{-\frac{z}{\lambda}}, \tag{8.5}$$

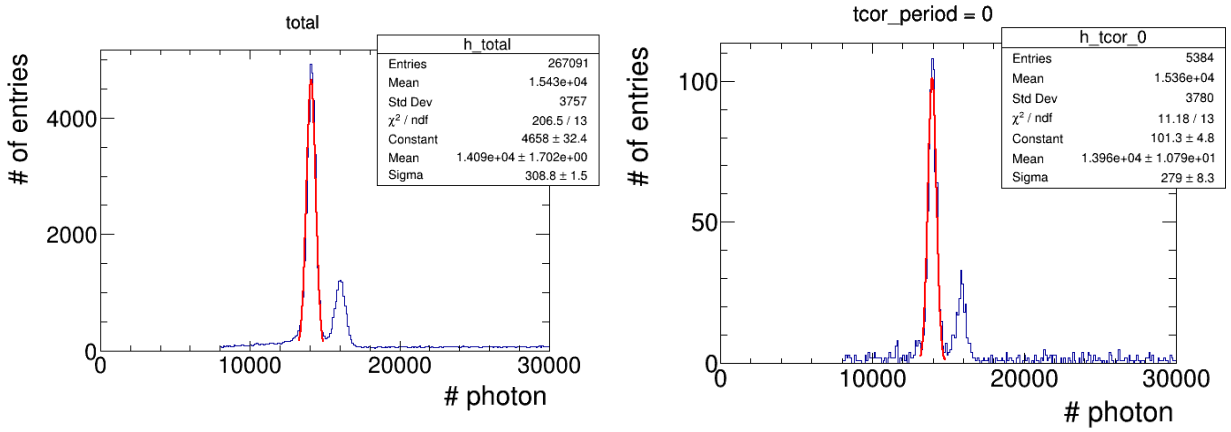

(a) Total cluster-integral.

(b) Sliced cluster-integral.

Figure 8.9: The number of photons distribution for events with the K_α and K_β peaks before the time correction. (a) For all period. *Kaplha_total* is obtained by fitting mean of the K_α peak. (b) Example of a 30 minutes period. *Kalpha_period* is obtained by fitting mean of the K_α peak.

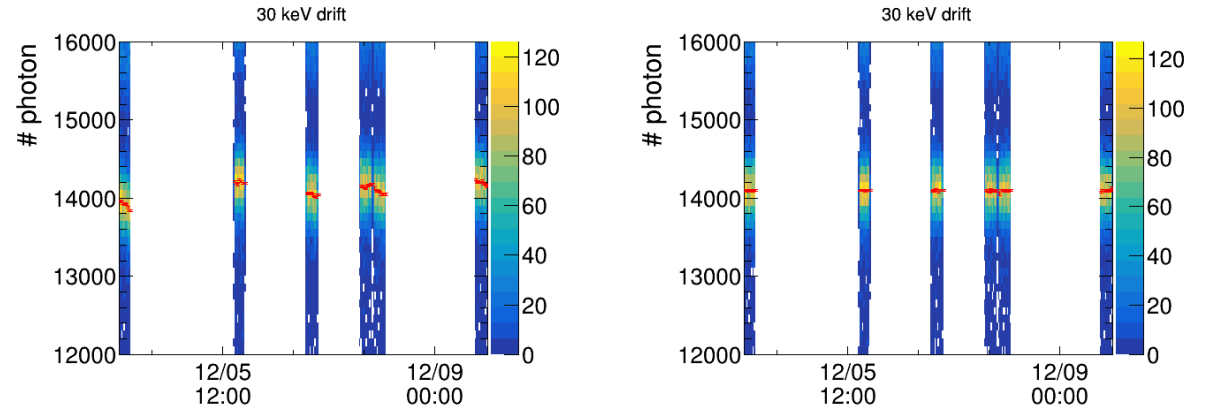

(a) Before time correction.

(b) After time correction.

Figure 8.10: Comparison of the time fluctuation between before and after of the time correction. The red marker indicates the *Kalpha_period* in each sliced period. It is confirmed that the fluctuation is corrected after the time correction.

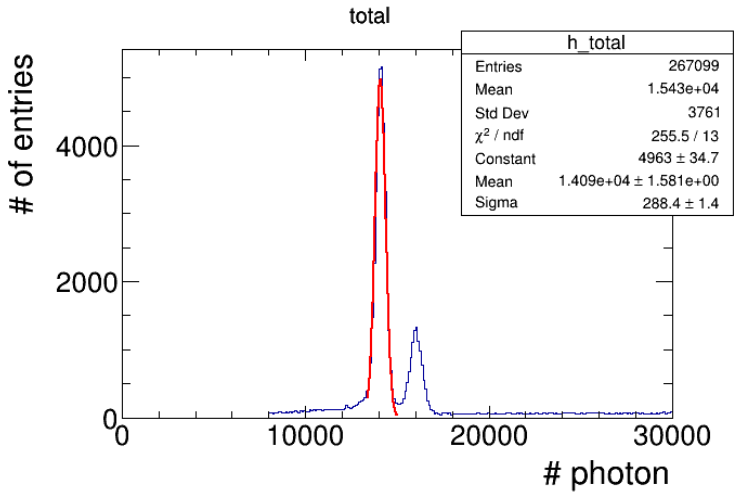

Figure 8.11: Number of photons distribution for events with K_α peak. The K_α peak after the time correction.

where λ is a absorption length. When z is sufficiently smaller than λ, Eq. 8.5 is approximated as

$$N \approx N_0 \left(1 - \frac{z}{\lambda}\right). \tag{8.6}$$

The z-dependence is corrected as,

$$N_0 = \frac{N}{1 - \frac{z}{\lambda}}. \tag{8.7}$$

To determine λ, the K_α peak is used. For every 20 mm slice in z of cluster center of mass, the number of photons of K_α is determined. Here, the following condition is required for clusters:

- Not include veto channels.
- Waveform does not overflow.
- Waveform is fully contained in the event (rise_clock $>$ 20 && fall_clock $<$ (depth $-$ 20))
- z cut (rise_pos_z $>$ 20 && fall_pos_z $<$ (drift_length $-$ 10))

The relationship between the peak photon number and z position is shown in Fig. 8.12a. The data points are fitted by a linear function in the region $(60 - 160\,\text{mm})$ and the fit result is shown as the red line. The absorption length is given as $\lambda = 21,400 \pm 4,000\,\text{mm}$ from this fitting. Fig. 8.12b shows the result of the z position correction. It is confirmed that the slope compornent is corrected.

The number of photon spectra around the K_α peak before and after the z position correction is shown in Fig. 8.13. Although the fit sigma is not changed significantly, the fit-mean is slightly increased after the correction.

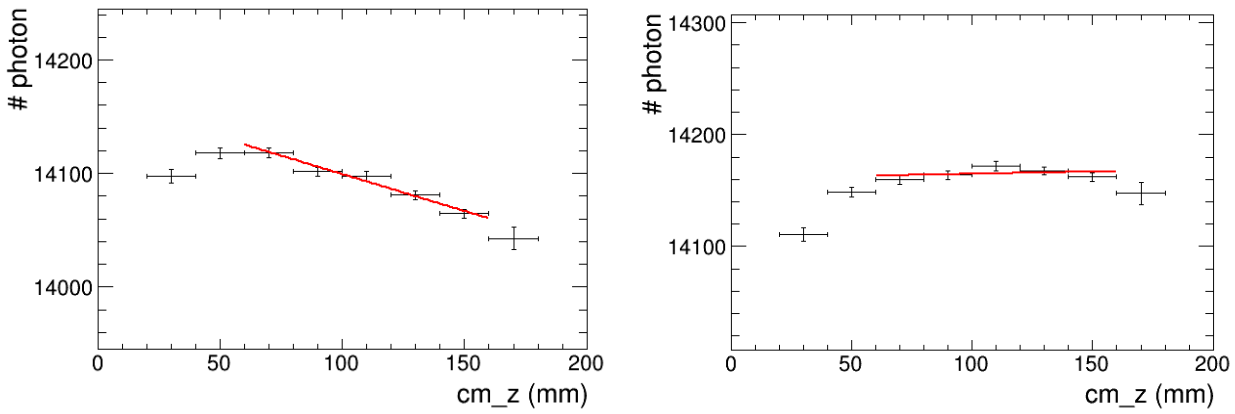

(a) Before z-correction. (b) After z-correction.

Figure 8.12: Relationship between the K_α peak photon number and z-sliced position. The data points are fitted by a linear function in the region $(60 - 160\,\mathrm{mm})$ and fit result is shown as the red line.

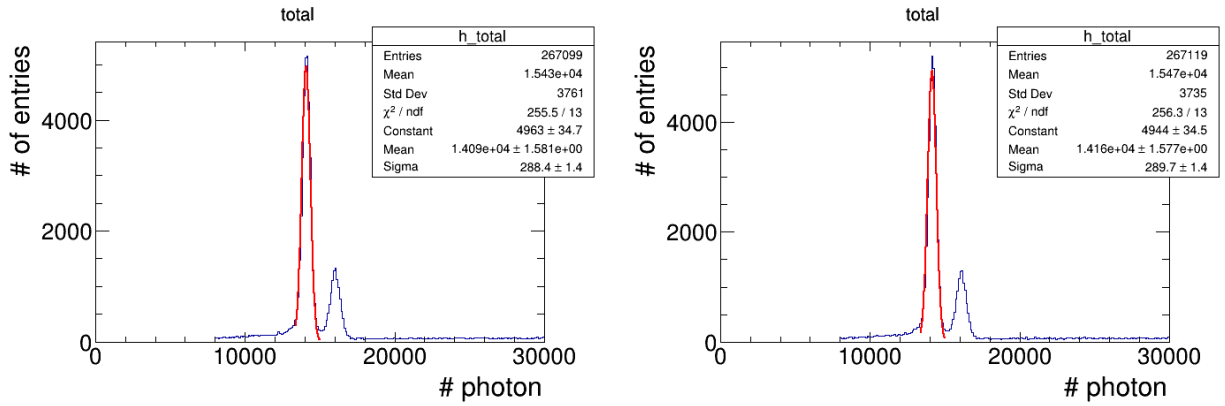

(a) Before z-correction. (b) After z-correction

Figure 8.13: The number of photon spectra around the K_α peak. Although the fit sigma is not changed the fit-mean is slightly increased after the correction.

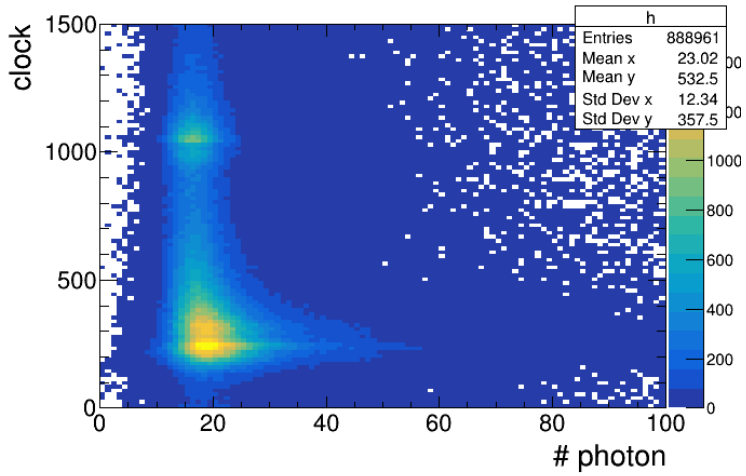

Figure 8.14: Relationship between the center-of-mass position and the number of photons of the cluster around the region of less photons. There are clusters with small number of photons (# photons < 30), around 1,000 clocks.

8.9 Cluster Selection

The relationship between the center-of-mass position and the number of photons of clusters around the region of less photons is shown in Fig. 8.14. There are small clusters (# photons $<$ 30), around 1,000 clocks. It is considered that the small clusters are produced when EL light hits the cathode mesh and electrons are produced (Fig. 8.15). If the small cluster is included in the event reconstruction, the *fall-clock* would be overvalued. Therefore, small clusters are excluded from event reconstruction.

In order to exclude the effect of the small cluster sufficiently, a small cluster of fewer than 100 photons is cut in the event integral. In order to evaluate the effect of the small cluster cut for the full peak of 1.8 MeV, the number of photons in an event using small clusters of less than 100 photons is obtained as shown in Fig. 8.16. The cut-off of the event integrl is about 400 photons. Considering that the number of photons at the full peak of 1.8 MeV is about 850×10^3 photons, the effect of the small cluster cut for the full peak is 0.035% at most.

8.10 Cluster Merge and Event Selection

By summing up the number of photons of clusters after the small cluster cut, the number of photons of the event is obtained. Here, the smallest *rise-clock* and the largest *fall-clock* are adapted as the *rise-clock* and *fall-clock* of the event.

As the event selection, following condition is required.

- No veto channels.

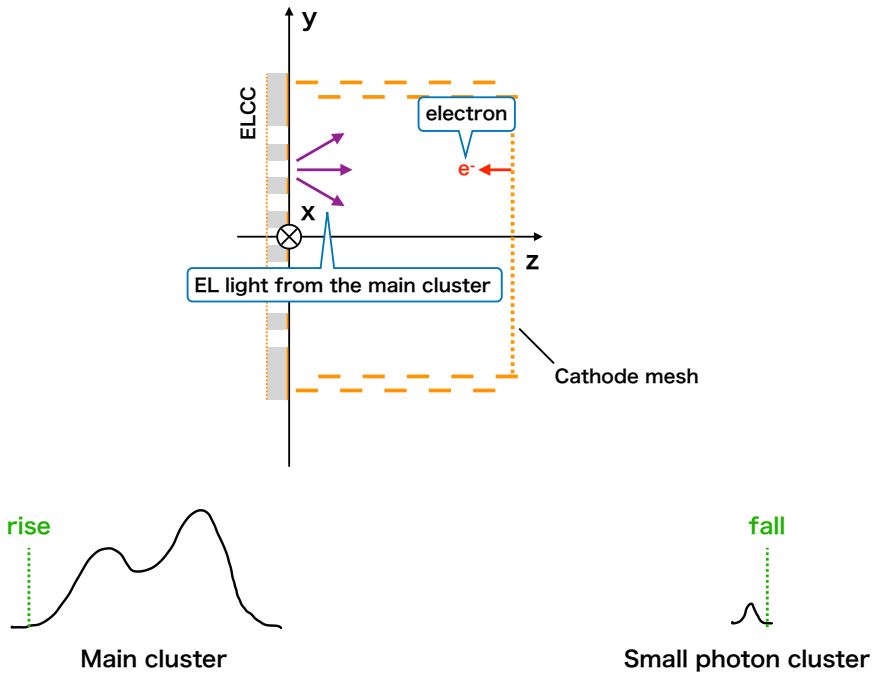

Figure 8.15: Possible mechanism of making the cluster with less photons around 1,000 clocks. It is considered that the small clusters are produced when EL light hits the cathode mesh and electrons are produced. If the small cluster is included in the event, the value of *fall-clock* would be overvalued.

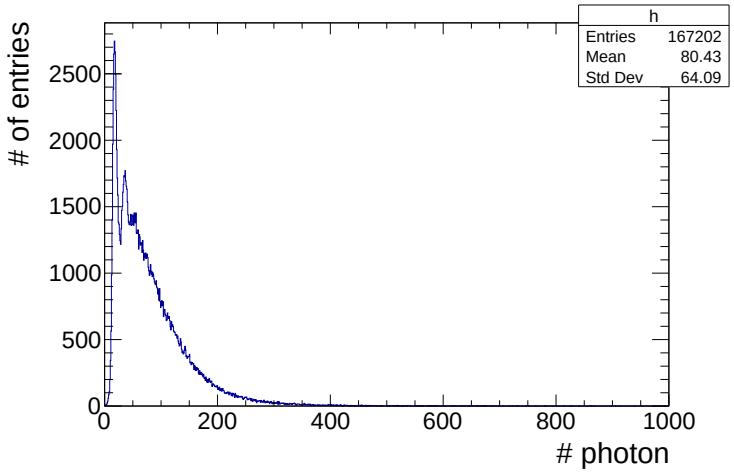

Figure 8.16: A distribution of the number of photons by using less than the 100 photon cluster. The cut off of the distribution is about 400 photons.

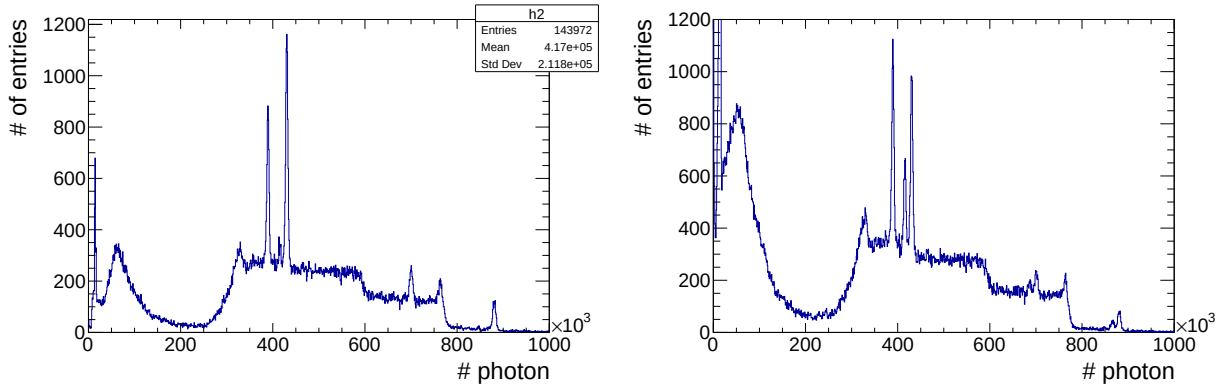

(a) Event photon number.

(b) cluster photon number.

Figure 8.17: Distributions of the number of photons for clusters and for events.

- Waveform does not overflow.
- Waveform is fully contained in the event (rise_clock $>$ 20 && fall_clock $<$ (depth $-$ 20))
- z cut (rise_pos_z $>$ 20 && fall_pos_z $<$ (drift_length $-$ 10))

8.11 Energy Reconstruction

Finally, the distributions of the number of photons for clusters and for events are obtained (Fig. 8.17). Some peaks are observed in Fig. 8.17. Considering the number of photons in the K_α peak, peaks are identified as shown in Table. 8.1. Also the peak around 7.8×10^5 photons is considered as the Compton edge of the 1836 keV.

Table 8.1: .

Number of photons	Origin	Energy
$\sim 14,000$	K_α	29.68 keV
$\sim 16,000$	K_β	33.62 keV
$\sim 3.9 \times 10^5$	^{88}Y (Double escape of 1836 keV)	814 keV
$\sim 4.2 \times 10^5$	^{88}Y (Escape peak of 898 keV)	$\sim$ 868 keV
$\sim 4.3 \times 10^5$	^{88}Y (Full peak)	898 keV
$\sim 6.9 \times 10^5$	^{40}K (Excape peak of 1461 keV)	$\sim$ 1431 keV
$\sim 7.0 \times 10^5$	^{40}K (Full peak)	1431 keV
$\sim 8.7 \times 10^5$	^{88}Y (Escape peak of 1836 keV)	$\sim$ 1806 keV
$\sim 8.8 \times 10^5$	^{88}Y (Full peak)	1836 keV

Each peak is fitted as shown in Fig. 8.18. Figure 8.19a shows the relationship between

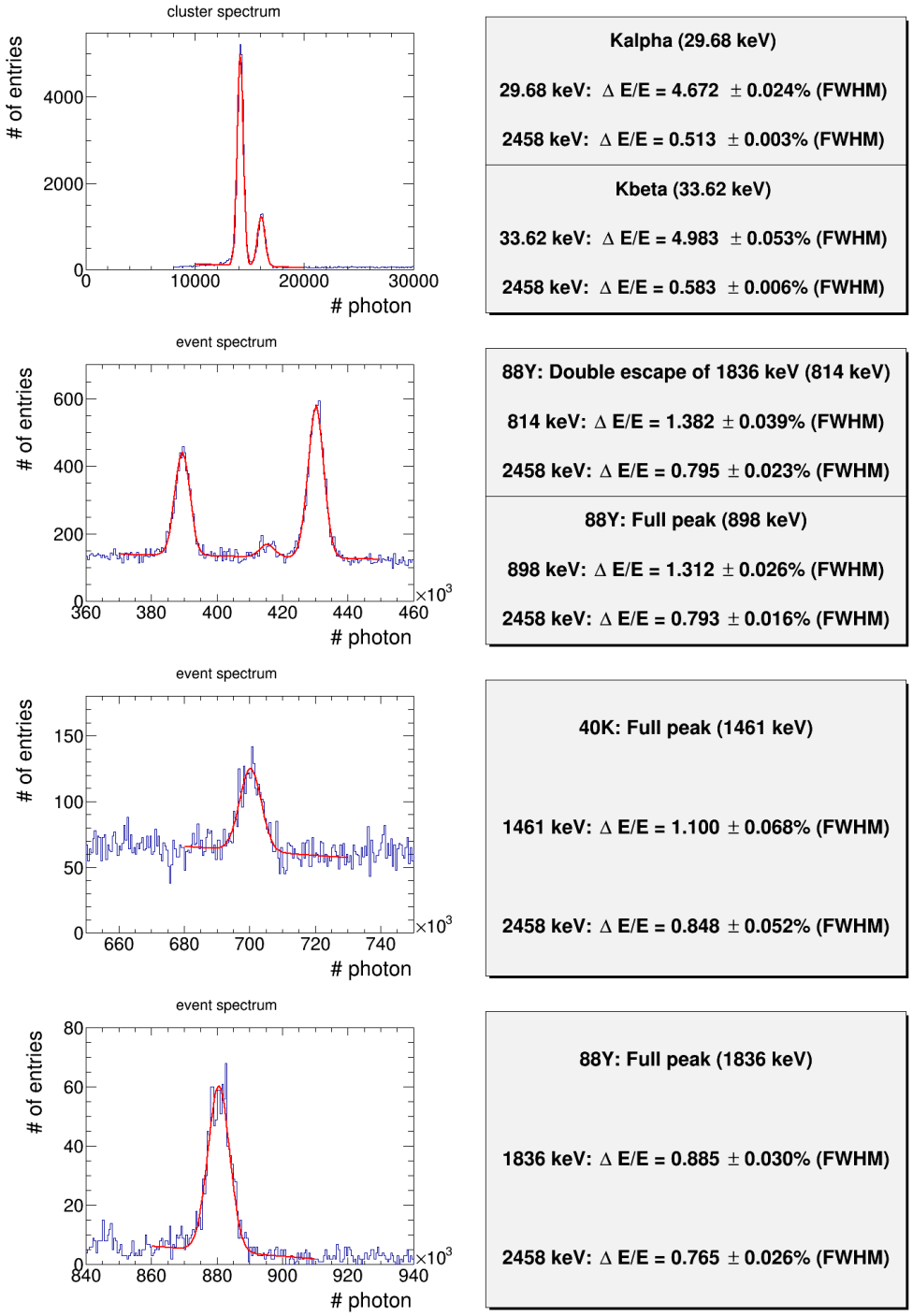

Figure 8.18: Result of the fit of each peak. In the region of the K_α and K_β peak, two Gaussian functions and liner functions are used. In the region of double escape peak of 1836 keV and the full peak of 898 keV, triple Gaussian function and linear function is used. In the region of the full peak of 1461 keV, a single Gaussian function and liner function is used. In the region of the full peak of 1836 keV, a single Gaussian function and liner function is used.

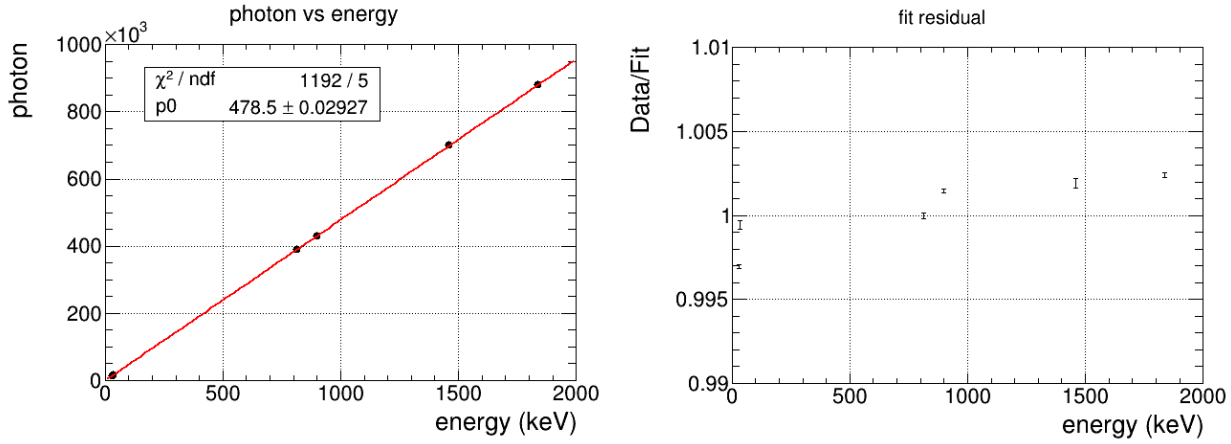

(a) (b)

Figure 8.19: (a) The relationship between the fit mean of the peak and the energy. By fitting the linear function, the conversion factor is obtained. (b) The residual between the data and the fit function. The data points are larger than the fit function in the high-energy region.

the peak photon number and the peak energy. By fitting this with a linear function, the conversion factor from the number of photons to the energy is obtained. The residual between the data and the fit function is shown in Fig. 8.19b. The data points are larger than the fit function in the high-energy region.

Figure 8.20 shows the final energy spectrum.

8.12 Result

8.12.1 Energy Resolution

In order to evaluate the energy resolution at Q-value of ^{136}Xe, the energy resoltion of each peak is fitted by a function of $a\sqrt{E}$ and $a\sqrt{E} + bE$. The fitting result is shown in Fig. 8.21. The energy resolution at Q-value is obtained as 0.79% (FWHM) by $a\sqrt{E}$ and 0.78% (FWHM) by $a\sqrt{E} + bE$.

8.12.2 Event Topology

Event topologes which has 1.8 MeV energy are obtained in this measurement. Four examples are shown in Fig. 8.22.

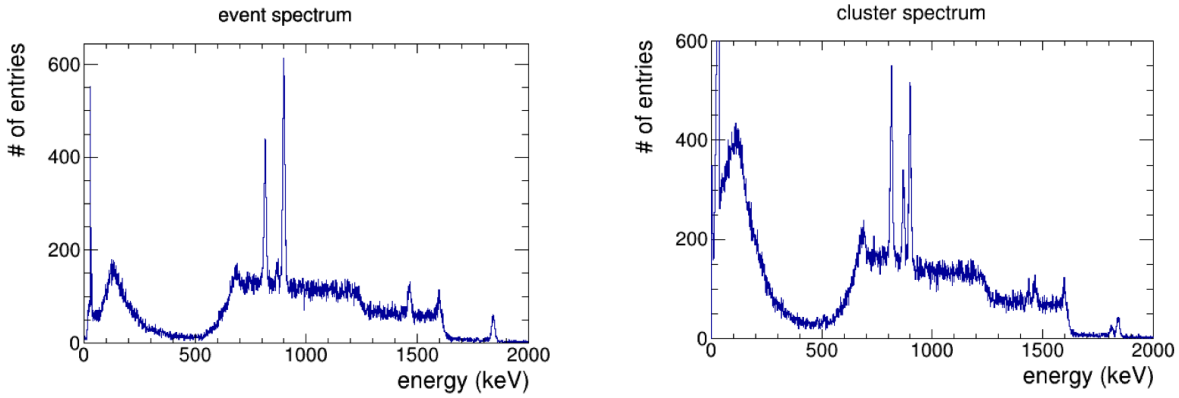

(a) Event spectrum.

(b) Cluster spectrum.

Figure 8.20: Energy spectra for clusters and for events.

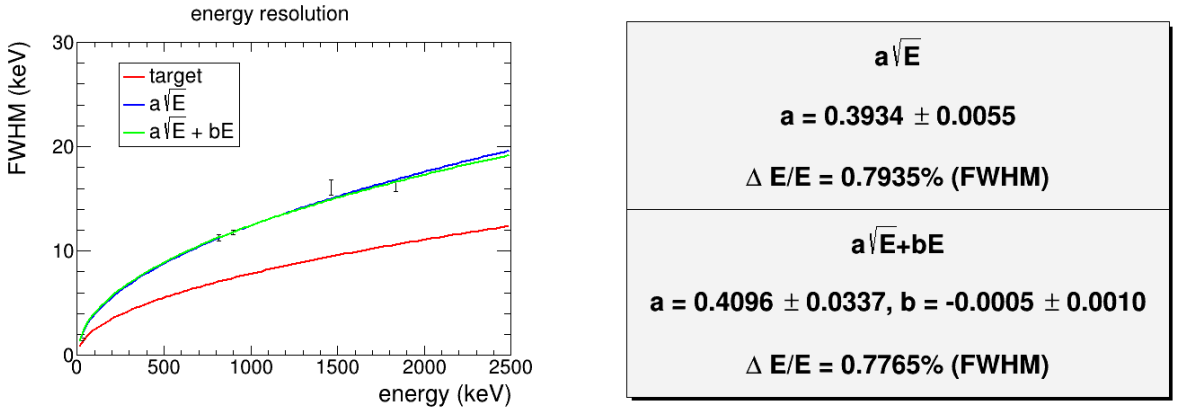

Figure 8.21: Extraporation of the energy resolution to the Q-value. Red line is the target energy resplution. In order to evaluate the effect of linear compornent, in adition to $a\sqrt{E}$, $a\sqrt{E} + bE$ is used as the fit function.

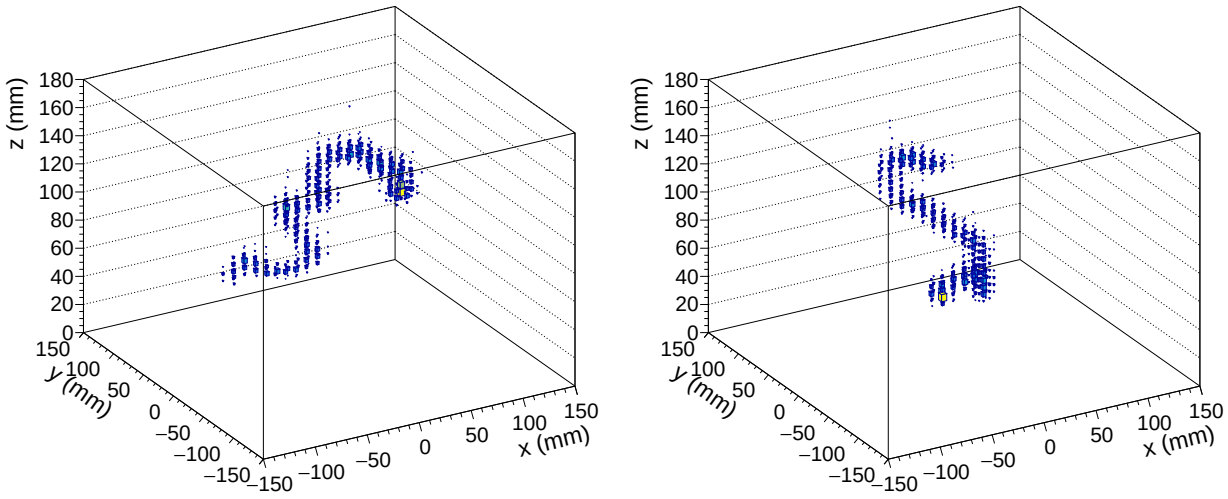

(a) (b)

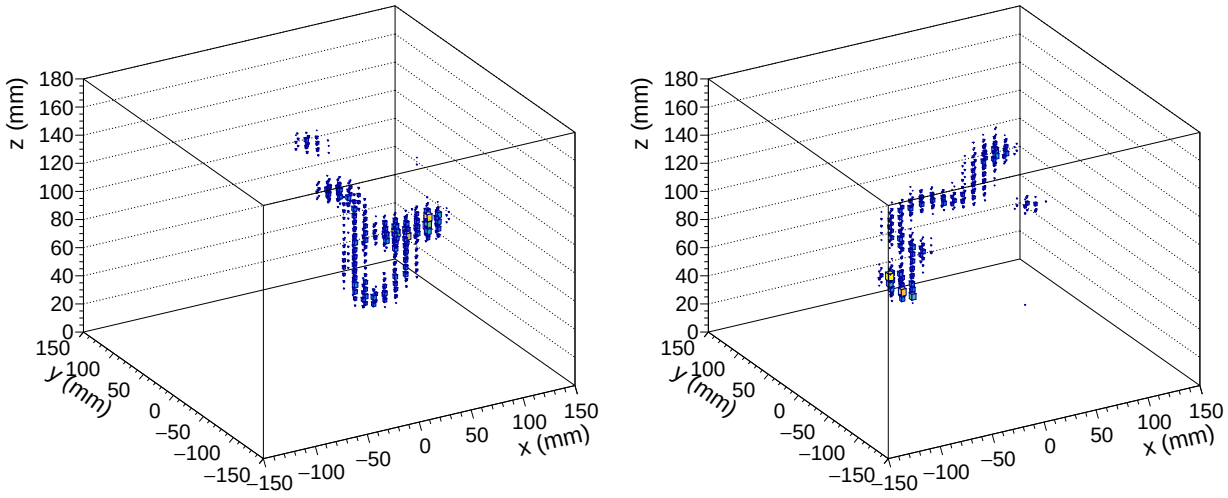

(c) (d)

Figure 8.22: Event topologes of of event having 1.8 MeV energy. In (c) and (d), characteristic xray cluster is confirmed near the main cluster.

Chapter 9

Discussion

In this chapter, we discuss the factors that affect the energy resolution. The following factors are considered:

(1) Fluctuation of the number of ionization electrons produced.

(2) Fluctuation of EL amplification.

(3) Position dependence of EL amplification factor.

(4) Waveform processing in AxFEB (waveform amplification and shaping with 400 ns time constant and 5 MHz, 12 bit digitalization).

(5) Error in EL gain calibration.

(6) Accuracy of MPPC recovery time measurement.

(7) Error in time correction.

(8) Error in z correction.

(9) Dependence of the drift electric field.

The intrinsic energy resolution is given by Eq. 2.1. When E is $1,836$ keV, W_{i} is 22.1 eV, F is 0.13, the intrinsic energy resolution (1) is 0.30% FWHM at 1.8 MeV.

Monte Carlo simulation studies were done with (2) to (4) implemented. The condition of the simulation that of the previous measurement: the gas pressure is 4 bar, number of cells is 168, and electron energy is 511 keV. Then, it is converted to the values at the condition of the measurement of this thesis.

As a result, it turns out that the contribution of (2) is 0.30%, and the effects of (3) and (4) are negligible.

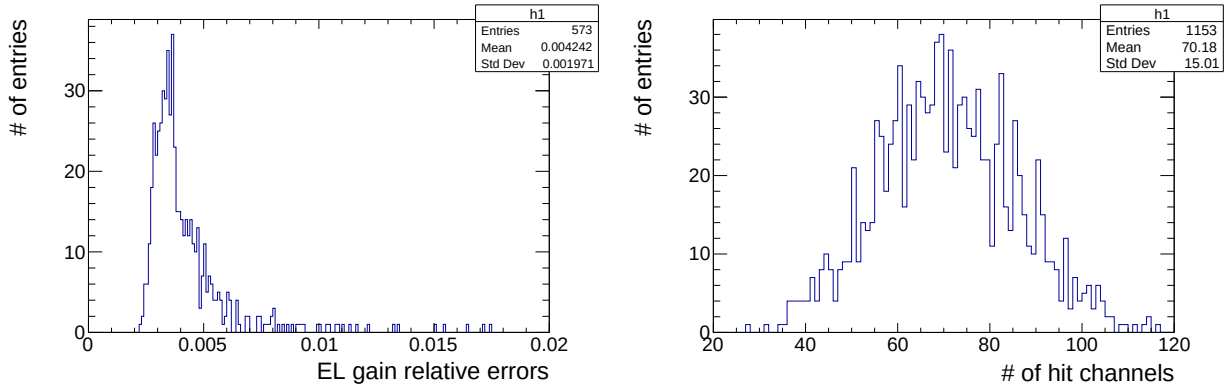

(a) (b)

Figure 9.1: Relative error during EL gain correction (a) and the distribution of the number of hit channels for the 1.8 MeV event (b).

9.1 Error in EL gain calibration

Figure 9.1 shows the relative error during EL gain correction (a) and the distribution of the number of hit channels for the 1.8 MeV event (b). The accuracy of the EL gain correction is 0.42%. The average number of hit channels for 1.8 MeV is 70. Therefore, the error of the EL gain calibration is

$$2.355 \times \frac{0.42}{\sqrt{70}} = 0.12\ \%. \tag{9.1}$$

9.2 Effect of the MPPC Recovery Time

From Fig. 6.10b, the error in recovery time is 0.43 ns. Since $\delta\tau$ is scanned in units of 2 ns to account for mesh effects, the systematic error in recovery time is

$$\frac{2\ \text{ns}}{\sqrt{12}} = 0.58\ \text{ns}. \tag{9.2}$$

Therefore, the total error in recovery time is

$$\sqrt{0.43^2 + 0.58^2} = 0.72\ \text{ns}. \tag{9.3}$$

From Fig. 6.5, the effect on resolution when the error in recovery time is 0.72 ns is negligible.

9.3 Error in Time Correction

The relative error of the correction factor for the time correction is shown in Fig. 9.2. Since the accuracy of the time correction is 0.86%, the effect on the energy resolution is

$$2.355 \times 0.86 = 0.20\%. \tag{9.4}$$

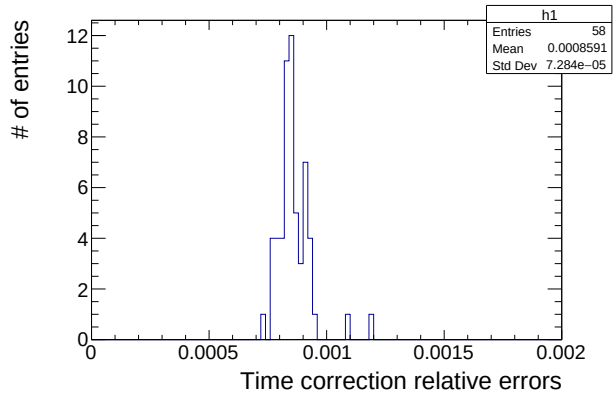

Figure 9.2: Relative error of the correction factor for the time correction.

9.4 Error in z Correction

Here, the error in the absorption length and the effect of the light intensity decrease at $z < 60$ mm in Fig. 8.12a are discussed. First, the error in the absorption length is discussed. The length of the track in the z direction at 1.8 MeV is about 76 mm. Figure 8.12a shows that the light intensity of K_α decreases by 0.4% with 100 mm. Since the detection efficiency of the scintillation photon of the K_α is low, it is likely that the absorption length is evaluated small due to misreconstruction of the event position. Assuming an absorption length error of 100%, the effect on the energy resolution is

$$0.4 \times \frac{76}{100} = 0.3\% \tag{9.5}$$

Next, the effect of light reduction at $z < 60$ mm is discussed. At $z < 60$ mm, the maximum reduction is about 0.2% even after z-correction Since about half of all events is there in the $z < 60$ mm region, the effect on resolution is

$$2.355 \times \frac{0.2}{\sqrt{12}} \times \frac{1}{\sqrt{2}} = 0.096\%. \tag{9.6}$$

Therefore, the contribution of z-dependence to resolution is

$$\sqrt{0.3^2 + 0.096^2} = 0.31\%. \tag{9.7}$$

9.5 Dependence of Drift Electric Field

In this measurement, the electric field was limited to $E_{\mathrm{EL}} = 2.25\,\mathrm{kV/cm/bar}$ and $E_{\mathrm{drift}} = 75\,\mathrm{V/cm/bar}$ due to discharge problems. The relationship between the drift electric field and

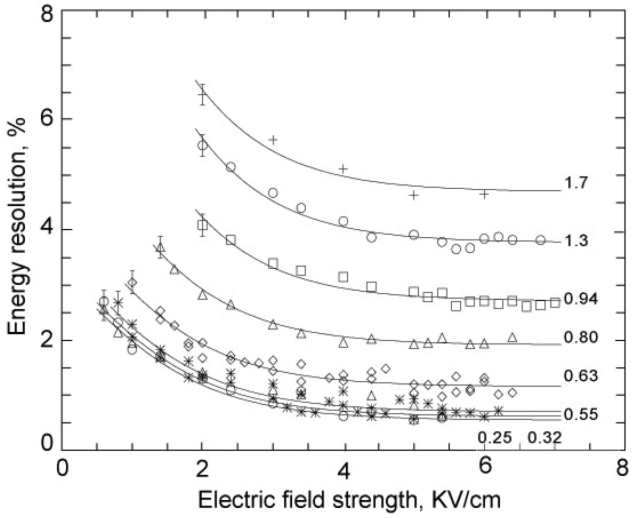

Figure 9.3: Relationship between the energy resolution and the drift electric field [16]. The energy resolution is expressed as the FWHM.

energy resolution is shown in Fig. 9.3. At 0.25 g/cm^3, the electric field is 4.275 kV/cm when 100 V/cm/bar is applied. On the other hand, when 75 V/cm/bar is applied, the electric field is 3.2 kV/cm. By the change of the electric field, the energy resolution changes from 0.6% to 0.75%. The contribution to the energy resolution is

$$\sqrt{0.75^2 - 0.6^2} \times \sqrt{\frac{662}{1836}} = 0.27\%. \tag{9.8}$$

9.6 Summary and Prospect

The breakdown of resolution obtained from the above discussion is summarized in Table 9.1.

In order to improve the energy resolution, it is important to suppress fluctuations of EL amplification. The following measures are effective.

- Improvement of EL electric field.
- Improvement of gas purity.
- Expanding the size of the MPPC photosensitive area.

A comparison with previous measurements is shown in Table 9.2. In Condition 5, where the dew point is 8°C lower than this measurement and $E_{\mathrm{EL}} = 3$ kV/cm/bar is achieved, the number of photons of K_α is 1.5 times higher than this result. By changing the photosensor size of the MPPC from 3 mm square to a size that covers the entire cell hole, the area of the

Table 9.1: Breakdown of the energy resolution at 1.8 MeV.

Fluctuation of the number of ionization electrons produced	0.25%
Fluctuation of EL amplification	0.30%
Position dependence of EL amplification factor	0%
Waveform processing in AxFEB	0%
Error in EL gain calibration	0.12%
Accuracy of MPPC recovery time measurement	0%
Error in time correction	0.20%
Error in z correction	0.31%
Dependence of the drift electric field	0.27%
Unknown	0.62%
Total	0.89%
Target which corresponds to 0.5% FWHM at Q-value	0.58%

photosensitive surface is 1.77 times larger. With the above measures, fluctuations during EL amplification can be reduced from 0.30% to 0.18%.

In this measurement, the energy resolution of K_α and K_β is higher than the other peaks. The reason for this is not yet understood, but clarifying this reason may provide clues for further improving the energy resolution. With the 1000L detector, we aim to achieve the target energy resolution of 0.5% at the Q-value based on the above measures.

Table 9.2: Result of this measurement and the electric field scan. The first line is the result of this measurement, and after the second line, the scaned results are shown.

	E_{EL} (kV/cm/bar)	E_{drift} (V/cm/bar)	Dew point (°C)	Num photons at K_α	Resolution at Q-value
This result	2.25	75.0	~ -85	$\sim 14,200$	$0.77 \pm 0.03\%$
Condition 1	2.0	50.0	-90.5	13,326	$0.71 \pm 0.01\%$
Condition 2	2.25	56.25	-94	17,406	$0.57 \pm 0.01\%$
Condition 3	2.5	62.5	-90.5	20,494	$0.57 \pm 0.01\%$
Condition 4	2.75	68.75	-94	24,334	$0.55 \pm 0.01\%$
Condition 5	3.0	75.0	-93	27,586	$0.59 \pm 0.01\%$
Condition 6	3.0	62.5	-93	27,521	$0.61 \pm 0.01\%$
Condition 7	3.0	50.0	-93	27,444	$0.61 \pm 0.01\%$

Chapter 10

Conclusion

We have developed a high-pressure xenon gas TPC, AXEL detector, for $0\nu\beta\beta$ decay search. The AXEL detector uses a uniquely developed readout mechanism called ELCC to measure the energy and reconstruct the trajectories of beta rays. With the very high energy resolution and reconstructed trajectories, it realizes high background rejection. The ELCC has a rigid structure and is feasibly extendable to larger sizes. The target energy resolution of the AXEL detector is 0.5% (FWHM) at Q-value (2458 keV), and we are aiming to search for $0\nu\beta\beta$ decay by constructing a ton or even larger scale detector.

The main objectives of this thesis are to establish the AXEL technology, especially ELCC, including the scalability, and to demonstrate the performance at the Q-value of the $0\nu\beta\beta$ decay with a 180L prototype detector.

In phase 1, a performance evaluation was conducted with three ELCC modules. It was turned out that discharge in the ELCC was the main problem to go to larger scale.

We have updated the 180L detector to phase 2 (12 modules). Discharge points at ELCC are identified with a system using a camera set inside the vessel. The structure of the ELCC is modified to strengthen the resistivity against discharge. The fraying of the mesh for ELCC electrode is prevented by welding mesh with PFA films. Through these efforts, we succeeded in applying a design voltage to the ELCC stably for more than 48 hours at 7.6 bar. A dedicated readout digitizer module was developed, and a data acquisition system was constructed. The performance of this phase 2 system was evaluated by using 1.8 MeV gamma-rays from ^{88}Y, and we obtained $0.89 \pm 0.03\%$ energy resolution in FWHM. This corresponds to $0.77 \pm 0.03\%$ at the Q-value.

In this thesis, we established the basic technology for the enlargement of the AXEL detector. To reach the lower limit of the inverted hierarchy region of $0\nu\beta\beta$ decay, the target energy resolution of FWHM 0.5% at the Q-value must be achieved. Breakdowns of energy resolution of this result are discussed. It is shown that the improvement of the EL electric field and gas purity and the enlargement of the MPPC photosenser size are effective to suppress the fluctuation during EL amplification, which is the major contribution to the energy resolution. Another behavior that is not understood is that the energy resolution of K_α and K_β is higher than the resolution of other peaks. If the reason for this can be understood, it could provide a clue for improving the energy resolution. By solving these

issues in the future, we aim to achieve the target energy resolution of FWHM 0.5% at the Q-value.

Bibliography

[1] F. Reines and C. L. Cowan. Detection of the free neutrino. *Phys. Rev.*, 92:830–831, Nov 1953.

[2] Y. Fukuda and others. Evidence for oscillation of atmospheric neutrinos. *Phys. Rev. Lett.*, 81:1562–1567, Aug 1998.

[3] M. Aker and The KATRIN Collaboration. Direct neutrino-mass measurement with sub-electronvolt sensitivity. *Nature Physics*, 18(2):160–166, Feb 2022.

[4] Aghanim, N. and Planck Collaboration. Planck 2018 results - vi. cosmological parameters. *A&A*, 641:A6, 2020.

[5] Abe S. et al. First search for the majorana nature of neutrinos in the inverted mass ordering region with KamLAND-Zen. arXiv:2203.02139.

[6] Tsutomu Yanagida. Horizontal Symmetry and Masses of Neutrinos. *Progress of Theoretical Physics*, 64(3):1103–1105, 09 1980.

[7] Sacha Davidson, Enrico Nardi, and Yosef Nir. Leptogenesis. *Physics Reports*, 466(4):105–177, 2008.

[8] Andrea Giuliani and Alfredo Poves. Neutrinoless double-beta decay. *Advances in High Energy Physics*, 2012:857016, Dec 2012.

[9] Gómez-Cadenas J.J. and Martín-Albo J. Phenomenology of neutrinoless double beta decay. *PoS*, 004(GSSI14), 2014.

[10] Frank T. Avignone, Steven R. Elliott, and Jonathan Engel. Double beta decay, majorana neutrinos, and neutrino mass. *Rev. Mod. Phys.*, 80:481–516, Apr 2008.

[11] Stefano Dell'Oro, Simone Marcocci, and Francesco Vissani. New expectations and uncertainties on neutrinoless double beta decay. *Phys. Rev. D*, 90:033005, Aug 2014.

[12] M. Agostini et al. Final results of gerda on the search for neutrinoless double-β decay. *Phys. Rev. Lett.*, 125:252502, Dec 2020.

[13] J. Renner et al. Energy calibration of the next-white detector with 1% resolution near q$\beta\beta$ of 136xe. *Journal of High Energy Physics*, 2019(10):230, Oct 2019.

[14] M. Kekic et al. Demonstration of background rejection using deep convolutional neural networks in the next experiment. *Journal of High Energy Physics*, 2021(1):189, Jan 2021.

[15] F. Monrabal et al. The NEXT white (NEW) detector. *Journal of Instrumentation*, 13(12):P12010–P12010, dec 2018.

[16] Elena Aprile, Aleksey E. Bolotnikov, Alexander I. Bolozdynya, and Tadayoshi Doke. *Noble Gas Detectors*. WILEY-VCH Verlag GmbH & Co. KGaA, 2006.

[17] C M B Monteiro, L M P Fernandes, J A M Lopes, L C C Coelho, J F C A Veloso, J M F dos Santos, K Giboni, and E Aprile. Secondary scintillation yield in pure xenon. *Journal of Instrumentation*, 2(05):P05001–P05001, may 2007.

[18] S Ban. *Development of a high pressure xenon gas time projection chamber with a unique cellular readout structure to search for neutrinoless double beta decay*. PhD thesis, Department of Physics, Graduate School of Science, Kyoto University, march 2020.

[19] motion (available at: https://motion-project.github.io/index.html, last accessed date 23 February 2022).

[20] S Yanagita. AXEL 実験における高エネルギー分解能を達成するための MPPC および読み出し回路についての研究. Master's thesis, Department of Physics, Graduate School of Science, Kyoto University, january 2016.